The Thesis committee for Randall Paul Williams
certifies that this is the approved version of the following thesis:

Experimental Measurement of Overall Effectiveness and Internal Coolant Temperatures for a Film Cooled Gas Turbine Airfoil With Internal Impingement Cooling

APPROVED BY

SUPERVISING COMMITTEE:

David Bogard, Supervisor

Halil Berberoglu

Experimental Measurement of Overall Effectiveness and Internal Coolant Temperatures for a Film Cooled Gas Turbine Airfoil With Internal Impingement Cooling

by

Randall Paul Williams, B.S.

THESIS

Presented to the Faculty of the Graduate School of
The University of Texas at Austin
in Partial Fulfillment
of the Requirements
for the Degree of

MASTER OF SCIENCE IN ENGINEERING

The University of Texas at Austin
December 2012

Dedicated to my wonderful family.

Acknowledgments

I would like to first extend my sincere thanks to Professor Bogard for all of his guidance over the last 2 years. Before joining his Turbulence and Turbine Cooling Research Laboratory I was a student in his incompressible flow class, and it must be said that I've had very few teachers throughout my lifetime who are as dedicated to doing a great job teaching in the classroom in addition to doing quality research and teaching his students in the lab as Dr. Bogard is. Also, many thanks to Professor Halil Berberoglu for taking the time to read this thesis and give his valuable feedback. I would like to thank my research sponsors at Pratt and Whitney for the financial support and for giving me the opportunity to work on this project and use some of the data collected for this thesis. I would also like to think my former labmates who made TTCRL a fun place to work even on days when the experiments didn't turn out exactly like we thought they should: Todd Davidson, Jason Albert, Emily Boyd, Marc Nathan, and Tom Dyson. It's been a real pleasure working with you all. Lastly, I appreciate the help of Aaron Frost in the ME machine shop and our undergraduate assistant Andrew Tabije for their assistance in constructing the airfoil models.

Experimental Measurement of Overall Effectiveness and Internal Coolant Temperatures for a Film Cooled Gas Turbine Airfoil With Internal Impingement Cooling

Randall Paul Williams, M.S.E.
The University of Texas at Austin, 2012

Supervisor: David Bogard

A scaled-up gas turbine vane model was constructed in such a way to achieve a Biot number (Bi) representative of an actual engine component, and experiments were performed to collect temperature data which may be used to validate computational fluid dynamics (CFD) codes used in the design of gas turbine cooling schemes. The physical model incorporated an internal impingement plate to provide cooling on the inner wall surface, and film cooling over the external surface was provided by a single row of holes located on the suction side of the vane. A single row of holes was chosen to simplify the operating condition and test geometry for the purpose of evaluating CFD predictions. Thermocouples were used to measure internal gas temperatures and internal surface temperatures over a range of coolant flow rates, while infra-red thermography was used to measure external surface temperatures. When Bi is matched to an actual engine component, these measured temperatures may be normalized relative to the coolant temperature and mainstream gas temperature to determine the overall cooling effectiveness, which will be representative of the real engine component. Measurements were made to evaluate the overall effectiveness resulting from internal impingement cooling alone, and then with both internal impingement cooling and external film cooling as the coolant flow rate was increased.

As expected, with internal impingement cooling alone, both internal and external wall surfaces became colder as the coolant flow rate was increased. The addition of film cooling further increased the overall effectiveness, particularly at the lower and intermediate flow rates tested, but provided little benefit at the highest flow rates. An optimal jet momentum flux ratio of $I_{SS3} = 1.69$ resulted in a peak overall effectiveness, although the film effectiveness was shown to be low under these conditions. The effect of increasing the coolant-to-mainstream density ratio was evaluated at one coolant flow rate and resulted in higher values of overall cooling effectiveness and normalized internal temperatures, ϕ and θ, throughout the model. Finally, a 1-dimensional heat transfer analysis was performed (using a resistance analogy) in which overall effectiveness with film cooling, $\overline{\phi}$, was predicted from measurements of film effectiveness and overall effectiveness without film cooling. This analysis tended to over-predict $\overline{\phi}$, at the lowest values of the jet momentum flux ratio, I, while under-predicting it at the highest I values.

Table of Contents

List of Tables

List of Figures

Nomenclature

Λ	Turbulence integral length scale $[mm]$
0	(subscript) without film cooling
β	Orifice diameter ratio, $D_{orifice}/D_{pipe}$
χ	Coolant warming factor
ΔP_o	Orifice flow meter pressure drop $[inH_2O]$
$\dot{m}$	Coolant mass flow rate $[kg/s]$
η	Adiabatic or Film Effectiveness
η_{th}	Thermal efficiency
∞	(subscript) mainstream
ϕ	Overall Effectiveness
ρ	Density $[kg/m^3]$
θ	Non-dimensional temperature using the average impinging jet temperature as reference
A_d	Orifice discharge area $[m^2]$
aw	(subscript) adiabatic wall, typically adiabatic wall temperature of film coolant
C	Vane chord $[cm]$
c	(subscript) coolant
C_d	Orifice discharge coefficient
C_p	Coefficient of pressure

DR	Density Ratio (Film Coolant to Mainstream)
f	(subscript) with film cooling
g	(subscript) gas
I	Momentum Flux Ratio
i	(subscript) inner
$imp.jet$	(subscript) impinging jet
M	Blowing Ratio
o	(subscript) outer
P_∞	Pitot tube static pressure $[Pa]$
P_{dyn}	Pitot tube dynamic pressure $[Pa]$
P_{stag}	Pitot tube stagnation pressure $[Pa]$
PS	(subscript) pressure side film cooling holes
q''	Heat flux, $[W/m]$
r	Radius of curvature $[mm]$
Re	Reynolds number
s	Surface distance, measured downstream of the stagnation line $[cm]$
$SS3$	(subscript) suction side film cooling holes
T	Temperature, $[K]$
Tu	Turbulence intensity
U	Mean fluid velocity$[m/s]$
VR	Velocity Ratio
w	(subscript) component wall

h	Coefficient of convective heat transfer $[W/m^2]$
R.H.	Relative humidity [%]
TTCRL	Turbulence and Turbine Cooling Research Laboratory at the University of Texas at Austin

Chapter 1

Introduction

1.1 Gas Turbine Engine Basics

Since evolving into their modern form in the early part of the 20th century, gas turbine engines have found their way into widespread use in the power and transportation industries. In addition to providing propulsion and electrical power for aircraft, gas turbine engines are also used for industrial power generation because of their size and speed with which they can be started for use. A schematic of a gas turbine engine is shown below in Figure 1.1.

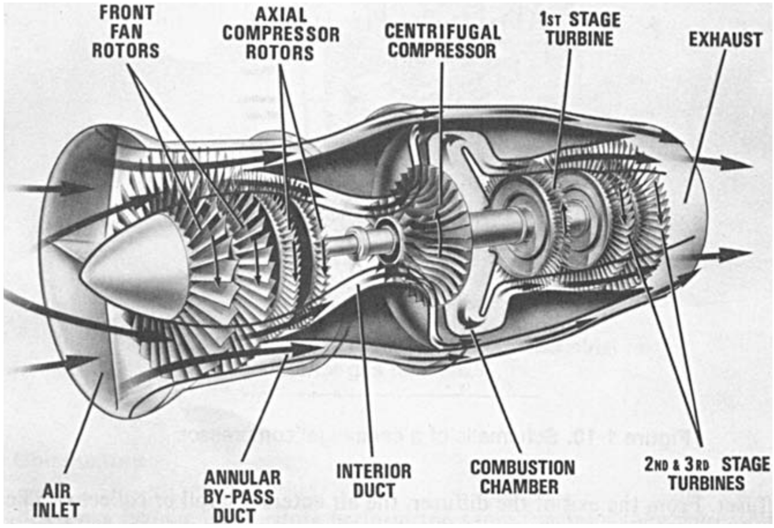

Figure 1.1: Cut-away view of a gas turbine engine
(From Boyce, 2002)

While there are nearly as many variations of the gas turbine engine as there are applications, all gas turbine engines share some common components: a compressor, combustion chamber, and turbine. Gas turbine engines can be thermodynamically described by the ideal Brayton cycle. A schematic of a basic open Brayton cycle engine is shown in Figure 1.2, illustrating the flow of the working fluid through the major system components.

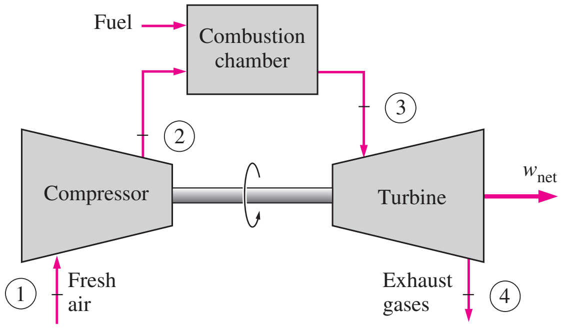

Figure 1.2: Schamatic of an ideal open Brayton cycle engine
(From Çengel and Boles, 2006)

The fresh air is first drawn into the compressor, where work is done to isentropically raise the pressure and temperature before it enters the combustor. Next, fuel is added to the compressed air in the combustor, isobarically increasing the temperature further. The mixture of air and combustion products is then isentropically expanded through one or more turbine stages where it is typically exhausted to the atmosphere. Because the gas leaving the turbine is generally warmer than the ambient fluid which it is exhausted to, heat is being rejected from the engine to the surroundings through the exhaust, completing and closing the cycle. Useful work is generated by the turbine stages, which are used to drive the compressor as well as to turn an output shaft.

The processes of the ideal Brayton cycle can be graphically depicted by using Temperature-Entropy (T-S) or Pressure-Volume (P-v) diagrams, which are shown in Figure 1.3 below. Points labelled 1, 2, and 3 represent the states of the working fluid at the entrance to the compressor, combustor, and turbine, respectively. Any heat rejected by the engine to the surroundings through the exhaust is represented by process 4-1 on the thermodynamic diagrams. For both diagrams, the total amount of work delivered through one cycle of the engine may be visually represented by the area inside each closed curve.

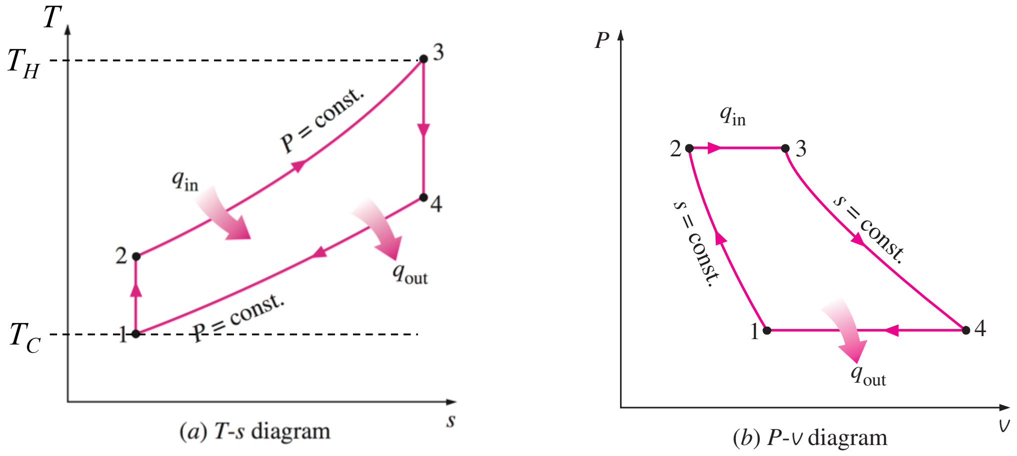

(a) T-s diagram (b) P-v diagram

Figure 1.3: T-S and P-v depictions of ideal Brayton cycle processes
(From Çengel and Boles, 2006)

The thermal efficiency of an ideal Brayton cycle engine may be expressed in terms of gas temperatures at the beginning of each thermodynamic process:

$$\eta_{th} = 1 - \frac{T_4 - T_1}{T_3 - T_2} \tag{1.1}$$

As indicated by Equation 1.1, either increasing the temperature of the working fluid entering the turbine or decreasing the temperature at which it leaves the turbine will improve the thermal efficiency of the cycle. Because of this, designers of gas turbine engines are continually seeking to increase the temperatures of the air and combustion products entering the first turbine stage. Reliability considerations provide a bound to the maximum temperature of the working fluid, which in many cases may be hotter than the maximum allowable temperature of the materials used for internal engine components such the vanes and blades of the stator and rotor. To maintain these components at a safe operating temperature, a variety of different cooling schemes may be integrated into the vanes or blades.

1.2 Gas Turbine Cooling

Gas turbine cooling can be divided into categories of internal or external cooling, depending on which side of the turbine component wall is being cooled. The coolant fluid is typically air which has been pressurized by the compressor but is bled off before it has a chance to mix with fuel in the combustion chamber. The pressure generated during compression is used to route the coolant past the combustion chamber and through to the interior of the hot components requiring cooling, where it performs its function as coolant. Because of the level of cooling needed, turbine components immediately downstream of the combustor often employ both internal and external cooling, and engine designers strive to get the maximum amount of cooling possible from a given amount of coolant.

1.2.1 Internal Cooling

An internal cooling scheme is employed when convection heat transfer through the inner surface of the part wall is used to help keep the component temperature down. Internal convective cooling has been used in gas turbines extensively since the 1960s, and multiple variations exist. Commonly, gas turbine blades and vanes will have serpentine passages which make several passes in the radial direction through which the coolant air flows, transferring heat from the inner surface of the part wall to the coolant. These serpentine passages may also have ribs added which serve the purpose of increasing the turbulence level of the coolant flow and further increasing the heat transfer coefficient. Figure 1.4 shows a turbine blade sectioned in such a way to expose the serpentine passages with rib turbulators used for cooling.

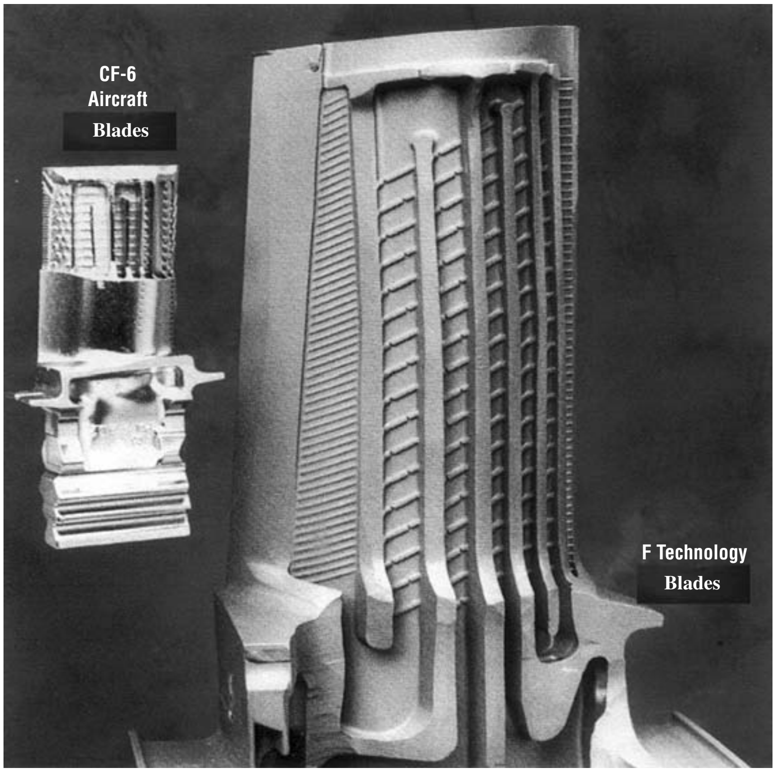

Figure 1.4: Serpentine cooling passages with rib turbulators
(From Boyce, 2002).

Another variation of internal cooling involves using impinging jets of coolant on the inner surface of the part wall to increase the internal convection heat transfer coefficient significantly. To create the impinging jets, a plate with many small holes is spaced away from the inner wall of the part so that as the coolant flows through it jets are formed. A simple illustration of this concept is shown in Figure 1.5.

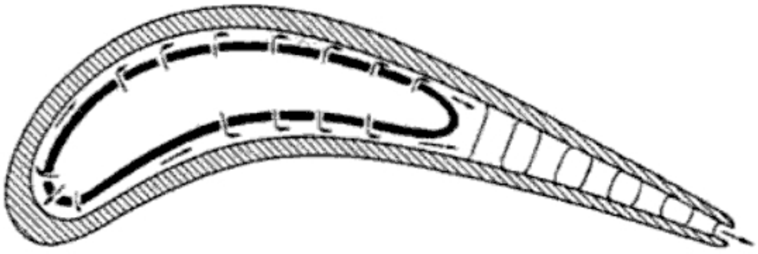

Figure 1.5: Example of internal impingement cooling (From Han et al., 2000).

1.2.2 External Film Cooling

The premise behind film cooling is simple: a thin “film” of relatively cool fluid is injected between the component requiring cooling and the hot working fluid which flows over it, reducing the driving potential for heat transfer from the hot mainstream to the part wall. This concept is illustrated in Figure 1.6. The film coolant leaves the film cooling hole at $T_{c,o}$ and flows downstream over the part surface, shielding the component from the potentially damaging temperature of the hot mainstream gasses while gradually warming up and being dispersed through turbulent mixing.

Newton’s Law of Cooling is often used by convention to relate the rate of convection heat transfer to a driving temperature difference by defining a proportionality constant, h:

$$q'' = h\left(T_1 - T_2\right), \tag{1.2}$$

where the proportionality constant h is referred to as the convection heat transfer coefficient. For heat transfer at the film cooled surface, one of the temperatures in Equation 1.2 is the component outer surface temperature, $T_{w,o}$. Identifying the other temperature and convection coefficient appropriately can be more difficult since the

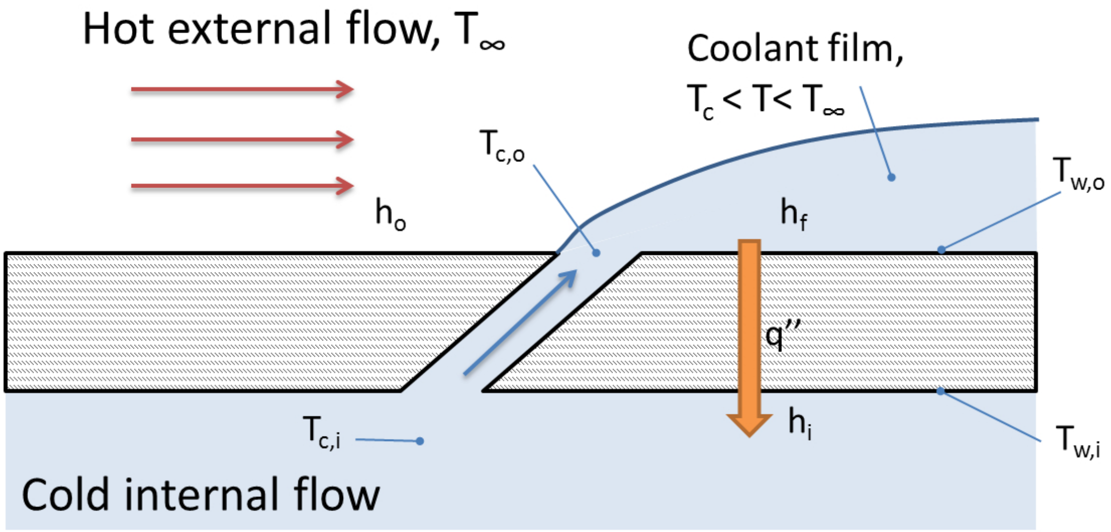

Figure 1.6: Basic concept of film cooling

temperature in the layer of film coolant will vary between $T_{c,o}$ and T_∞. If T_∞ is used as the driving temperature, then the heat transfer coefficient with film cooling will be a function of coolant temperature and flow field. A more simple definition of h_f which is independent of coolant temperature and flow field may arrived at by using the gas temperature immediately above the surface of the part as the temperature of the gas in Equation 1.2, as first proposed by Goldstein (1971). If the component surface were adiabatic so that no heat transfer occurred between it and the gas, then the temperature of the gas immediately above the component surface would be a function of mixing and heat transfer between the mainstream gas and the film coolant (Bogard and Thole, 2006). This temperature is often referred to as the adiabatic wall temperature, T_{aw}, and is relatively easy to measure. The adiabatic wall temperature is often assumed to be an accurate representation of the driving gas temperature for convection heat transfer when film cooling is used.

It is convenient to normalize T_{aw} relative to T_∞ and $T_{c,o}$ so that it becomes primarily a function of the external flow field, and dynamics of the mixing of the film cooling jet with the mainstream gas. The normalized adiabatic wall temperature, η, is referred to as "adiabatic effectiveness" or simply "film effectiveness", and is computed as:

$$\eta = \frac{T_{aw} - T_\infty}{T_{c,o} - T_\infty}. \tag{1.3}$$

With film effectiveness defined as shown in Equation 1.3, a value of $\eta = 1$ indicates that the adiabatic wall temperature is the same as the temperature of the coolant exiting the film cooling hole, and that the film coolant achieves the maximum possible reduction in driving heat transfer potential. On the other had, a value of $\eta = 0$ indicates that the adiabatic wall temperature is the same as the hot mainstream gas, implying that the film cooling jet is doing nothing to reduce the driving potential for heat transfer. Because a higher value corresponds to better film cooling performance, higher values indicate lower surface temperatures.

Because the film effectiveness is a function of the external flow field, which is a function of many different variables, there are many different parameters which are important to the performance of film cooling. Any parameter which affects the dynamic interaction between the film cooling jet and mainstream will affect the film effectiveness. The ratio of film coolant density to mainstream gas density is conventionally used as one such flow parameter in film cooling, defined as:

$$DR = \frac{\rho_{c,o}}{\rho_\infty} \tag{1.4}$$

where $\rho_{c,o}$ is the density of the coolant at the exit of the film cooling jet hole. The density ratio has significance because the amount of mixing and diffusion which occurs between the coolant jet and the mainstream is partially dependent on the densities of the two gas streams.

Another parameter commonly used when discussing film cooling studies is the mass flux ratio of the film coolant to the mainstream gas, most commonly referred to as the "blowing ratio":

$$M = \frac{\rho_{c,o} U_{c,o}}{\rho_\infty U_\infty}, \tag{1.5}$$

where $U_{c,o}$ is the bulk velocity of the film coolant being ejected from the film cooling hole. Because the temperature rise experienced by the coolant for a given amount of heat transferred to it is proportional to $\rho_{c,o} U_{c,o}$, the film coolant has greater capacity for heat transfer as either the density or the velocity of the film coolant is increased relative to the mainstream flow.

Film cooling jets are typically not ejected parallel to the component surface, but at an angle away from the surface. The interaction between the coolant jet and the mainstream gas is tied to the momentum of the coolant relative to the jet, as this determines how far into the mainstream flow the jet will penetrate. The ratio of the jet momentum flux to mainstream momentum flux is simply referred to as the "momentum flux ratio", which is represented by the letter I and is defined as:

$$I = \frac{\rho_{c,o} U_{c,o}^2}{\rho_\infty U_\infty^2}. \tag{1.6}$$

Appearing in the previous three equations is the ratio of the coolant velocity to the mainstream gas velocity - this ratio is naturally referred to as the "velocity ratio", or VR:

$$VR = \frac{U_{c,o}}{U_\infty}. \tag{1.7}$$

While it is conventionally less important than the other ratios when discussing film cooling performance, the velocity ratio is important when considered as a factor in M and I.

Gas turbine engines typically operate at density ratios of around $DR = 2$ (Bogard and Thole, 2006), although achieving such a high density ratio under the conditions often used in a laboratory setting for experimentation is can be difficult, so experiments are frequently performed at density ratios of closer to unity. Looking at Equations 1.4 through 1.7, it becomes apparent that matching both I and M without matching DR is impossible, so care must be taken when choosing which parameters to match to typical engine operating conditions when designing experiments and interpreting results.

1.2.3 Overall Effectiveness

While the performance of film cooling jets are often reported in terms of the adiabatic film effectiveness, η, the ultimate goal of all active gas turbine cooling strategies is to reduce the external surface temperature of the component being cooled - this places emphasis on the external wall temperature of the actual part as a critical parameter. The external wall temperature for the actual metal part can be normalized as follows:

$$\phi = \frac{T_{w,o} - T_\infty}{T_{c,i} - T_\infty}, \tag{1.8}$$

where $T_{w,o}$ is the outer wall surface temperature of the metal part, $T_{c,i}$ is internal coolant temperature, typically taken at the coolant inlet to the part, and the resulting normalized temperature, ϕ, is referred to as "overall effectiveness". Comparing Equation 1.8 with Equation 1.3, it may seem at first that the difference between ϕ and η is simply the coolant temperature used for normalization. The physical difference is much greater than this; η is by definition only valid for a scenario where the part wall is adiabatic so no heat is transferred from the part wall to fluid, while ϕ is defined for conducting part walls such as real engine components or models which have been appropriately scaled in accordance with the matched-Bi method, of which a more detailed discussion will be given in Section 1.3.2.

1.3 Thermal Analysis of Actively Cooled Gas Turbine Components

This section presents a thermal analysis of gas turbine components with internal impingement and external film cooling. A basic one-dimensional analysis of heat transfer through a plane wall with film cooling and impingement cooling is performed in order to build a foundation for the matched-Bi method, followed by a discussion of the conventional thermal analysis method whereby convection heat transfer on the internal and external sides of the part wall are decoupled and treated separately.

1.3.1 Simplified 1-D Plane Wall Heat Transfer Analysis

Generally speaking, the geometries of film cooled gas turbine engine components are 3D and very complex in nature and therefore so is the heat transfer and resulting temperature distribution within the part. However, much information about the behavior of active cooling schemes may be gleaned by taking the simple case of a plane wall with film cooling, assuming 1-dimensional heat transfer through the wall and that the adiabatic wall temperature is the correct driving potential for heat transfer at the external surface. This allows for the application of a simple thermal resistance analogy, as shown in Figure 1.7, where the heat flux through the part wall may be related to the driving temperature difference by the resistance to heat transfer, in the same way that Ohm's Law relates electrical current to the driving voltage using an electrical resistance.

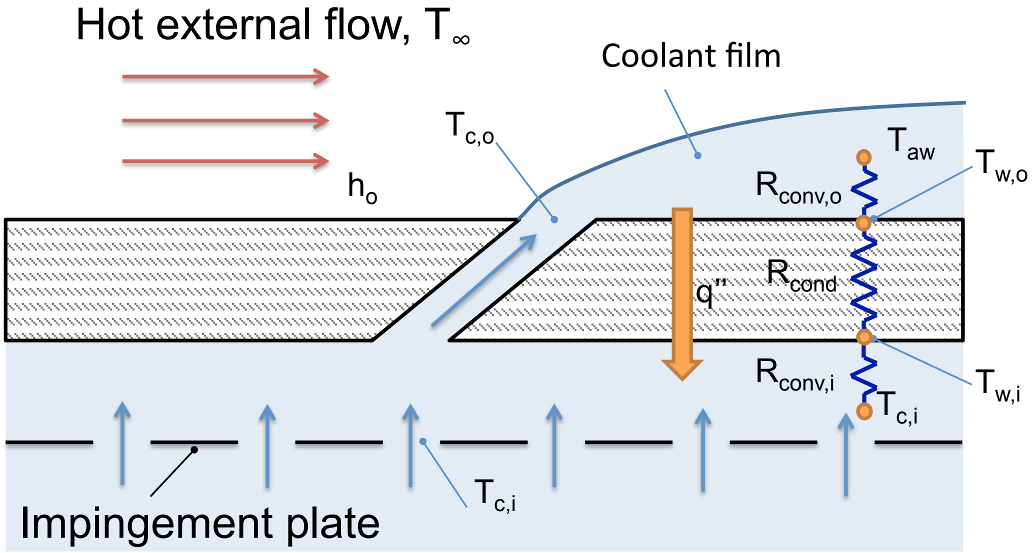

Figure 1.7: Application of the 1-D thermal resistance analogy to heat transfer to an actively cooled plane wall

In this case, there are three resistances to heat transfer involved: one associated with convection on each side of the part wall, and one associated with conduction through the wall. Adding these resistances in series and employing the analogy with Ohm's Law gives:

$$q'' = \frac{T_{aw} - T_{c,i}}{R_{conv,o} + R_{cond} + R_{conv,i}} = \frac{T_{aw} - T_{c,i}}{\frac{1}{h_f} + \frac{t}{k} + \frac{1}{h_i}} \tag{1.9}$$

Also, since the heat flux through the part is the same as the heat flux at the external surface, Newton's Law of Cooling may be employed at the external surface, resulting in the following relationship:

$$h_f\left(T_{aw} - T_{w,o}\right) = \frac{T_{aw} - T_{c,i}}{\frac{1}{h_f} + \frac{t}{k} + \frac{1}{h_i}}, \tag{1.10}$$

or

$$\frac{T_{aw} - T_{w,o}}{T_{aw} - T_{c,i}} = \frac{1}{1 + \frac{h_f t}{k} + \frac{h_f}{h_i}}. \tag{1.11}$$

Using the definitions of film effectiveness and overall effectiveness, as shown in Equations 1.3 and 1.8, respectively, it may be shown that

$$\phi = \frac{1}{1 + \frac{h_f t}{k} + \frac{h_f}{h_i}} \left(1 - \eta \frac{T_\infty - T_{c,o}}{T_\infty - T_{c,i}}\right) + \eta \frac{T_\infty - T_{c,o}}{T_\infty - T_{c,i}}. \tag{1.12}$$

Equation 1.12 may be simplified by defining a Biot number based on wall thickness and external heat transfer coefficient,

$$Bi = \frac{h_f t}{k} \tag{1.13}$$

and a dimensionless temperature, χ,

$$\chi = \frac{T_\infty - T_{c,o}}{T_\infty - T_{c,i}} \tag{1.14}$$

to relate the overall effectiveness to the adiabatic effectiveness and other system parameters:

$$\phi = \frac{1}{1 + Bi + \frac{h_f}{h_i}} \left(1 - \eta\chi\right) + \eta\chi. \tag{1.15}$$

The normalized temperature χ is a new parameter which appears for the first time as part of the analysis presented in this study. It is referred to as the "coolant warming factor" and its presence in in Equation 1.15 accounts for the fact that by the time the coolant is ejected from the film cooling holes it has already lost some of its film cooling potential due to pre-heating, since the coolant is continually warming as it passes through the internal passages before being ejected onto the external surface.

1.3.2 Importance of Matching Model Parameters for Film Cooling Experiments

In order to perform temperature measurements with a film cooled conducting vane model in a laboratory environment and measure normalized temperatures that are representative of an actual engine component, Equation 1.15 indicates that the Biot number must be matched, as well as the ratio of heat transfer coefficients and the dimensionless temperature at the exit of the coolant hole, χ. If either Bi or h_f/h_i of the experimental model is too large relative to a real engine component, then the measured values of ϕ will be low by comparison to a real component. Also, if χ for the experimental model is too large compared to a the engine component, then the measured value of ϕ will be higher than the real value. A similar analysis was performed by Albert (2003) and expanded on by Johnson (2008) in order to examine the relationship between film effectiveness and overall effectiveness. However, one major difference between previous analyses and the present study is the presence of the factor χ in Equation 1.15. Previous analyses assumed that the coolant ejected from the film cooling hole was at the same temperature as that at the inlet, for which χ would be unity; this may not always be appropriate, as will be shown using measurements from the current study.

Use of the matched-Bi technique is a relatively recent development. Sweeney and Rhodes (2000) implemented a matched Biot number (Bi) technique for measuring overall effectiveness of film-cooled double-wall flat plate specimens. Because the convective heat transfer coefficients for their experiment were approximately three times lower than those in an actual engine, a material was selected with a thermal conductivity lower than that of an actual engine component by a factor of close to three. Sweeney and Rhodes did not, however, account for the difference in physical scale between their test model and an actual engine component; the wall thickness of their test specimen was approximately three times larger than engine scale, which, by Equation 1.13, would make Bi for their model three times larger than that of an engine component (since they scaled k with h). Furthermore, no mention was made regarding whether or not the ratio h_f/h_i was matched.

1.3.3 Conventional Decoupled Analysis Method

While internal and external cooling of gas turbine engine components allows for higher gas temperatures at the inlet of the turbine, thereby increasing engine performance, the coolant comes at a cost. For industrial engines, between 12% and 15% of the total compressor flow is bled off as coolant airflow (Petchers, 2002), and up to 30% for advanced military engines (Bogard and Thole, 2006). The power used to compress the coolant and drive it through the engine components reduces the total amount of power produced by the engine. For this reason, considerable effort goes into the thermal design of gas turbine engine components. The geometries used are complex by design, so therefore the fluid mechanics and heat transfer are also complex.

During the design of gas turbine cooling systems, one of the ways that engine component temperatures are predicted for a particular cooling configuration is by using a 3-dimensional numerical simulation of conduction within the part wall using prescribed boundary conditions on each side of the part wall. Specifying convection boundary conditions on each of the wall surfaces effectively decouples the internal and external convection problems, which are frequently each studied as individual problems outside of the context of the entire system. While these numerical simulations can provide decent approximations of the temperature distributions, they rely on having accurate boundary conditions for inputs, and the boundary conditions themselves are regularly based on simplifying assumptions which can cause error in the results. For the external heat transfer problem, the assumption is often made that the adiabatic wall temperature is the correct driving potential for heat transfer through the wall. This greatly simplifies things, although doing so leaves out the effects of conjugate heat transfer on the system temperature. The internal and external convection problems are not truly independent in the physical system, and heat transfer on one side of the part wall can affect the heat transfer on the other side in ways that are not captured when the two sides are artificially decoupled.

The assumption that T_{aw} accurately represented the driving potential was computationally tested by Harrison and Bogard (2008), who used a series of CFD simulations of types of experiments commonly reported in the literature to predict heat flux and component temperatures, and compared those results to simulations of conjugate heat transfer. Their results found that the adiabatic wall temperature assumption gave reasonably accurate predictions of both surface temperatures and wall heat flux distributions for a conducting wall although there were differences of up to 10% in predicted surface temperature when using the conventional decoupled analysis method compared to the conjugate heat transfer simulation.

In order to experimentally assess the validity of the adiabatic wall temperature assumption, Dees et al. (2011a) measured the thermal boundary layer above the external surface for both matched-Bi and adiabatic vane models to determine if T_{aw} accurately represented the temperature of the gas just above the vane surface. This was done at a variety of locations and film coolant momentum flux ratios. He found that T_{aw} was a good representation of the gas temperature just above the vane surface for certain situations, such as regions downstream where film cooling jets remained attached to the surface of the model, and along the centerline of jets which had only slightly detached from the surface. However, in other instances such as near the edges of film cooling jets which were detached from the surface, the developing thermal boundary layer had a noticeable effect on the gas temperature above the wall, resulting in T_{aw} being a poor representation of the driving temperature for heat transfer to the surface in such regions.

Recent improvements in computational processing power have made it possible to numerically model the full conjugate heat transfer problem rather than just specifying the convection boundary conditions as per the conventional approach. To use CFD models including conjugate heat transfer to design with confidence, it is important to first validate the models against experimental data for known cooling configurations. Because the conventional approach has been to decouple the internal and external heat transfer problems making them easy to study individually, there have been numerous experimental studies on the performance of either internal or external cooling of gas turbine components. However, the number of experimental investigations into fully cooled conducting engine components reported in the open literature is limited. The earliest study of a conducting airfoil with internal heat transfer was performed by Hylton et al. (1983), who later incorporated the effects of film cooling into the same experimental setup (Hylton et al., 1988). Measurements were made using thermocouples attached to the surface of the vane at midspan, and internal cooling was predicted using correlations for a round duct. The experimental model was not designed to match either Bi or h_f/h_i, which would be necessary in order to measure ϕ values representative of an actual engine component. Because of the limited amount of experimental investigations into conjugate heat transfer, the experimental data from Hylton et al. has been used for comparison with many computation predictions despite limitations of the dataset.

More recently, a number of experiments employing the matched-Bi technique on film cooled turbine components have been conducted at the Turbulence and Turbine Cooling Research Laboratory ($TTCRL$) at the University of Texas at Austin. A scaled-up model of a blade leading edge with internal impingement cooling and three rows of film cooling holes was studied by Albert et al. (2004). The fused alumina ceramic from which the model was constructed was chosen to match Bi to conditions matching those of a typical engine, and overall effectiveness was measured for direct comparison with adiabatic effectiveness measurements made using a low conductivity foam model. His results showed that adiabatic effectiveness plots exhibited much stronger spatial gradients than were seen in overall effectiveness, due to conduction within the experimental model. The importance of conduction within the model was illustrated with a practical example by by blocking one film cooling hole and observing that in the absence of flow though the blocked hole, some amount of cooling was maintained by conduction through the part wall, and overall effectiveness decreased slightly and only in the near vicinity of the blocked hole.

Conduction through the wall of a film cooled component component in the vicinity of a film cooling hole can be largely a consequence of the high rates of convection heat transfer which can occur inside a film cooling hole as the coolant flows from the inside of the part immediately before being ejected as coolant. This convective heat transfer was investigated experimentally by Terrell et al. (2005) for a conducting leading edge model constructed of alumina to achieve Bi representative of an actual engine component. Coolant temperature profiles were measured at the inlet and exit of the cooling holes for calculation of the total rate of heat transfer as the coolant passed through holes in the leading edge model. Because the leading edge model tested had several rows of film cooling holes and no internal impingement cooling, it was seen that convection inside the film cooling holes accounted for about 50% of the total heat transfer at the lowest blowing ratios tested, and increased up to 80% at the highest blowing ratios tested.

The first conjugate heat transfer experiments reported in the open literature of a scaled-up turbine vane with engine-matched Bi and film cooling were performed by Dees et al. (2011b), who built and took measurements using the same basic C3X airfoil geometry as Hylton et al. although with different internal cooling and film cooling geometries. Dees et al. built both conducting and near-adiabatic vane models and used IR thermography to measure external overall effectiveness with and without film cooling provided by a single row of holes as well as adiabatic effectiveness. The row of film cooling holes was located in a high-curvature region on the suction side of the vane. Internal cooling was provided by a U-bend passage in the front section of the vane which also served to supply coolant for the film cooled case, and a radial passage was also used to provide internal cooling to the tail section of the vane. Tests were also performed to examine the impact of adding rib turbulators to these internal flow passages to augment the internal heat transfer coefficient. The total flow rate through the model could be adjusted independently of M to achieve various levels of internal cooling. In addition to overall and adiabatic effectiveness, Dees et al. also measured hydrodynamic and thermal boundary layers at several locations (2010), 2-D jet temperature profiles (2011a), external heat transfer coefficient for a constant heat flux boundary condition, and internal surface temperatures (2010).

Albert (2011) measured adiabatic and overall effectiveness for the an engine-matched Bi vane model with a "showerhead" film cooling configuration in the leading edge region as well as a single row of holes on the pressure side as part of a larger study to experimentally simulate the effects of contaminate deposition on film cooled parts. The study was performed in the same facility at the University of Texas as Dees' study, and also had the same simple internal cooling configuration. Both Dees and

Albert used a simplified 1-D heat transfer analysis similar to that shown in Section 1.3 to make predictions of ϕ based on ϕ_0 and η and found that the predicted values of ϕ compared reasonably well with the experimentally measured values except near the film cooling holes where the 1-D heat transfer assumption was likely violated and for high jet momentum flux ratios, where the jets would be fully detached from the vane surface.

1.4 Objectives of the Current Study

This thesis presents the methodology and results from four experiments involving an airfoil with a single row of film cooling holes which were performed in the early stages of a much larger experimental and computational study of a matched-Bi vane model with 13 rows of film cooling holes performed at the Turbulence and Turbine Cooling Research Lab at the University of Texas at Austin. The motivation for this smaller study derived itself from the goals of the larger study, which are discussed in this section.

When examining the open literature for experimental data for gas turbine cooling strategies, there are a few deficiencies which the current study aims to address. First, the problems of internal cooling and external film cooling are frequently decoupled from one another and are studied independently, and there have been very few experimental studies done with both internally and externally cooled gas turbine engine components with properly scaled thermal conductivity. While Dees et al. and Albert both measured overall cooling effectiveness distributions on matched-Bi vane models and film effectiveness using adiabatic vane models, the internal cooling for both of their vane models was provided by a simple U-bend passage with coolant flowing through the model. While Dees' model had a single row of holes and Albert's vane model had a single row of holes on the pressure side of the vane in addition to three rows of “showerhead” holes, the first stage stator vanes in a gas turbine engine regularly have many more rows of cooling holes, and commonly use impingement cooling to increase the heat transfer coefficient on the internal wall surface.

One primary goal of the project was to directly measure the overall effectiveness for a gas turbine vane with a more realistic (and much more complex) cooling configuration than has previously been studied. In order to measure overall effectiveness for a realistic gas turbine cooling configuration, a large-scale model was built with thermal properties chosen so that both Bi and the ratio of heat transfer coefficients would be representative of an actual gas turbine vane under typical engine operating conditions as described in Section 1.3. Building the model at a large scale made it possible to take measurements with greater detail than could be done with an engine test rig. The model was built and tested in stages of increasing complexity, and the final model had 13 rows of film cooling holes including five rows on the pressure side, five rows in the leading edge region, and three rows on the suction side. A large portion of the model was also cooled internally using an impingement plate, as opposed to the U-bend configuration with through flow which was used by Dees et al. and Albert.

It has been well established that (with the exception of “showerhead” cooling configurations) adiabatic film effectiveness decreases as the film cooling jet momentum flux ratio is increased beyond an optimal value due to the film cooling jets separating from the surface and penetrating into the mainstream flow (Bogard and Thole, 2006). The results of Dees et al. showed that when internal cooling was held constant while the mass flow rate of external film coolant was increased, overall cooling effectiveness dropped as the film cooling jets separated. However, other internal cooling configurations exist which would have internal cooling that increases along with I, so it was also desired to see if the trade-off between increasing internal cooling and decreasing film cooling due to jet separation created an optimal coolant flow rate which would be different from that for either internal or external cooling alone. To isolate the effects of the impingement cooling alone, a number of test cases were measured for which the middle two film cooling holes were taped over so that there was no film cooling over a small portion of the vane surface while the internal cooling circuit was still active. More details on the test rig and methodology will be discussed in Chapter 2.

Another objective of the larger encompassing project (beyond the scope of this thesis) was to computationally predict the conjugate heat transfer and temperature distribution throughout the same gas turbine vane component using CFD, and compare the computational results with the experimental measurements for overall and adiabatic effectiveness. This was done to assess how well a simple Reynolds-Averaged Navier-Stokes ($RANS$) model can predict the flow field and heat transfer through and around gas turbine components with complicated cooling configurations. Because of the complexity in building, testing, and computationally modelling the the fully cooled vane model with 13 rows of film cooling holes, it was determined that a simplified cooling configuration employing a single row of film cooling holes should be built and tested first as a way of bringing the experimental and computational models on-line. Once the experimental model and facilities had been debugged, more film cooling holes were added to the physical and computational vane models. This simplified experimental model which was initially tested is the subject of this thesis.

While there is very little data in the published literature for overall effectiveness measurements on a fully cooled, matched Bi vane model, there is even less data regarding internal temperatures. Therefore, it was desired to not only measure overall effectiveness, but also internal gas temperatures and inner wall surface temperatures as part of the current study in order to gain more insight to the behavior of the coolant as it flowed through the system, as well as making the data available for use in the validation of CFD schemes.

Chapter 2

Facility and Experimental Procedures

This chapter discusses the test facilities, hardware, and procedure used for the current study. Descriptions will be given of the wind tunnel and coolant supply system, as well as details regarding the construction and instrumentation of experimental airfoil models. The test procedure and subsequent data reduction techniques are explained and estimates of the experimental uncertainty are presented.

2.1 Experimental Test Facility

All experiments were performed using a recirculating (closed-loop) wind tunnel in the Turbulence and Turbine Cooling Research Laboratory (*TTCRL*) at the University of Texas at Austin, a schematic of which is shown in Figure 2.1. A

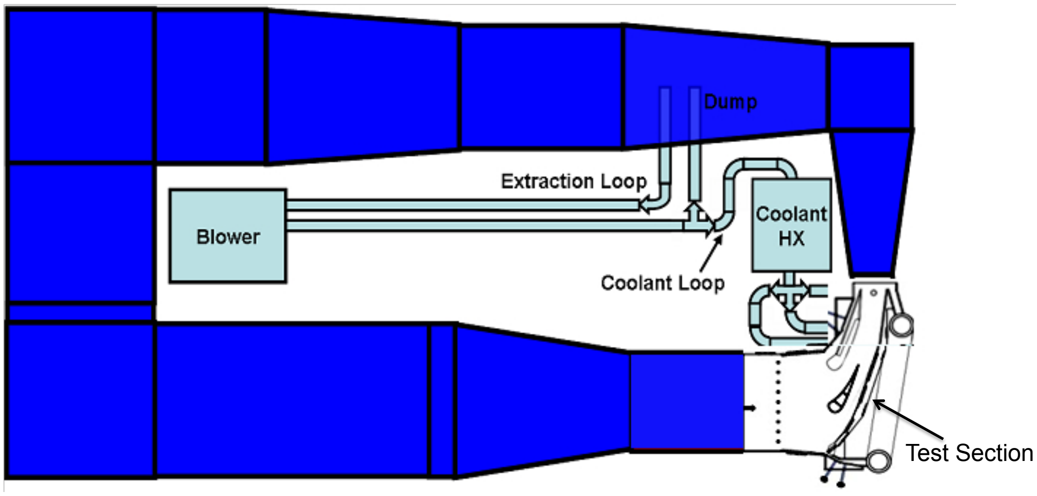

Figure 2.1: Schematic of closed-loop wind tunnel (From Albert, 2011)

50hp fan with adjustable speed and blade pitch was used to drive the flow inside the tunnel. Because temperatures in the coolant supply system and film cooled model were below the freezing point of water, high levels of humidity inside the wind tunnel would lead to the formation of frost in the test facility. Removable, reusable desiccant packs, supported by a rack just downstream of the fan, were used to dry out the air in the wind tunnel. The temperature of the air in the wind tunnel was regulated using an air-to-water heat exchanger, through which flowed a controlled mixture of hot and cold tap water. During overall effectiveness experiments, the mainstream temperature of the air in the wind tunnel was kept at $305K \pm 1K$.

After passing through the heat exchanger but before entering the test section, the flow passed through a series of honeycomb and screens then through a 4:1 contraction which served to reduce the the level of turbulence as well as the boundary layer thickness on the wind tunnel walls. The velocity at the inlet to the test section was measured using a Pitot-static probe.

Coolant was supplied to the vane model via a secondary flow loop, which worked by drawing some of the mainstream flow out of the primary loop using a blower and passing it through a liquid-to-air heat exchanger which used liquid nitrogen to cool the secondary flow down to the appropriate temperature. After exiting the heat exchanger, the coolant was split into two separate supply ducts, each feeding a different coolant passage in the vane model, and each equipped with an orifice flow meter and control valve so that the coolant flow rates could be varied independently for each plenum. A schematic of the coolant supply system is shown in Figure 2.2.

The wind tunnel test section consisted of a simulated 3-vane cascade, and was constructed by Dees et al. (2009). The vane geometry used had the same external profile of the NASA C3X vane which was used by Hylton et al. (1983), although the

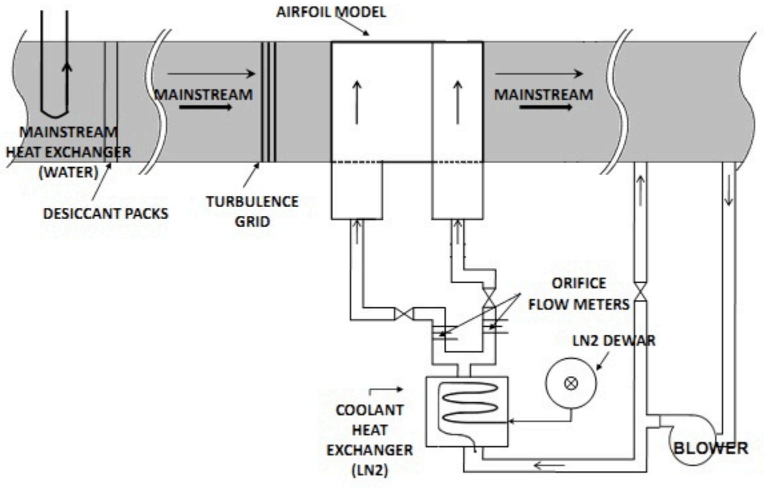

Figure 2.2: Schematic of secondary coolant supply system

scale of the vane was increased by an additional factor of 3.88 to match the vane pitch in the existing the existing TTCRL test section cascade. A diagram of the test section is shown in Figure 2.3, and some of the relevant test section parameters are listed in Table 2.1.

Table 2.1: Test Section Parameters

Parameter	Value
Chord Length (C)	53.1 cm
Vane Span	54.6 cm
Vane Pitch	45.7 cm
Turning Angle	72°
Inlet Velocity (U_∞)	5.8 m/s
Exit Reynolds Number (Re_C)	7.5 x 10^5

The test section was constructed out of clear acrylic, with numerous ports cut through which were used to mount a zinc selenide infrared viewing window for the use of infrared thermogrpahy to measure surface temperatures. The center vane in

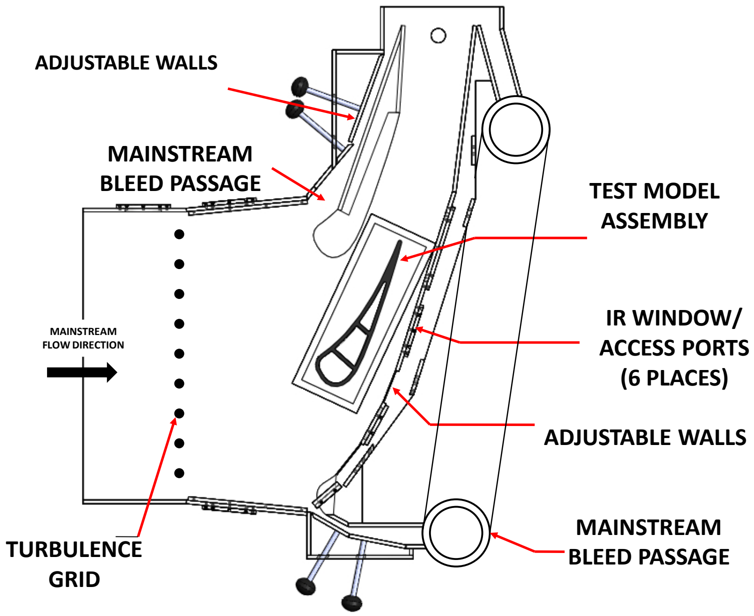

Figure 2.3: Wind tunnel test section designed by Dees et al. (2009).

the simulated 3-vane cascade was used for active cooling measurements, while the inner and outer simulated vanes provided adjacent suction and pressure surfaces, respectively. The outer walls of the test section were adjustable, and by changing their position the velocity and pressure distribution around the vane model could be adjusted as will be discussed later. The outer two vanes in the cascade had adjustable flow bypasses which were used to set the location of the stagnation lines independently on each vane. Freestream turbulence intensity levels of approximately $Tu = 0.5\%$ existed upstream of the test section entrance before passing through a set of removable vertical rods which generated the desired turbulence characteristics in the approach flow.

Because Dees et al. had constructed a new test section in the corner of the existing $TTCRL$ wind tunnel for his study, former undergraduate lab assistant Yoran Pinchon measured the uniformity and turbulence characteristics of the approach flow using a hot wire anemometer in order to verify that they matched measurements taken by previous graduate student Marcus Polanka using a 3 component laser doppler velocimetry in the previous test section. Pinchon (2009) found that the average mainstream turbulence level was $Tu = 20\%$ with an average turbulence integral length scale $\Lambda_f = 37mm$, measured $0.26C$ upstream of the test vane, where C is the chord length of the airfoil. The uniformity of the turbulence intensity and integral length scale measured by Pinchon are shown in Figures 2.4 and 2.5, respectively, while the three-component LDV measurements taken by Polanka in the previously used test section can be seen in Figure 2.6.

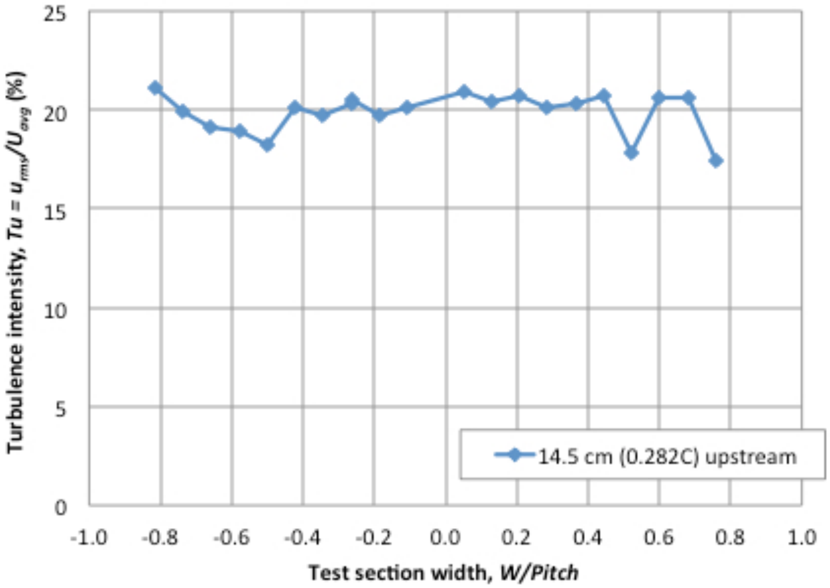

Figure 2.4: Lateral uniformity of approach flow turbulence intensity (from Albert, 2011)

The test section was designed to be modular, such that different vane models could be easily swapped in and out for different testing configurations. Each vane test model tested was attached to two large rectangular mounting plates, which secured

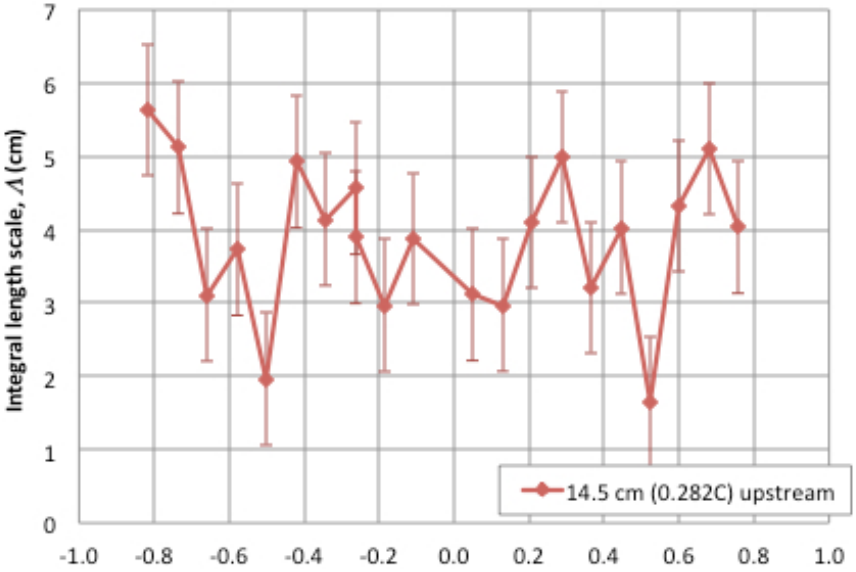

Figure 2.5: Lateral uniformity of approach flow turbulence length scale (from Albert, 2011)

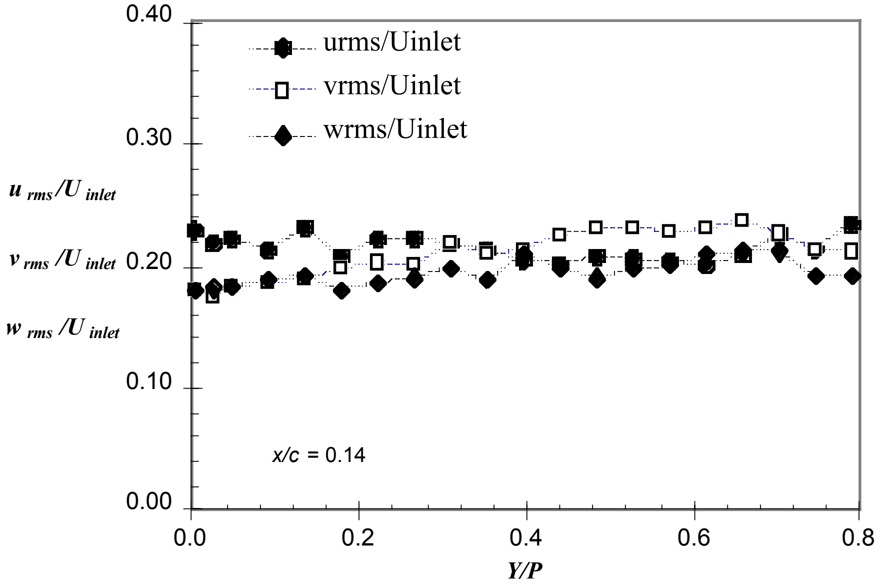

Figure 2.6: Lateral uniformity of approach flow turbulence levels originally measured by Polanka (from Ethridge et al., 2000)

to the top and bottom walls of the test section. A schematic of the removable vane module is shown in Figure 2.7. Once installed in the wind tunnel, the bottom plate was bolted down using counter-bored machine screws so that the bottom plate was flush with the floor of the test section. To prevent thermal strains from stressing the test models, the top plate was designed to have a very slight slip-fit, so that the vane was able to expand or contract a small amount in the span-wise direction but was otherwise constrained from moving. A rubber gasket and high-vacuum grease (Dow-Corning) were used to seal the interface between the vane model and coolant supply duct.

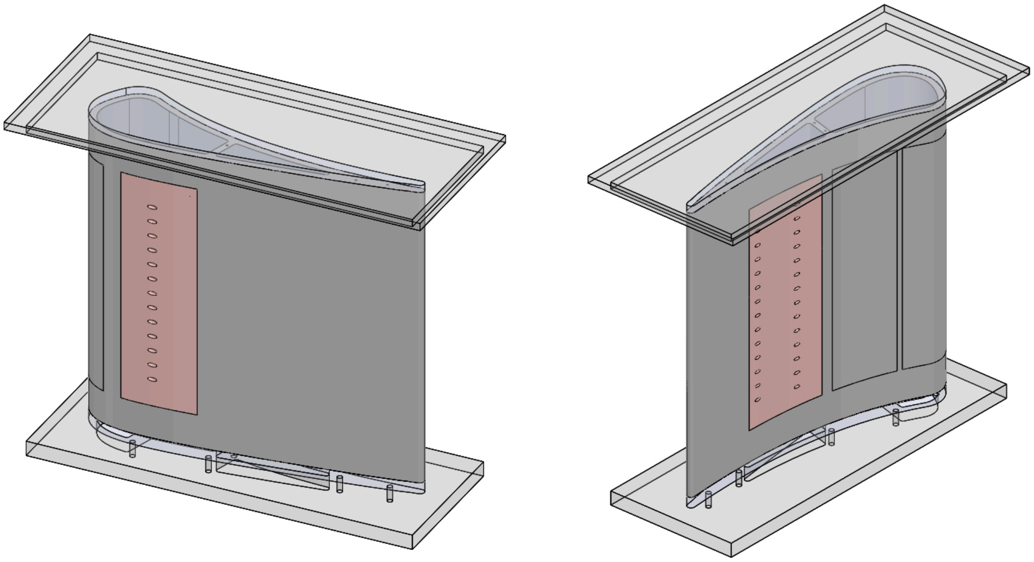

(a) Suction side

(b) Pressure side

Figure 2.7: CAD model of removable vane module with mounting plates

2.2 Vane Test Models

Three different airfoils were used to take measurements over the course of this project, although only two were tested as part of this thesis. For each vane model built and tested, the external airfoil geometry was the same NASA C3X geometry of Hylton et al., scaled up by an additional factor of 3.88. Specific models were built with differences in material, cooling configuration, and instrumentation, depending on the particular measurements collected.

2.2.1 Airfoil with surface pressure taps

The first vane model used was a polyurethane model with no internal flow features and which was instrumented with surface pressure taps, originally constructed by Dees et al. (2009) as part of his study. The particular grade of polyurethane foam was selected for its low thermal conductivity of $k = 0.048W/m - k$ in order to make adiabatic effectiveness measurements (which are beyond the scope of this study). The surface pressure taps were used to measure the surface pressure distribution around the model while making adjustments to the wind tunnel outer wall position and adjustable bypass flows in order to tune the stagnation line location and surface pressure distribution to that predicted using CFD analysis performed by fellow graduate student Tom Dyson — the experimental procedure for this is discussed in further detail in a subsequent section of this thesis.

2.2.2 Matched Bi Airfoil with Internal Impingement and External Film Cooling

The vane model which was the primary subject of this thesis was a fully conducting airfoil with a single row of film cooling holes on the suction side and two rows of film cooling holes on the pressure side, and a realistic internal impingement cooling configuration. The vane was designed in accordance with the matched-Bi method discussed previously in Section 1.3.2. The vane was constructed out of Dupont Corian® material, chosen for its specified thermal conductivity of $k = 1.06W/m - K$.

The thermal conductivity was also measured at $TTCRL$ and found to be $k = 0.97 \pm 0.1 W/m - K$ Because the material was readily available in sheets with a thickness of 19mm, the vane was constructed by machining sections with the airfoil profile in the thickness of a Corian sheet, then stacking and gluing them together using a special Corian glue with dowel pins for alignment.

In order to add the flexibility of being able to test many different film cooling hole geometries and configurations during subsequent studies without having to build entirely new vane models, the vane model was constructed with five different removable "hatches" into which the film cooling holes were machined, so that adding, removing, or modifying the film cooling holes just became a matter of changing hatches. The removable hatches were fastened to the vane model using threaded fasteners and a sealant paste of an appropriate thermal conductivity. Figure 2.8 is a CAD image of the vane body, showing the stacked 19mm thick Corian layers and openings for the removable "hatches".

2.2.2.1 Internal Cooling Geometry

Internal cooling of the vane was provided by two different internal passages which were both designed to achieve the correct ratio of internal to external heat transfer coefficients as required by the matched-Bi method. A schematic showing the locations of the two internal coolant passages is shown in Figure 2.9. The first passage, extending from the leading edge region to approximately mid-chord, employed an internal impingement plate in order to augment the internal heat transfer coefficient and provide a realistic internal cooling configuration. All of the coolant which passed through this front passage was ultimately ejected as film coolant from a single row of film cooling holes on the suction side of the model. The impingement plate was designed to provide a realistic internal cooling condition on the inner vane wall in

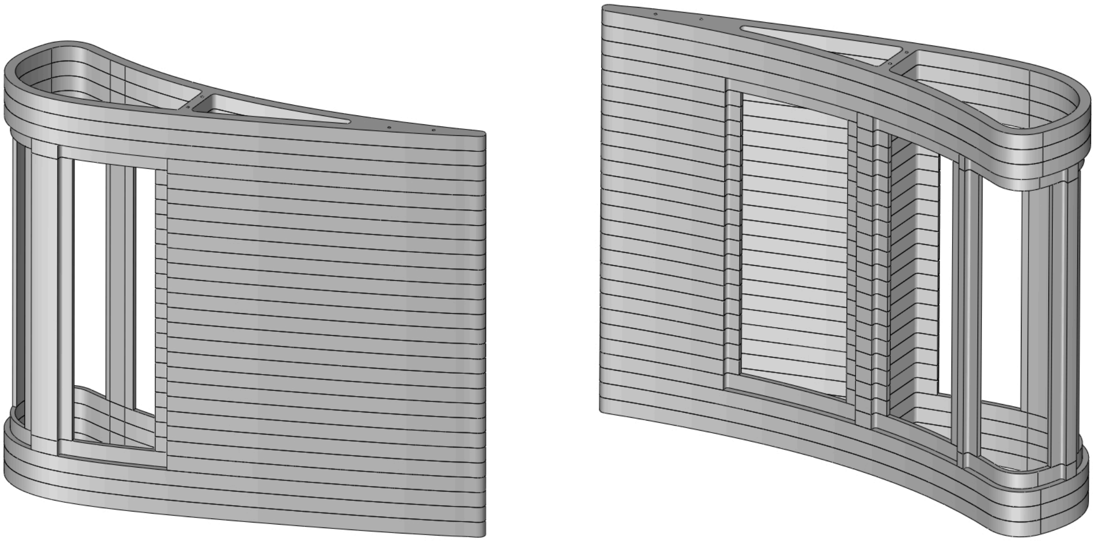
(a) Suction Side (b) Pressure Side

Figure 2.8: CAD illustration of vane body composed of laminated layers with openings for removable "hatches"

accordance with the matched-Bi approach.

The aft passage was a simple radial channel with no impingement plate, feeding two rows of film cooling holes on the pressure side of the model. Because all of the coolant entering the model was ejected as film coolant, the flow rate of the coolant through the model was determined by the desired coolant momentum flux ratio, which in turn determined the internal heat transfer coefficient. This was a significant departure from the model used by Dees (2010), whose internal coolant passages were designed such that the internal flow rate could be varied independently from the film cooling jet momentum flux ratio.

2.2.2.2 Film Cooling Geometry

As mentioned, the vane model included film cooling holes on both the pressure and suction sides of the airfoil. The suction-side holes provided the film cooling which

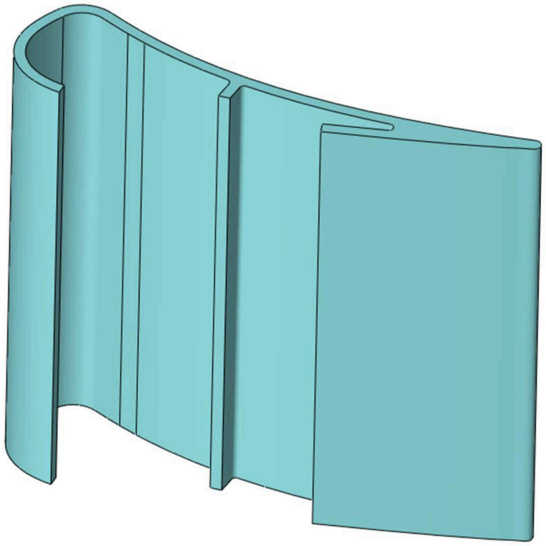

Figure 2.9: Cutaway of vane model showing difference between the fore (left) and aft (right) internal coolant passages

is largely a subject of this thesis, and are shown in Figure 2.7a. This row of holes was located at a surface distance downstream of the stagnation line of $s/C = 0.512$. The holes had a diameter of $d = 6.35mm$, a hole-to-hole pitch/diameter ratio of $p/d = 4$, and formed an angle with the surface tangent of the vane in the stream-wise direction of $\alpha = 25°$. The vane surface was relatively flat in the region where the holes were drilled, having a relative radius of curvature of $2r/d = 260$, where r is the radius of curvature for the vane surface.

2.2.2.3 Internal Instrumentation

For the measurement of temperatures inside the airfoil, the vane model was instrumented with a number of E-type thermocouples. It was desired to measure the temperature of the coolant at various positions inside the model along the coolant flow path, as well as the temperature of the inner vane wall surface in the film-cooled region.

For measurement of the inner wall surface temperature, five E-type ribbon thermocouples (chosen for their suitability to measuring very low temperatures) were carefully attached to the inner surface using a small amount of epoxy. Ribbon type thermocouples were used because their flat geometry allows for good thermal contact with surfaces for measuring surface temperature, and their low profile when attached to the surface keeps any disturbance to the flow passing over them to a minimum. The locations of these five surface thermocouples relative to the position of the row of film cooling holes, viewed from the exterior of the vane hatch, may be seen in Figure 2.10. All of the thermocouples were positioned on the surface of the vane wall directly across from an impinging jet so that they would ideally all be in the middle of a region of very high convection heat transfer, with the exception of thermocouple "B" which was positioned on the vane surface exactly mid-pitch between a set of impinging jets. The reason for placing thermocouple "B" between the impinging jets was to ascertain if a spatial variation existed on the inner wall surface between the adjacent rows of impinging jets which would not otherwise be captured if all of the surface thermocouples were located directly in the center of an impinging jet.

The temperature of the coolant flowing through the model was measured at several locations along the coolant flow path. These locations, shown in Figure 2.11, included the middle of the coolant inlet at the base of the model, the middle of the plenum feeding coolant to the front passage impingement plate, the center of an impinging jet hole, the impingement cavity formed between the impingement plate and the inner wall surface, the center of the inlet to a film cooling hole, and near the edge of the inlet to a film cooling hole. A pair of ribbon thermocouples were attached to the downstream surface of the impingement plate, near the impinging jets which were instrumented to compliment the gas temperature measurements. Even though very small bead-type thermocouples were used to measure the gas temperature, it

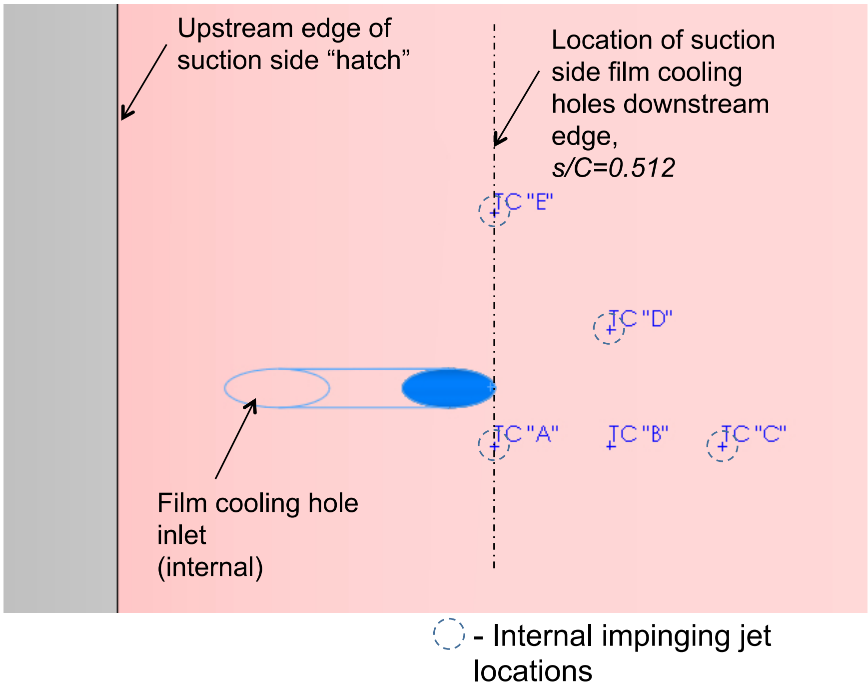

Figure 2.10: Location of internal wall surface thermocouples, viewed from the exterior of the vane

was desired not to disturb the flow field near the film cooling hole inlets or the region of the vane being imaged by the IR camera, so this arrangement of thermocouples was installed at two different span-wise positions in the model: one set of thermocouples was placed just above the region of the vane model being imaged, and one set of thermocouples just below the region of the vane model being imaged; these positions are shown in Figure 2.12.

2.3 Measurement Hardware

Experimental measurements were made using a digital data acquisition system connected to a number of thermocouples and pressure transducers, as well as an infrared thermography system. The purpose of this section is to provide details on

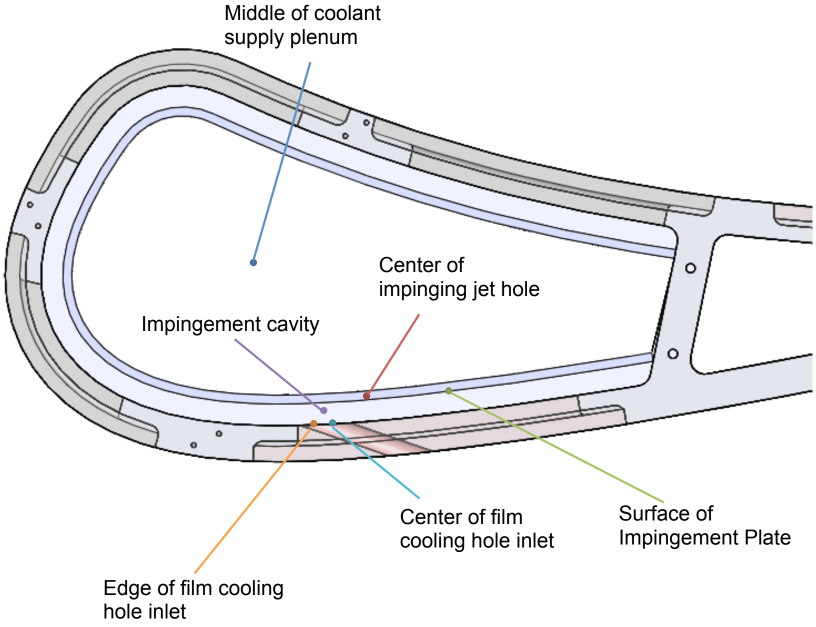

Figure 2.11: Configuration of internal coolant thermocouples

this equipment and it's usage.

2.3.1 Digital Data Acquisition System

In addition to the thermocouples with which the vane was instrumented, E-type thermocouples were also used to measure the wind tunnel mainstream temperature and temperatures at several locations throughout the coolant supply loop. The task of thermocouple and pressure transducer data acquisition was performed by a DAQ system built around a National Instruments PCI-6023E analog/digital interface card, connected to an NI-SCXI signal conditioning and multiplexing amplifier system. Thermocouple voltages were conditioned using SCXI-1102 input modules, and pressure transducer voltages were conditioned using one SCXI-1100 input module. The hardware was controlled using a program coded in LabView. Data collection was a

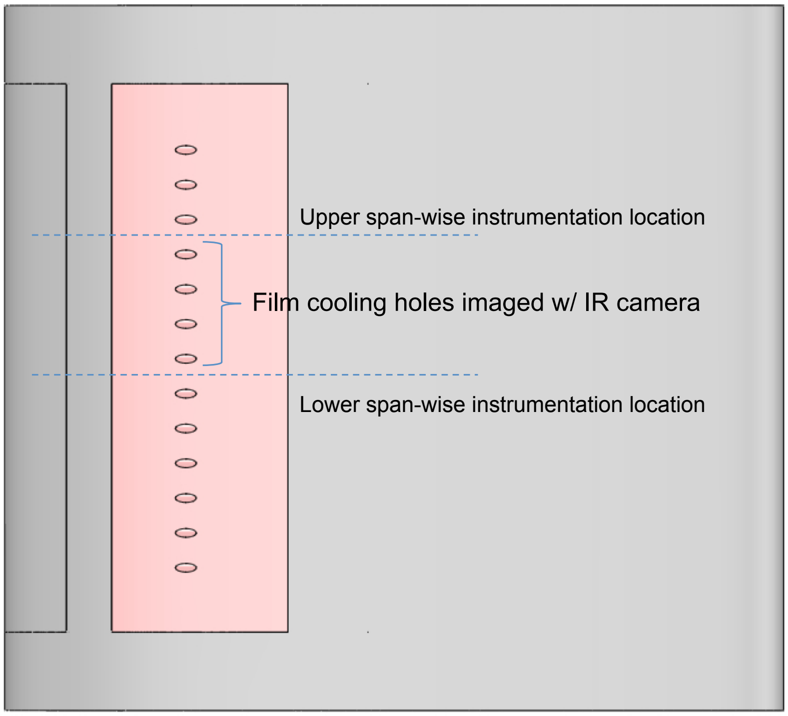

Figure 2.12: Two different span-wise positions, each instrumented with the thermocouple arrangement shown in Figure 2.11

semi-manual process, in the sense that taking a data point was achieved by clicking a "save data" button on the LabView virtual instrument user interface, at which time the DAQ system would sample data for two seconds at a rate of 2000 Hz, average the values, and record average measurement values to a text file.

2.3.2 Pressure Transducers

The Pitot-static probe dynamic pressure used to monitor the mainstream wind tunnel velocity was measured using an Omega Engineering PX2650-0.5D5V pressure transducer, which had a range of 0 to 0.5 inH_20 (or 0 to 0.124 kPa). Omega Engineering PX164-005D5V pressure transducers with operating ranges from 0 to 5.0 inH_20 (or 0 to 1.24 kPa) were used to measure the pressure drops across the coolant supply orifice flow meters, as well as for taking surface pressure measurements around the airfoil. The static pressure in the coolant supply line was measured using an Omega Engineering PX142-001D5V with a measurement range from 0 to 27.7 inH_20 (or 0 to 1.24 kPa) .

Although the pressure transducer manufacturer supplied a “standard” calibration for each pressure transducer, the uncertainties specified were unacceptably large with respect to the pressures measured for the current study. For this reason, each pressure transducer was calibrated by applying a pressure to the transducer input ports using a squeeze bulb, measuring the pressure with a Meriam micro-manometer, and taking a measurement of the pressure transducer voltage using the DAQ system. The calibration curve for the pressure transducer used to measure the coolant flow rate through the fore plenum is shown in Figure 2.13.

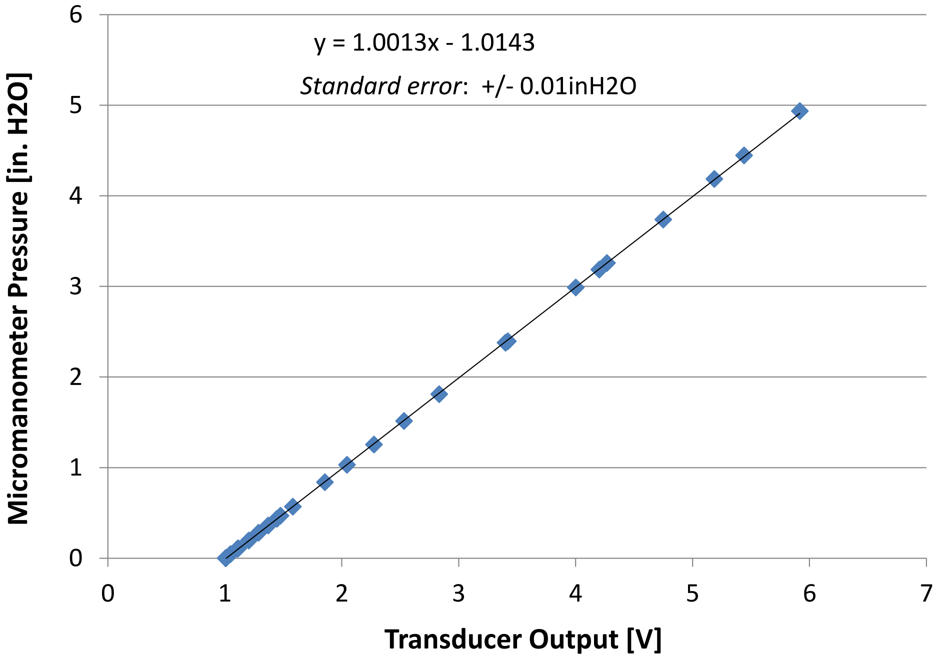

Figure 2.13: Calibration curve for pressure transducer used with orifice flow meter

During testing it was noticed that over the course of the film cooling experiments, the pressure drop measured across the orifice flow meter by the pressure transducer did not always return to zero when the coolant flow was shut off, indicating the presence of a bias drift in the pressure transducer output. In order to account for as much of this drift as possible, the coolant supply was shut off after the measurement of each test condition during film cooling experiments, and the zero bias was recorded and subtracted from the pressure measurements.

2.3.3 IR Thermography

The temperature distribution over a portion of the external vane surface on the suction side was measured using an infra-red thermography technique developed and refined at $TTCRL$. A FLIR Systems P25 infra-red camera was used to capture images of the vane surface in which the value of each pixel represented the surface temperature at that location. To achieve a high emissivity of the vane model surface, the vane model was painted with a matte black spraypaint. Because the walls of the test section were essentially opaque to IR radiation, a zinc selenide window was installed into a port in the test section wall to give the P25 camera IR optical access to the vane surface. Figure 2.14 shows the position of the camera relative to the vane model in the test section. During preliminary facility testing it was noticed that the IR camera was picking up reflections of other objects in the lab (body heat from the author and his labmates, in particular) in addition to the target surface of the vane model, so several cloths were draped over the wind tunnel and camera tripod to eliminate these reflections in the IR images.

Because the temperatures measured in the current study were lower than those which the P25 camera was intended to measure according to the manufacturer specifications, as well as the fact that the transmission of the ZnSn window was only

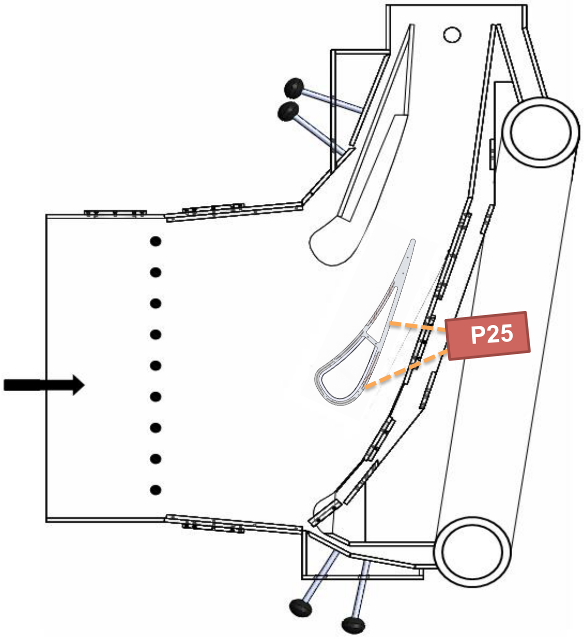

Figure 2.14: Position of IR camera relative to test model

about 70% in the range of IR wavelengths being captured by the camera, the temperatures reported by the P25 camera showed an unacceptably large error of up to $15K$ when compared to direct temperature measurements using ribbon-type thermocouples attached to the vane surface. Therefore, a calibration procedure was developed to remove this bias error from the IR temperature measurements. The calibration procedure involved making direct temperature measurements using ribbon-type thermocouples glued to the surface of the vane in the field of view of the camera, which were painted flat black to match the rest of the vane surface. These direct surface thermocouple measurements were compared against the IR camera temperature measurement at the pixel locations of the thermocouples in the IR camera output image, and a least-squares polynomial fit was used to generate the calibration curve from two sets of temperature measurements. The IR calibration correlation was then used to post-process all the temperature of each pixel in all of the IR images, using Mat-

Lab codes developed at *TTCRL*. The IR calibration curve fit used in the current experiment is seen in Figure 2.15.

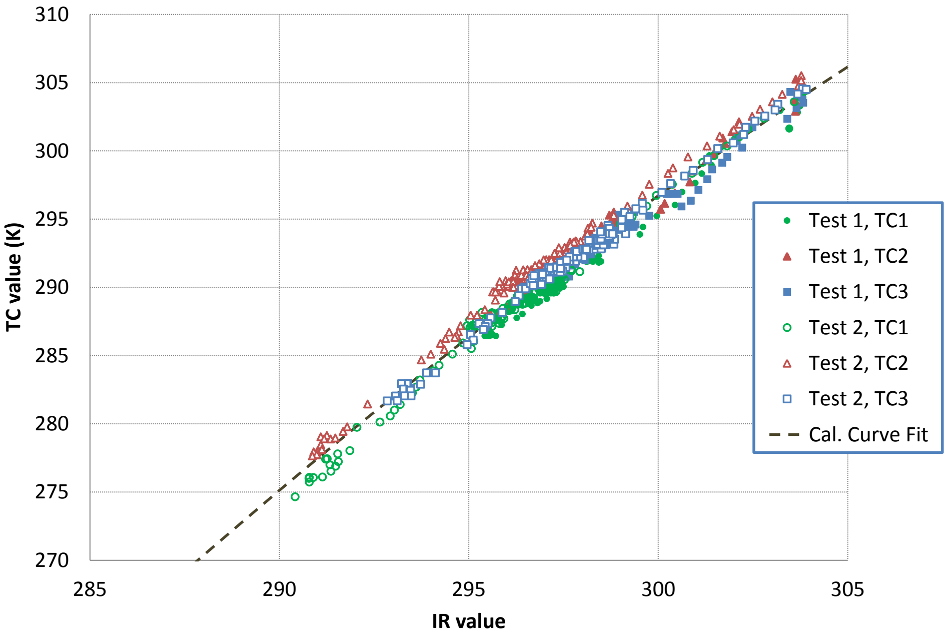

Figure 2.15: Calibration curve used to post-process IR camera images

2.4 Experimental Procedures and Data Reduction

Before thermal data could be collected, the surface pressure distribution around the vane model had to be adjusted. This section describes how and why this was done, as well as the procedure for measuring surface temperatures and reducing the data into the desired form.

2.4.1 Adjustment of Stagnation Line Location and Pressure Distribution

During preliminary testing, it was noticed that the adjustable tunnel walls appeared to have shifted from the location originally set by Dees et al. as part of his study, which could have caused a shift in the pressure distribution around the model airfoil and the location of the stagnation line on the leading edge portion. For this reason, a polyurethane model with pressure taps, previously discussed in Section 2.2.1 was used to re-measure the surface pressure distribution around the vane while flow visualization “tufts” were used to identify the position of the stagnation line on the leading edge. Images of the tufts positioned on the leading edge of the model airfoil are shown in Figures 2.16 (a) and (b). Figure 2.16 (a) shows the tufts hanging down in the neutral position with the wind tunnel off, while Figure 2.16 (b) shows the position of the tufts with the wind tunnel on, with a single tuft hanging straight down at the approximate location of the stagnation line. When the stagnation line moved a little further to one side or the other, the tuft would blow to the opposite side of the airfoil.

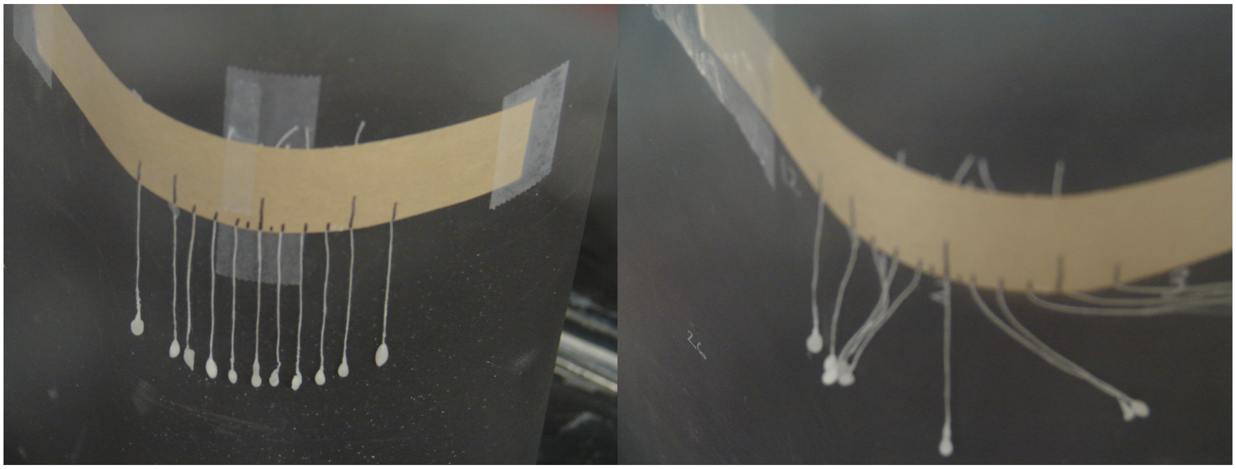

(a) Wind tunnel off

(b) Indicating stagnation line location

Figure 2.16: Use of flow visualization “tufts” to determine stagnation line location

Measuring the pressure distribution was done by operating the wind tunnel at a mainstream approach flow velocity of 5.8 m/s while measuring the pressure at each surface pressure tap around the airfoil, as well as measuring the static pressure from a Pitot-static probe used to monitor the mainstream flow velocity just upstream of the vane model. The measured pressure distribution was compared with CFD results from fellow graduate student Tom Dyson, who simulated the vane geometry used for the current study in an infinite cascade. The measured pressure distribution differed enough from the CFD simulation results to confirm that the wind tunnel walls had indeed shifted, and adjustments would have to be made to the wind tunnel wall positions and test section flow bypass bleeds in order to match the correct pressure distribution.

Tunnel wall adjustments were made by turning the threaded adjusting rods to move the wall in or out while continuously monitoring the surface pressures around the vane while using flow visualization tufts to identify the stagnation line position as it was moved. The adjustable bypass bleeds had the primary impact of changing the stagnation line position with a weaker effect on the overall pressure distribution, while moving the walls primarily changed the pressure distribution with subtle changes to the stagnation line position as a secondary effect. Making adjustments was an iterative process because of the number of wind tunnel adjustment points, with smaller and smaller changes required as the pressure distribution and stagnation line position approached the target values. The final pressure distribution measured after making all wind tunnel adjustments was normalized into C_p using the definition of the coefficient of pressure,

$$C_p = \frac{P - P_\infty}{\frac{1}{2}\rho U_\infty^2}, \tag{2.1}$$

where P_∞ was the static pressure of the approach flow near the inlet of the test section. The resulting distribution is shown in Figure 2.17, along with the target distribution found using CFD modelling. It is seen that the target distribution and the measured distribution begin to disagree at a surface distance downstream of the stagnation line of $s/C = 0.7$; this is because the adjustable wind tunnel wall responsible for setting the pressure distribution downstream of $s/C = 0.4$ was not adjustable in small enough sections to dial the pressure in over the whole range, so the distribution was matched near the film cooling hole exit at $s/C = 5.12$.

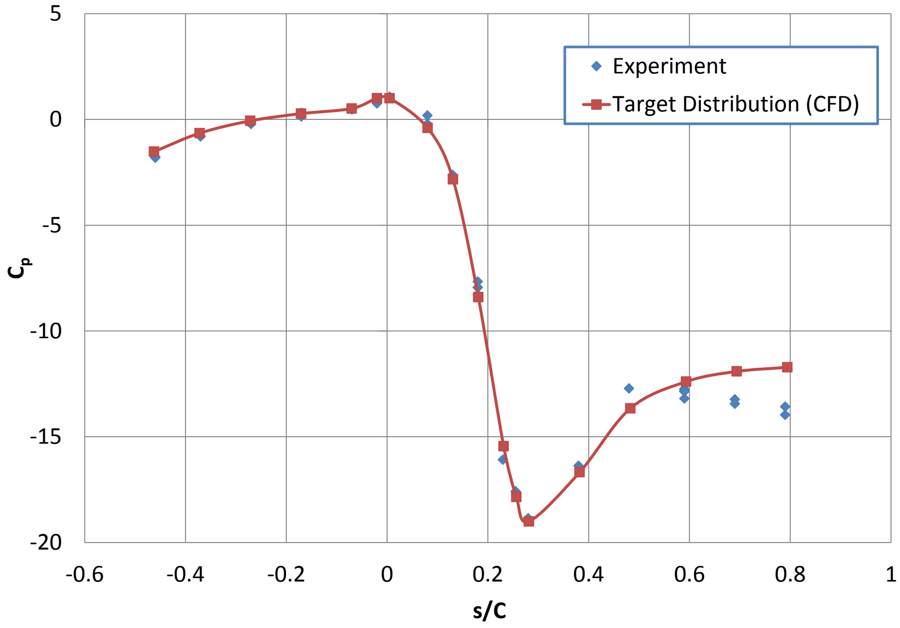

Figure 2.17: Measured surface pressure distribution after adjusting wind tunnel walls

A mistake was later discovered in the post-processing of the CFD data which had been used: the stagnation line was set erroneously 5mm too close to the nose, although the pressure distribution had been adjusted to match the target distribution. Because the suction side film cooling holes studied were located relatively far downstream of the leading edge beyond the location of transition from a laminar to turbulent boundary layer, the effect of this error in the stagnation line position should be negligible.

2.4.2 Thermal Test Procedure

In order to measure internal and external gas and surface temperatures for our matched-Bi vane, the polyurethane vane model used for pressure distribution measurement had to be removed and replaced with the conducting vane model. After installing the vane and connecting each of the thermocouples to the DAQ system, the temperatures reported by each of the thermocouples were checked to ensure that no wires were broken during the installation procedure.

Setting up the IR camera in the correct viewing position was critical to seeing as much of the vane surface as possible. To aid in alignment of the camera with the vane model and ZnSn viewing window, fine "tick" marks were drawn on the vane surface using a silver paint pen. Because the marks were silver on the flat black surface of the vane model, their different emissivity made the marks visible in the IR camera's viewfinder. Silver marks were also used to focus the camera, and to indicate the position of the surface thermocouples used for IR camera calibration. Once the camera was positioned using the silver tick marks so that the desired region of the vane surface could be clearly seen in the IR image, cloths were draped from the wind tunnel to the camera to cut down on reflected radiation.

Thermal tests were performed at a target mainstream approach flow velocity of $U_\infty = 5.8 \pm 0.05 m/s$, monitored in LabView from Pitot-static probe measurements, and a target temperature of $T_\infty = 305 \pm 1K$, regulated by changing the flow rate of hot water passing through the wind tunnel's water-to-air heat exchanger. It must be noted that even though these tolerances on the nominal approach conditions may seem loose, these were simply the target values used to control the equipment during the experiment and the actual measurements were made with much greater precision for the purposes of data reduction. Because temperatures in the coolant supply system and vane model were often below 273 K, frost would accumulate and create problems if the air in the closed-loop wind tunnel wasn't sufficiently dry to prevent it. For this reason, the air in the wind tunnel was replaced and dried though a two-part procedure which involved first purging the wind tunnel of the majority of humid air inside and then further drying using desiccant. The first part, purging, was done by operating the tunnel with one small port open while dry nitrogen was pumped into the tunnel, displacing the humid air inside. The relative humidity was monitored during this purge process, and would typically decrease from an initial value of up to 50% relative humidity, R.H., down to a value around 10 % before the desiccant was used. The desiccant was of a molecular sieve variety, reusable by heating it above the boiling point of water. The desiccant was contained by large mesh and expanded metal "packs" which could be transported between the wind tunnel and an oven which was used to dry out the desiccant packs before and after use. Once the relative humidity in the wind tunnel had dropped to about 10%, the wind tunnel was temporarily stopped and the desiccant packs were loaded into a rack just downstream of the fan.

After installing the desiccant packs, the wind tunnel was re-started and continued to operate while the humidity dropped a few more percent, at which point the process of cooling down the vane model was begun. The blower providing pressure to the the secondary flow loop was activated, and the coolant supply valves were opened which allowed gas to flow through the secondary flow loop heat exchanger and into the vane model. At this point liquid nitrogen was from a set of dewars was supplied to the coolant supply heat exchanger in the secondary flow loop, cooling down the gas flowing into the airfoil model. This also had the effect of further decreasing the relative humidity in the wind tunnel, as moisture in the air passing through the heat exchanger condensed and became trapped as ice in the heat exchanger. At the beginning of data collection, the relative humidity inside the wind tunnel had dropped to 6.6 % RH.

The LabView program used to collect the data was used to monitor system temperatures and flow rates in real time, and was also designed to calculate and show the relevant film cooling parameters such as DR and the film cooling jet-to-mainstream momentum flux ratio, I, for the film cooling holes on the suction side and pressure side of the airfoil. The flow rate of liquid nitrogen through the coolant supply heat exchanger was varied in order to regulate the temperature of the coolant flowing into the model to maintain the desired coolant-to-mainstream gas density ratio of $DR = 1.20 \pm 0.01$ for all but one test condition which was done at $DR = 1.4$. During post-processing of the data an error was found: the wrong thermocouple channel was specified for the coolant temperature, T_c used by LabView to calculate and display DR for monitoring during the experiment. The actual density ratio was $DR = 1.14 \pm 0.02$ when the correct thermocouple was used. The mass flow rate of coolant through the model was controlled by manually opening or closing the supply valves in order to maintain the desired I value for each test condition. The momentum flux ratio for the two rows of holes on the pressure side was maintained at a nominal $I_{PS} = 1.63$, while the momentum flux ratio for the suction side row of holes I_{SS3} was varied over a range of desired target values. Collecting temperature data for each test condition required setting the necessary coolant temperature and flow rates to achieve the desired I_{SS3} and DR value, and waiting for the vane model temperatures to reach steady-state. The pressure inside the liquid nitrogen supply dewars fluctuated enough that keeping the desired conditions steady during the experiment was often a juggling act which involved constantly adjusting and re-adjusting valves controlling the coolant flow rates and temperature. Once conditions had stabilized, a data point was collected every few minutes for at least 15 minutes by pressing the image capture button on the Flir P25 IR camera and simultaneously clicking the "capture data" button on the LabView interface. The reason for collecting at least 15 minutes worth of data was to be able to verify that steady state had indeed been reached during post-processing of the data. After collecting a sufficient amount of data at each test condition, the coolant supply valves were shut in order to record the drift in the zero bias of the pressure transducers, and the valves were re-opened and tunnel conditions were adjusted to those desired at the subsequent data point in the test plan.

In order to isolate the effects of internal impingement cooling and external film cooling, several test conditions were measured with the middle two film cooling holes taped over so that no film coolant was ejected over a portion of the vane surface. No other changes were made to the test procedure for these simulated "internal cooling only" data points, and the total coolant mass flow rate was matched to that of several of the un-taped cases. For these cases where the holes were taped over, the momentum flux ratio loses significance as a physical film cooling parameter except as a measure of mass flow - for simplicity, I_{SS3} was calculated and monitored during the experiment as if the middle two holes had remained un-taped.

The majority of the data discussed in this thesis came from a single experiment, with three data points from a second experiment which were used to assess the test-to-test repeatability. Table 2.2 lists the test conditions covered during the primary experiment in the sequence that they were performed in, including two in-test repeat points of the initial test case. It must be emphasized that while only one test was responsible for providing the majority of the data discussed here, a total of five thermal experiments were conducted over the course of the study, the first three of which were used to check the operation of the facility after installing the new conducting airfoil model and making some changes to the secondary flow loop responsible for supplying coolant to the model.

Table 2.2: Sequence of test conditions measured

Test Point No.	**I_{SS3}**	**DR**	**Test Conditions**
1	0.38	1.12	Internal and film cooling
2	0.62	1.13	Internal and film cooling
3	1.09	1.14	Internal and film cooling
4	2.46	1.16	Internal and film cooling
5	5.01	1.17	Internal and film cooling
6	0.38	1.12	Internal and film cooling, 1st repeat
7	0.38	1.12	"Internal Cooling Only"
8	1.11	1.14	"Internal Cooling Only"
9	2.44	1.15	"Internal Cooling Only"
10	4.80	1.17	"Internal Cooling Only"
11	0.64	1.13	"Internal Cooling Only"
12	1.69	1.15	Internal and film cooling
13	2.98	1.16	Internal and film cooling
14	0.38	1.12	Internal and film cooling, 2nd repeat
15	0.40	1.25	Internal and film cooling, High DR

2.4.3 Reduction of Experimental Data

While most of the experimental data reduction took place following completion of the experiment, a small amount of processing was done by the LabView code responsible for monitoring the experiment. The pressure transducers output a voltage that corresponded to the pressures - this voltage was measured by the DAQ system and was converted to a pressure using a simple linear calibration curve specific to each pressure transducer. The mainstream flow velocity was found from the dynamic pressure measured by the Pitot-static probe, calculated by

$$U_{\infty} = \sqrt{\frac{2P_{dyn}}{\rho_{\infty}}} \tag{2.2}$$

where $P_{dyn} = P_{stag} - P_{\infty}$ is the difference between stagnation and static pressure measured at the two ports of the Pitot-static probe, and ρ_{∞} is the density of the mainstream flow, found from the mainstream temperature and static pressure.

The pressure drop across each orifice flow meter, ΔP_o, was used to find the mass flow rate of coolant entering the vane model as

$$\dot{m} = \rho_o A_d \frac{C_d}{\sqrt{1-\beta^4}} \sqrt{\frac{2\Delta P_o}{\rho_o}} \tag{2.3}$$

where $\dot{m}$ is the total coolant mass flow rate through the orifice, A_d is the orifice discharge area, C_d is the orifice discharge coefficient, and β is the diameter ratio $D_{orifice}/D_{pipe}$.

The discharge coefficient, C_d, was a function of Re based on the orifice diameter and velocity through each orifice flow meter. These values came from a calibration using a laminar flow element which was performed by fellow lab mate Tom Dyson in a separate experiment, which also accounted for gas temperature, static pressure upstream of the orifice, and orifice geometry. More information on the use of orifice flow meters in general is given by Goldstein (1996).

Using the coolant mass flow rate calculated from the orifice flow meters, the average velocity of the coolant leaving the film cooling jets was found by assuming a uniform coolant distribution across the row of jets and using the density of the coolant, $\rho_{c,hole}$, and total jet area for the row of film cooling holes, A_{hole}:

$$U_c = \frac{\dot{m}}{A_{hole}\rho_{c,hole}}. \tag{2.4}$$

Testing the assumption of uniformly distributed coolant along the row of film cooling holes was done during a subsequent experiment performed by fellow lab mate Tom Dyson, using the IR camera to look at the surface temperature just downstream of the row of jets on a geometrically identical model made of low conductivity polyurethane foam. This same test had been attempted using the matched-Bi vane at the beginning of the present study, but this was unsuccessful since temperature gradients in the coolant flowing through the interior passages of the vane model were externally visible due to conduction through the part wall, and this made resolving jet-to-jet differences impossible.

Ultimately, the film cooling jet velocity was normalized into the momentum flux ratio, as defined in Eq. 1.6. The freestream velocity at the position of the row of film cooling holes was determined from the surface pressure measurements referred to in Section 2.4.1, and the freestream temperature was measured using a pair of E-type thermocouples located just upstream of the vane model.

Processing the surface temperature data measured using the IR camera was a multi-step process primarily done using Matlab and Excel. After retrieving the image files form the camera, FLIR software was used to extract the temperature data from the proprietary image format and export the temperatures to a Matlab matrix where the value of each cell was the temperature of the corresponding pixel in the image. Because the surface of the vane was curved and viewed at an angle by the camera, a Matlab script developed previously at $TTCRL$ was used to remove the effects of curvature and perspective from the images by mapping the location of each pixel to linear coordinates in the span-wise and stream-wise directions along the vane surface. For this, the pixel coordinates of silver “tick” marks on the vane surface were found in the image files using the FLIR software, and correlated with their physical position on the vane surface. In addition to transforming the image pixel coordinates to physical coordinates, the Matlab code also applied the IR calibration discussed in Section 2.3.3, calculated laterally-averaged temperatures at each span-wise pixel location and also output the calibrated temperatures and physical coordinates to a set of spreadsheets for importation into Excel.

Laterally averaged surface temperatures were loaded into Excel and were then normalized according to the definition of overall effectiveness shown in Equation 1.8. In order to confirm that steady state conditions had indeed been met, the last 10 minutes of data collected for each test condition were compared to each other, and had to vary by less than $\phi = 0.01$ in order to declare that conditions were in fact steady.

Internal gas and surface temperatures were measured using thermocouples, and NIST-standard correlations were used by LabView to convert the voltage measured by the DAQ into temperatures for monitoring during the experiment. While the thermocouples were not individually calibrated as part of the current study, a thermocouple calibration experiment was performed by fellow lab mate Todd Davidson as part of a separate study, which showed bias errors in the temperatures reduced from the standard correlations as will be discussed in the next section. The internal gas and surface temperatures were both normalized as a fraction of the mainstream to coolant temperature difference:

$$\theta = \frac{T_\infty - T}{T_\infty - T_{c,imp.jet}}, \tag{2.5}$$

where the reference temperature for the coolant, $T_{c,imp.jet}$, is defined as the average temperature measured at the center of two different impinging jet temperatures, one at a low span-wise position, and the other at a higher span-wise position. This is consistent with the normalization of ϕ, with the simple difference that while ϕ is reserved for external surface temperatures only (by the definition of overall cooling effectiveness), θ can refer to any normalized temperature throughout the system.

2.5 Estimation of Measurement Uncertainty

Uncertainty in I_{SS3} was estimated using the sequential perturbation method given by Moffat (1988), whereby uncertainties in each of the measurands used to calculate I_{SS3} were estimated and propagated through the data reduction sequence in order to find an estimate of the uncertainty in the final computed value. This method uses a root-sum-squares approach to add the contributions to the final uncertainty due to each of the individual measureands in a very similar manner as the widely used Kline-McClintock formula for error propagation, but eliminates the need to calculate partial derivatives in order to find the sensitivities to each elemental uncertainty. First, a single equation was entered into Excel to calculate I_{SS3} from the individual experimental measurements, by taking the definition of the momentum flux ratio shown in Equation 1.6, and substituting into it Equations 2.4, 2.3, and 2.2. Densities were determined by substituting in the ideal gas law, $\rho = P/(R_{air}T)$, where the static pressure and temperature, P and T, were taken at the location where the density was needed. This expression was then evaluated using each of the individual measurements "as measured" to find the value of I_{SS3} reported at each test condition and then re-evaluated while perturbing the value of each measureand by it's uncertainty one-by-one. The differences between the "as measured" and perturbed values for each measureand were combined in a root-sum-squares fashion to arrive at a total uncertainty in I_{SS3}.

The most critical (and perhaps the most difficult) part of performing such an uncertainty analysis is determining what the appropriate elemental uncertainties are which contribute to the uncertainty in the final measurement. For the current study, the each of the variables appearing in Equations 1.6, 2.4, 2.3, and 2.2 had an uncertainty associated with them. The precision uncertainty in the orifice flow meter pressure drop ΔP_o was estimated from a root-summed-squares combination of two separate random components. The first component of the uncertainty was due to zero bias drift in the pressure transducer over the course of the experiment, which was ascertained as follows: after collecting data at each test condition but before adjusting the tunnel to the next condition, the valve controlling the coolant flow was periodically shut to measure the pressure transducer output in the absence of a pressure difference, and it was recorded and re-zeroed in LabView before opening the valve again. In general, the zero-bias drifted both up and down over the course of the experiment and and didn't depend on the value of the pressure measured, making it a random error (rather than a systematic one). The uncertainty in ΔP_o resulting from this bias drift was estimated from the set of values recorded during the experiment to be $0.007 in.H_2O$. There was also a random fluctuating component the pressure measurement seen on a shorter time scale than the zero bias drift, which was estimated by measuring the pressure drop multiple times during a relatively short time period while holding the wind tunnel conditions constant, and was found to be 1.1% of the pressure reading with 95% confidence, ranging from $0.0029 inH_2O$ to $0.042 inH_2O$ over the range of flow rates tested.

Because a calibration curve was used to convert each of the pressure transducer voltages to a pressure (as shown in Figure 2.13), each pressure measurement is subject to a bias uncertainty which can be attributed to uncertainty in the curve fit coefficients. Uncertainty in these coefficients was found to be $\delta \Delta P_{o,bias} = \pm 0.0038 in.H_2O$ by the method of sequential perturbation, where each calibration data point was perturbed by the individual measurement uncertainty, one at a time, to arrive at a population of curve fit coefficients upon which statistics could be performed. Uncertainty in the static pressure measurements just upstream of the orifice flow meter was also $\delta P_o = \pm 0.19 in.H_2O$, based on a similar random scatter and transducer zero bias drift. The dynamic pressure of the pitot static probe used to measure freestream velocity was $\delta P_{dyn} = \pm 0.0004 in.H_2O$, based on the calibration curve for the pressure transducer previously calibrated by Albert as part of his study.

The atmospheric pressure in the lab was taken from the most recent readings from the nearby Camp Mabry weather station, with the uncertainty taken as one-half of the reported resolution, or $\delta P_\infty = 20Pa$. The physical dimensions of the orifice flow meter orifice plates and film cooling holes were measured using calipers with a resolution of $0.001in.$, so the uncertainty for both diameters was taken to be one-half of this resolution, $\delta d = 0.0005in.$.

A thermocouple calibration experiment was performed by fellow graduate student Todd Davidson shortly after the completion of the current study. He found that the temperatures read from a thermometer disagreed with the temperatures reported by the thermocouples by between $1K$ and $2.4K$ depending on the temperature, so the bias uncertainty of the thermocouples was taken as $\delta T_{bias} = \pm 1K$ to $2.4K$. Precision uncertainty for the temperature measurements was estimated by looking at the thermocouple temperatures over the "steady state" data collection period to see how much temperatures varies while test conditions were steady, and was typically about $\delta T_p = \pm 0.5K$.

The resulting uncertainty in I_{SS3} is shown for film cooled test cases from I_{SS3}=0.38 to 5.01 in Table 2.3.

The largest elemental uncertainty contributing to δI_{SS3} depended on the coolant flow rate. At low values of I_{SS3} where the flow rate through the coolant supply system was low, the uncertainty in I_{SS3} was dominated by the bias drift in the pressure transducer output used to measure the drop across the coolant orifice flow meter. Because the pressure drop across the orifice flow meter became large relative to the bias

Table 2.3: Uncertainty in momentum flux ratio

I_{SS3}	δI_{SS3}	δI_{SS3} [%]
0.38	0.014	3.7%
0.62	0.016	2.6%
1.09	0.023	2.1%
2.45	0.047	1.9%
5.01	0.095	1.9%

error at high flow rates, the uncertainty contribution due to the pressure transducer decreased with increasing I_{SS3}, and at the highest values of I_{SS3} the uncertainty was dominated by contributions from the coolant and mainstream temperature and the physical dimension of the flow meter orifice and film cooling holes. Although the absolute uncertainty increased along with I_{SS3}, the relative uncertainty was the greatest at $\delta I_{SS3} = 3.7\%$ at the lowest value of $I_{SS3} = 0.38$, decreasing to $\delta I_{SS3} = 1.5\%$ at the highest value of $I_{SS3} = 5.01$.

The precision uncertainty in the measurement of ϕ was estimated to be $\delta\phi_{prec} = \pm 0.02$ by Dees et al. (2011b), who repeated an experiment with a similar matched-Bi vane model in the same facility at $TTCRL$ a number of times and measured the overall effectiveness at the same I values each time in order to perform a statistical analysis. Because the current study was performed in the same facility and in a similar fashion, it may be reasoned that the uncertainty in the measurement of ϕ for the current study will be approximately the same as Dees' study. While Dees did not report any bias uncertainty limits, the known thermocouple bias uncertainties were used to estimate the bias uncertainty for the current study. As already mentioned, the bias uncertainties in the coolant and mainstream temperatures revealed by the recent calibration experiment were estimated to be $\delta T_{bias} = \pm 1K$ to $2.4K$, and the bias uncertainty in the surface temperature was estimated to be $\delta T_{surface} = \pm 0.75K$

based on the fact that out of the three surface thermocouples used for IR camera calibration, there was a noticable bias difference between the three thermocouple of about $1.5K$, so the bias uncertainty was taken to be half of this. These individual biases were all propagated into an estimated bias uncertainty of $\delta\phi_{bias} = \pm 0.023$. A root-sum-squares combination of the bias and precision uncertainty showed the total uncertainty to be $\delta\phi = \pm 0.03$. It is important to note the differences between the bias and precision components of the uncertainty here, since only the precision component is relevant when determining if any trends within the data are statistically significant while the bias uncertainty will be constant across the entire dataset, and the total uncertainty gives the limits within which the true value of the data is expected to be.

The uncertainty in measured values of normalized internal temperatures, θ_g and $\theta_{w,i}$, were also found by the same sequential perturbation method just described, where the data reduction equation used was Equation 2.5, and each of the measured temperatures were perturbed by their estimated uncertainties. The total uncertainty in internal temperatures was $\delta\theta_g = \delta\theta_{w,i} = \pm 0.015$, which can be broken into a precision component of $\delta\theta_{prec} = \pm 0.014$ and a much smaller bias component of $\delta\theta_{bias} = \pm 0.001$. The precision uncertainty component was estimated by looking at the variation in temperatures over the period of "steady" data collection at each test condition, and were approximately $\delta T_{precision} = \pm 0.5K$. In addition, the sensitivity of $\theta_{w,i}$ to I_{SS3} was numerically approximated from the processed data in order to examine the contribution to $\delta\theta$ from δI_{SS3}, and this was determined to be an order of magnitude less than the contribution to $\delta\theta w, i$ from the uncertainty in the temperatures appearing directly in Equation 2.5.

In order to validate these estimates of measurement uncertainty, one test condition was measured at multiple times throughout the primary experiment to assess the in-test repeatability of the measurements, and was also re-tested as part of a separate experiment on a different day to examine the test-to-test repeatability. If the above uncertainty estimates are accurate, each repeat point should be within the estimated uncertainty of one another. Comparisons between the initial test measurement and the two in-test repeat measurements are shown for the inner wall surface thermocouples in Figure 2.18, and for overall cooling effectiveness in Figure 2.19. Both figures also show error bars representing the precision uncertainty in ϕ and θ.

It is seen that the variation in inner wall surface temperature between the three different measurement instances was $\theta_{w,i} = 0.015$ or less, depending on the specific thermocouple. The overall variation in overall effectiveness between the original test point and the two repeats was $\phi = 0.02$, which was also the precision uncertainty in ϕ quoted by Dees et al. (2011b). The variation in repeated measurements for the current study would ideally be less than this. However, if an experiment were to be repeated enough times some measurements are statistically expected to fall near the limits of the experimental precision uncertainty, so these results should still be considered acceptable. The difference between the first and second and second and third data points are within the expected measurement uncertainty, and the spread is still small enough to be able to clearly distinguish trends in the results to be presented in the following chapter.

In addition to the in-test repeatability assessments, test-to-test repeatability was examined by taking measurements at the same test conditions during two different experiments which were performed nearly one month apart. Values of $\theta_{w,i}$ as a function of I_{SS3} are compared for two of the inner wall surface thermocouples in Figures 2.20 and 2.21. Error bars showing the estimated precision uncertainty are also shown, and it was seen that the two tests agreed well within the measurement

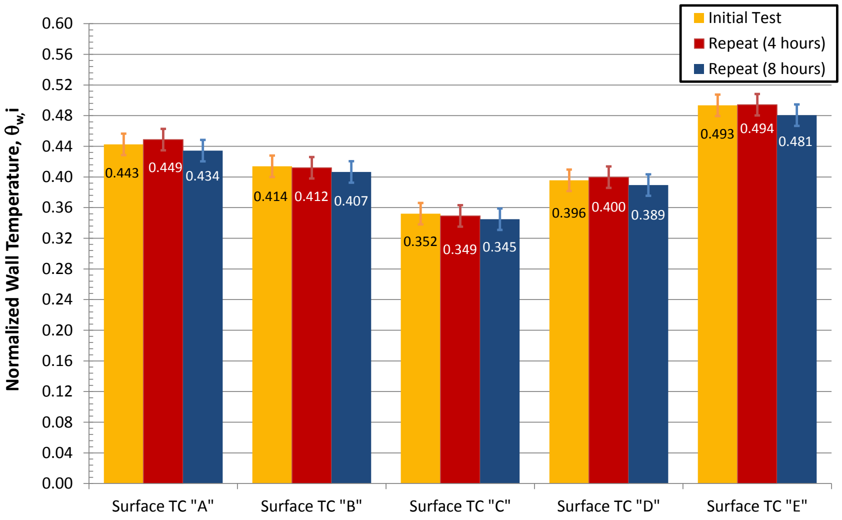

Figure 2.18: In-Test repeatability of normalized inner wall surface temperatures, $DR_{SS3} = 1.12$, $I_{SS3} = 0.38$

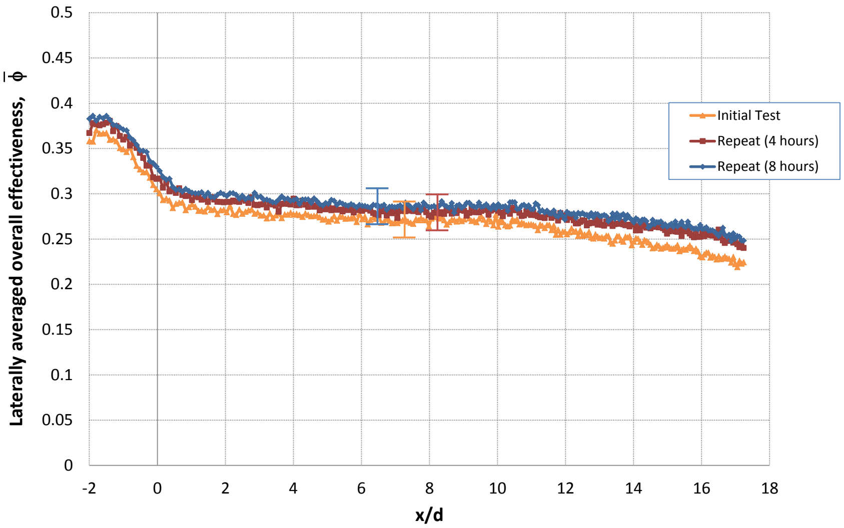

Figure 2.19: In-Test repeatability of overall effectiveness, $DR_{SS3} = 1.12$, $I_{SS3} = 0.38$

uncertainty of one another.

Test-to-test repeatability comparisons for $\overline{\phi}$ are shown in Figure 2.22 for two of the lower momentum flux ratios tested, and in Figure 2.23 for the highest mo-

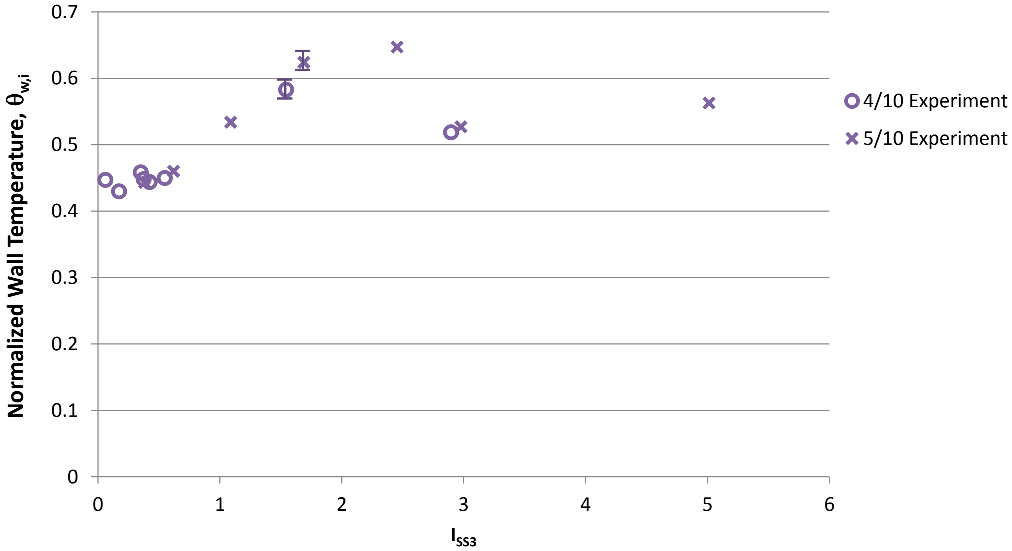

Figure 2.20: Test-to-test repeatability of internal wall surface thermocouple "A", nominal $DR_{SS3} = 1.14$

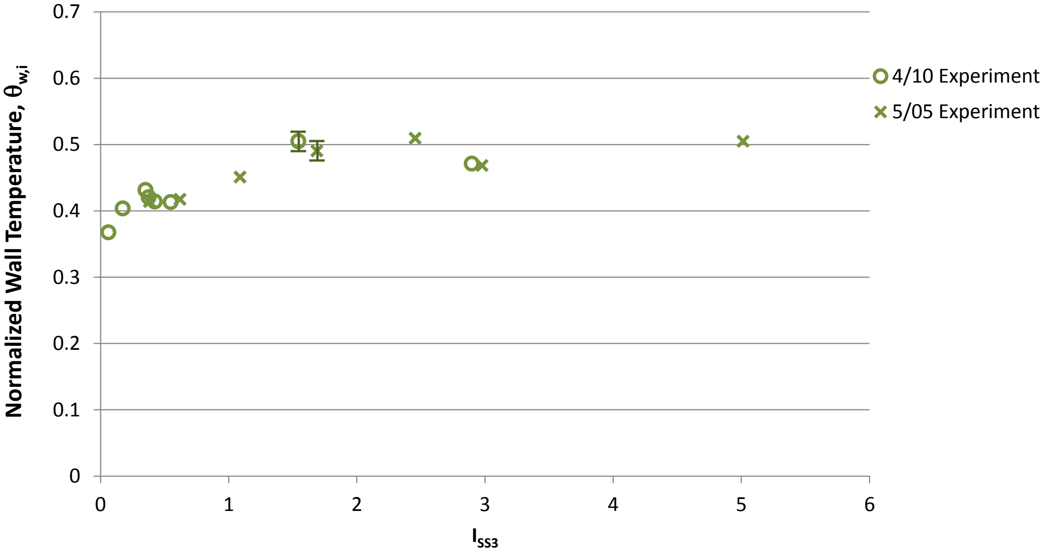

Figure 2.21: Test-to-test repeatability of internal wall surface thermocouple "B", nominal $DR_{SS3} = 1.14$

mentum flux ratio repeated between the two experiments. As was the case with the in-test repeatability of $\overline{\phi}$ and the test-to-test repeatability of $\theta_{w,i}$ just shown, the measured values of $\overline{\phi}$ agreed with one another well within the range of the measurement uncertainty, verifying the analytical uncertainty estimates.

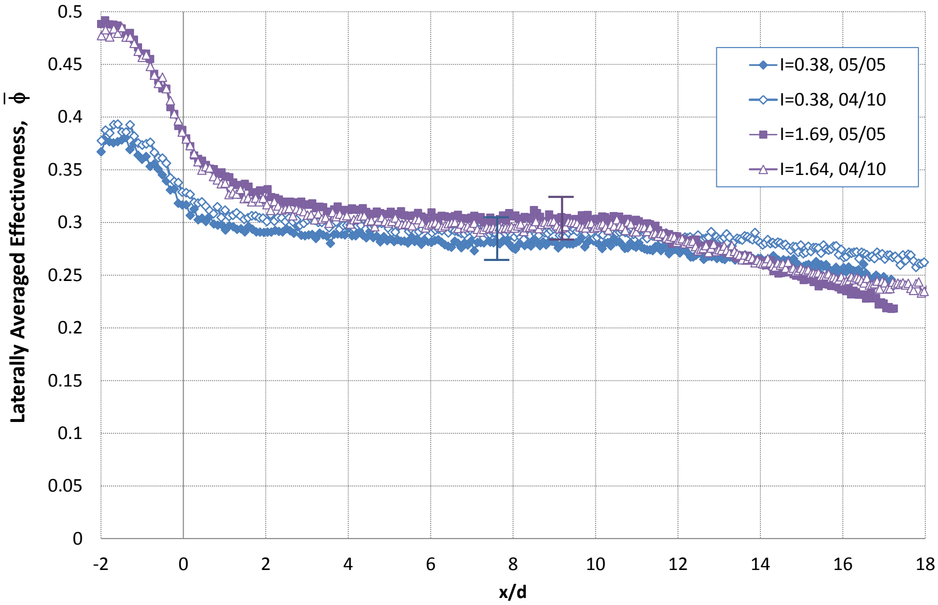

Figure 2.22: Test-to-test repeatability of $\overline{\phi}$, film cooling active, nominal $DR_{SS3} = 1.14$

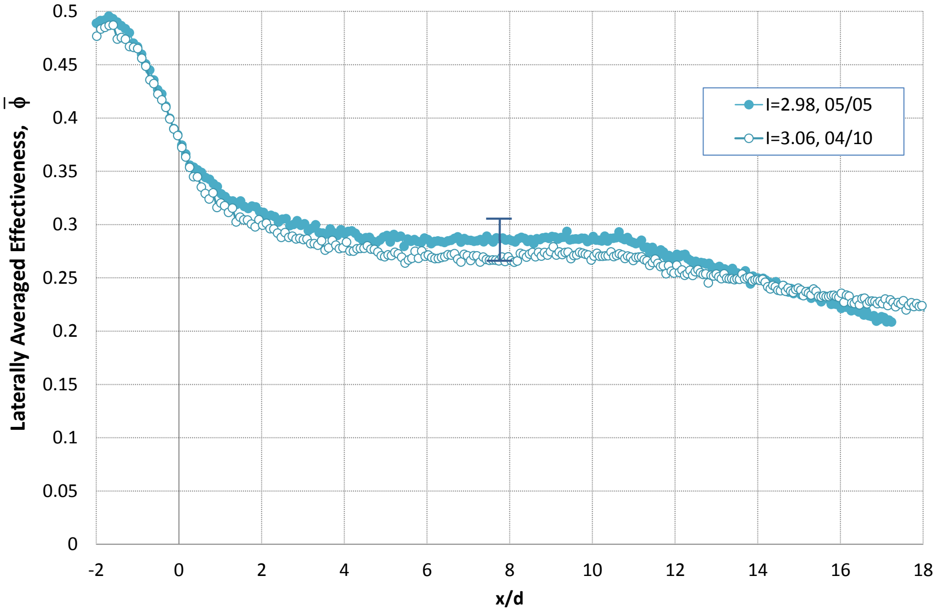

Figure 2.23: Test-to-test repeatability of $\overline{\phi}$, film cooling active, nominal $DR_{SS3} = 1.14$

Chapter 3

Results and Discussion

As mentioned previously, the objective of this study was to determine the overall effectiveness and internal temperatures for a gas turbine vane model cooled by both internal impingement and external film cooling. Measurements of internal coolant temperatures, internal wall surface temperatures, and external surface temperatures were made for scenarios both with film cooling and with two cooling holes taped over to simulate a case of internal impingement cooling alone. Results will first be presented for the simulated "internal cooling only" configuration, and then for the case with both impingement and film cooling, in order to demonstrate the effect of film cooling when impingement is present.

3.1 Internal Cooling Only

In this section, experimental measurements are presented and discussed for the set of test conditions for which the middle two film cooling holes were blocked off so that no film cooling was present over the inner-most hole pitch to simulate "internal cooling only". First, the effect of taping over the middle two holes on the overall effectiveness just downstream of the adjacent film cooling holes was examined in an attempt to validate the assumption that taping over the middle two holes had negligible impact on the internal impingement cooling performance. Normalized inner wall surface temperatures for a range of coolant mass flow rates will be presented, as well as external surface temperatures normalized as overall effectiveness. The normalized external surface temperatures were used were to back-calculate the laterally averaged convection heat transfer coefficient for impingement on the inner wall surface, and this will be compared with multiple empirical correlations.

3.1.1 Validation of Assumptions

In order to simulate “internal cooling only”, two film cooling holes in the middle of the field of view were taped over while the other holes remained open, preventing any coolant from being ejected over this center-most hole pitch while still allowing coolant to flow through the internal cooling circuit. Only the middle two holes were blocked because all of the coolant which enters the vane model must be ejected as film coolant, so blocking all of the holes to achieve a true non-film-cooled configuration would also eliminate the internal cooling. Blocking more than two holes would have increased the chances of seriously altering the internal coolant velocity field, which would make comparing the data to the film cooled cases questionable. In blocking off the two middle holes to simulate the case without film cooling, it is assumed that blocking off the two innermost film cooling holes has negligible effect on the behavior of the internal impingement cooling. To see how well this assumption holds, two contour plots which together show the effect of taping over the middle two holes while holding the coolant flow rate nominally the same are given in Figures 3.1a and 3.1b. The first figure shows the normalized external surface temperatures with the middle two jets active, while the second one shows the surface temperatures with the middle two holes blocked. It is seen by comparison of these two figures that taping over the middle holes not only prevented the ejection of film coolant over the innermost jet pitch as intended, but it also changed the normalized surface temperatures downstream of the outer two jets, reducing the overall effectiveness downstream of the outermost holes.

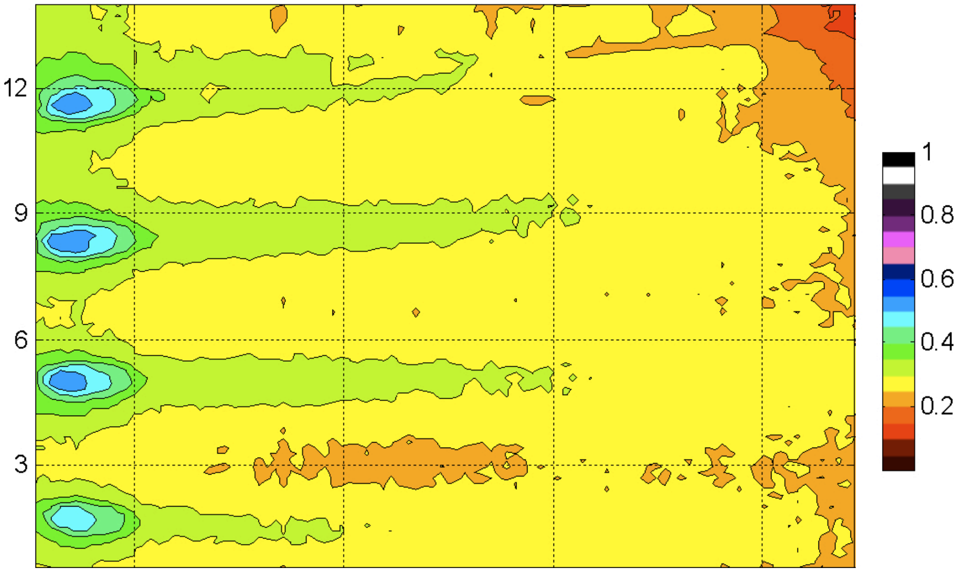

(a) Normalized surface temperature with holes un-taped, $I_{SS3} = 0.38$, $DR_{SS3} = 1.12$

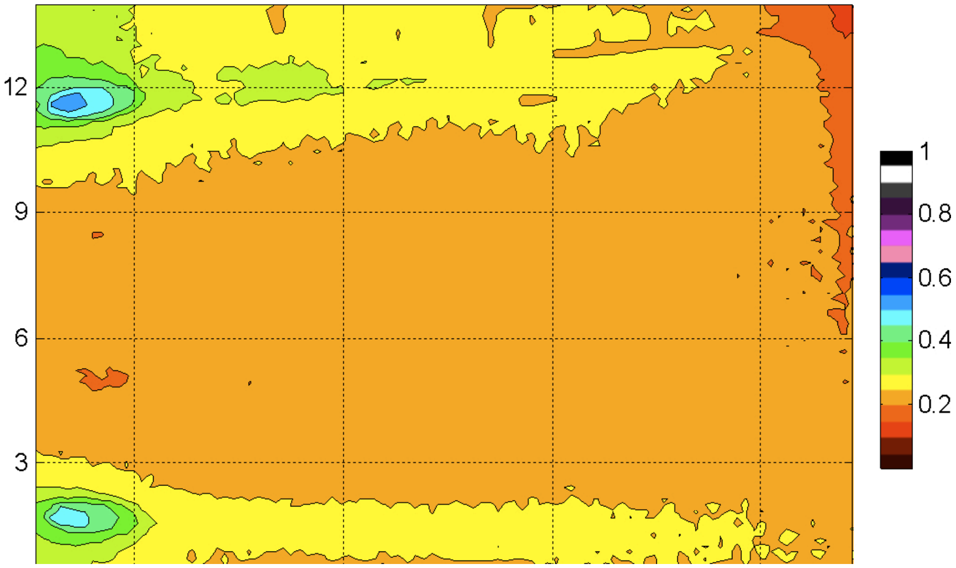

(b) Normalized surface temperature with holes taped, $I_{SS3} = 0.36$, $DR_{SS3} = 1.12$

Figure 3.1: Effect of taping over the middle two film cooling holes under the same nominal flow conditions

There are multiple possibilities for this change in performance. Taping over the middle two holes eliminates film cooling downstream of the innermost hole pitch, allowing the hot mainstream gas to directly contact the outer vane wall, which has the effect of reducing the overall effectiveness over this region relative to the adjacent regions which are film cooled by the un-taped jets. Because the vane model is conducting in nature, heat will be conducted laterally from the warm inner region towards the colder outer regions, which has the effect of heating up the vane wall in the film cooled region. The second possibility is that taping over the middle two holes did have some impact on the internal coolant distribution, potentially decreasing the amount of coolant which impinged upon on the inner wall surface and flowed through the outer two jets. These two scenarios are not mutually exclusive and it is possible that both lateral conduction in the part wall as well as a change in the inner coolant flow field are contributing to the decrease in overall effectiveness which occurs downstream of the outer two film cooling holes.

Although it was seen that taping over the middle two holes did alter the external surface temperature of the adjacent, un-taped holes, the change was relatively small. Because the cooling configuration with a single row of holes was only an intermediate configuration on the way to developing a fully cooled vane model with many more rows of holes (subsequently tested and reported on by Dyson et al. (2013)), the internal flow and internal impingement distribution which occurred with one row of holes was not representative of that which would occur for a fully cooled configuration. For the fully cooled configuration, much more coolant would flow through the other film cooling holes (over seven times as much) before being ejected as film coolant, and taping over two holes out of a single row would have a much smaller effect, since a smaller fraction of the total jet area would be blocked in this process. This would be expected give much more realistic results when the same method of blocking film cooling holes was employed to assess the amount of internal cooling which occurs with the vane in the fully-cooled configuration.

3.1.2 Internal Gas Temperatures with Middle Two Holes Blocked

As mentioned in Chapter 2, the vane model was instrumented with a number of thermocouples which were used to measure the temperature of the coolant as it travelled through the model, proceeding from the coolant inlet at the base of the model, through the internal plenum, through the impingement jet holes and impingement cavity (the region between the impingement plate and the inner surface of the vane wall), and finally through the film cooling holes. These thermocouples were installed at two different span-wise locations as shown in Figure 2.12, which were located roughly one-half of a hole pitch above and below the outer two holes being imaged by the IR camera. Therefore, the gas temperature measurements made by these thermocouples cannot be viewed as being for a case of simulated "internal cooling only" since they were most likely affected by the presence of the film cooling holes nearby, and these thermocouple measurements should be simply viewed as the gas temperatures at various positions inside the vane for the operating conditions where the middle two holes were blocked. Despite this, the author feels that before examining the effect that active cooling scenarios had on surface temperatures, it is helpful to know the temperature of the coolant as it flowed through the vane model and how this temperature varied with position and changes in coolant flow parameters.

Because the purpose of taking measurements with two holes taped over to simulate "internal cooling only" was to generate data which can be compared to the film cooled case, the total coolant mass flow rates through the model for the non-film-cooled cases were matched to those of the film cooled cases which will be presented later, which were based on the momentum flux ratios tested for the film cooled cases. To make comparing results easy between the non- and film-cooled cases, the coolant flow rates in this section are presented in terms of an equivalent momentum flux ratio, $I_{SS3,eq}$, which would be achieved if all of the film cooling holes were active, so that the total coolant mass flow rates are equal when matching $I_{SS3,eq}$ for the non-film-cooled cases and I_{SS3} for the film cooled cases.

Normalized coolant temperatures, θ_g (previously defined in Eq. 2.5), measured at different locations along the gas flow path at the lower of the two span-wise instrumentation locations are shown in Figure 3.2 for $DR_{SS3} = 1.12$ and $I_{SS3,eq} = 0.38$. These temperatures have been normalized between the mainstream temperature T_∞ and $T_{c,imp.jet}$, as previously shown in Equation 2.5, where it should be emphasized that $T_{c,imp.jet}$ is the average of the two different span-wise impinging jet temperatures. The positions along the flow path include the middle of the coolant plenum upstream of the impingement plate, the center of an impinging jet, a ribbon thermocouple located on the downstream surface of the impingement plate, a thermocouple in the cavity between the impingement plate and the inner surface of the vane wall, and two thermocouples at the inlet to one of the film cooling holes which was not blocked to simulate the absence of film cooling. A more detailed description of each thermocouple location was given in Chapter 2, Figure 2.11.

It is clearly seen in Fig. 3.2 that the coolant warmed up as it traveled from the flow development section upstream of the vane model through to the film cooling hole inlet. An explanation for this warming trend is simple when the vane is viewed as a gas-to-gas heat exchanger, transferring energy from the hot mainstream flow to the coolant inside the model: as heat was transferred by convection and conduction through the vane wall, it was ultimately transferred to the coolant flowing through the vane.. As the coolant flowed from the vane inlet to the plenum and outwards toward the film cooling holes, it continually gained thermal energy, which resulted in

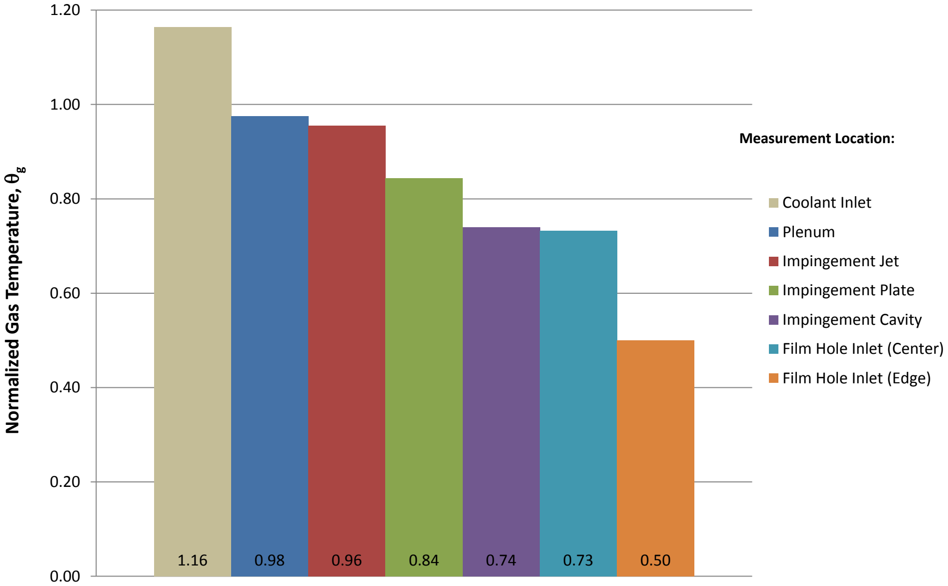

Figure 3.2: Internal coolant temperatures at various positions along the gas flow path, lower span-wise location, $DR = 1.12$, $I_{SS3,eq} = 0.38$, middle two holes blocked

an increase in temperature.

Comparing normalized temperatures between the coolant inlet and the plenum inside the impingement plate, there was a drop in θ_g of about 0.2, indicating a significant amount of coolant heating between the inlet to the model and the plenum TC location, although it was noticed after the test that the position of this plenum thermocouple had been accidentally bent by about 3 cm during routing of the thermocouple wires through instrumentation ports in the top of the model. The plenum thermocouple was originally placed in the center of the plenum about 13 cm from the dividing wall, but was inadvertently moved to a position approximately 10 cm from the wall which divides the front and rear coolant plena. This error in thermocouple placement is most likely the reason for the drop in θ_g observed from the inlet to the plenum. The coolant inside the plenum would be expected to be the coldest in the center of the plenum, so positioning the thermocouple closer to the edge of the plenum may have resulted in an erroneously warm measurement. In subsequent experiments performed by lab-mate Tom Dyson using the same vane model but with corrected plenum thermocouple placement, the temperature rise between the inlet at the base of the model and the middle of the plenum was negligible, which would confirm the misplacement of the thermocouple in the current study as the source of the drop of θ_g seen here.

At the lower span-wise location, the temperature of coolant flowing through the impinging jet hole was close to that measured by the internal plenum thermocouple, which would be expected if the coolant was flowing from the location in the plenum where the temperature was measured to the impinging jet hole without passing over any warm surfaces which could heat the coolant. A significant decrease in normalized temperature was measured from the impinging jet hole to the gas in the middle of the impingement cavity, with the temperature of the impingement plate between the two gas temperatures. After passing through the impingement plate and forming impinging jets, the coolant came into close proximity with the inner wall surface and warmed up as a result of the convective heat transfer at this surface. Because of the nature of the impinging jets and high levels of turbulent mixing which would be expected to exist in the impingement cavity, this warmed gas mixed with the rest of the gas in the impingement cavity and also heated the downstream surface of the impingement plate. Finally the coolant from the impingement cavity was exhausted through a pair of the unblocked film cooling holes. The center of the film cooling hole was near the same temperature as the gas in the center of the impingement cavity, while the gas near the edge of the film cooling hole was even warmer, due to it's proximity to the wall surface and the thermal boundary layer which existed above the inner wall surface of the vane.

The cooling configuration of a single row of holes which was tested was only a small portion of a larger project which aimed to study a fully-cooled vane model. One row of holes was chosen for simplicity, to provide an opportunity to debug the test apparatus while other rows of holes were being machined into vane hatches which would be subsequently tested. Because all of the coolant entering the vane had to leave through a single row of film cooling holes, the total mass flow rate through the interior passages of the vane for this simplified cooling configuration was much lower than it would be flow for a fully cooled configuration. The thermal capacity of the coolant was less than would exist for a more realistic cooling configuration, and the amount of heating experienced by the coolant was greater as well. For a fully cooled configuration where many more rows of film cooling holes are added to the current vane, the coolant mass flow rate would be over twice as much as for the single row of holes, so there would be less coolant heating between the inlet to the model and the exit of the film cooling holes on account of the higher mass flow rate.

The internal coolant temperature measurements just discussed for the "lower" span-wise location were also repeated at an "upper" span-wise location, farther downstream from the flow inlet. Figure 3.3 presents a direct comparison of these upper position thermocouples with the lower span-wise measurements for the same flow conditions of $DR_{SS3} = 1.12$ and $I_{SS3,eq} = 0.38$. It should be noted that a problem during the experiment caused a thermocouple located in the inner coolant plenum at the "upper" span-wise location to quit functioning, so no valid measurement was recorded for comparison to the lower position in the inner plenum. It is seen in Figure 3.3 that θ_g was consistently higher, meaning the gas was consistently colder, at the upper span-wise location than it was at the lower span-wise location. This may be contrary to intuition - it was expected that the coolant was flowing upwards through the internal plenum (because the coolant inlet to the model was at the base of the

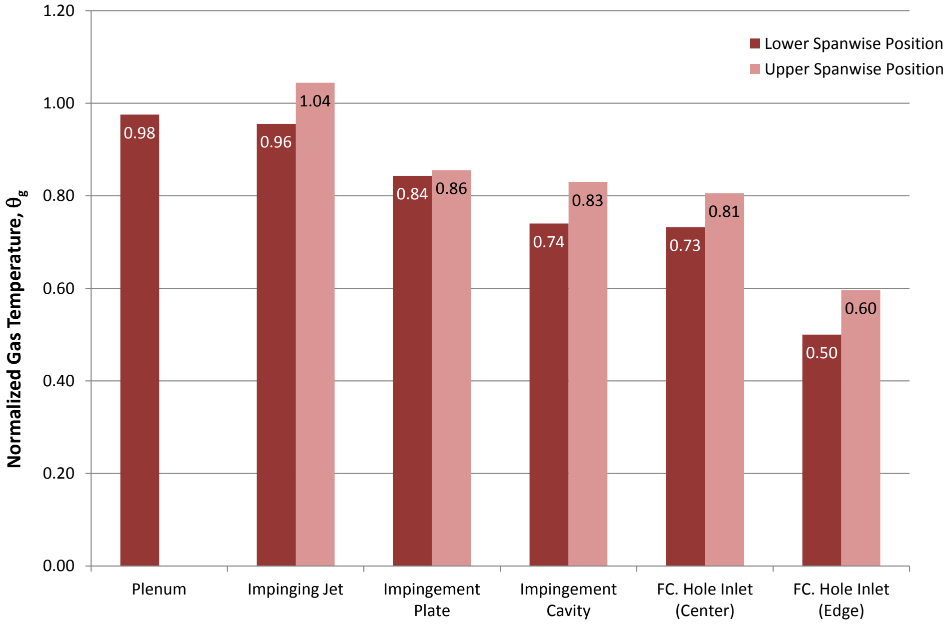

Figure 3.3: Comparison of internal coolant temperatures at two span-wise locations, $DR_{SS3} = 1.12$, $I_{SS3} = 0.38$, simulated "internal cooling only"

plenum), and because of heat transfer from the hot external mainstream flow though the wall of the vane and into the coolant, the coolant should have warmed up as it flowed through the model. This would result in higher θ_g at the lower span-wise location than at the upper location, which stands in contrast to the temperature distribution measured experimentally.

One possible explanation for the counter-intuitive span-wise gradient observed is if the geometry of the coolant inlet to the vane plenum caused a more complex coolant flow pattern inside the model than the simple upward flow which was expected. As described previously in Section 2.2.2.1, coolant doesn't enter the plenum uniformly, but is only supplied to about the front one-half of the plenum, while the trailing half of the plenum is blocked off at the base. This could have created a jetting effect where the incoming coolant flowed from the inlet up through the front portion of the plenum before striking the top plate of the vane model and turning back downwards through the rear part of the plenum. An illustration of this hypothetical flow pattern is shown in Figure 3.4.

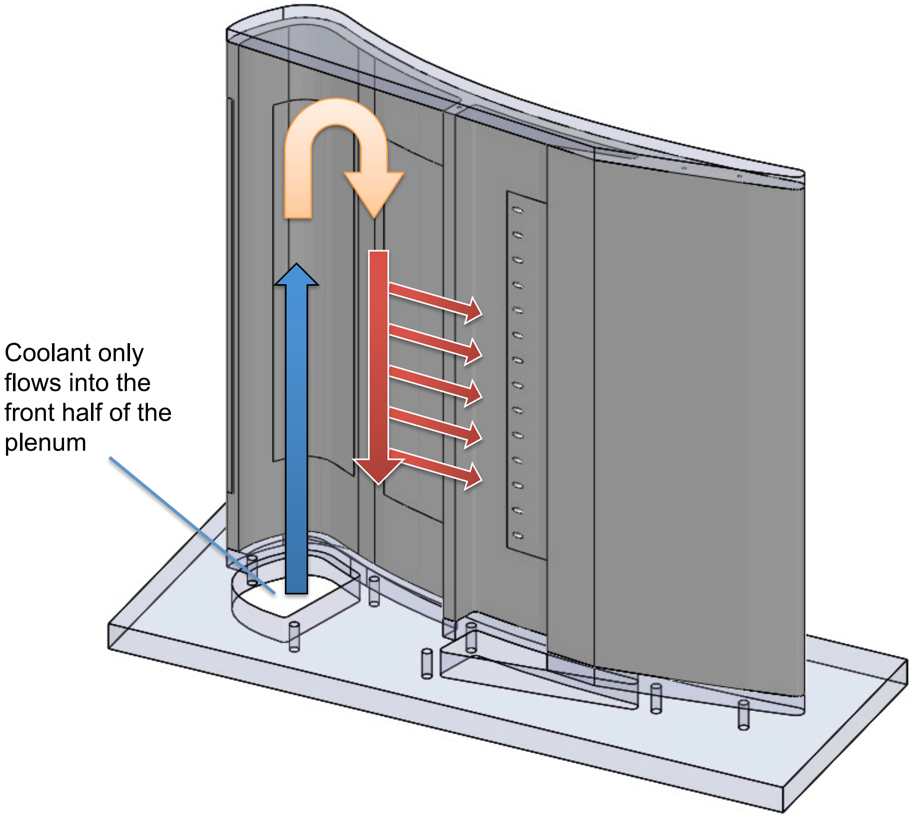

Figure 3.4: One hypothetical coolant flow path inside the plenum feeding the impinging jets which could cause the unusual span-wise temperature gradient observed

If instead of flowing from the bottom of the vane upwards, a portion of the coolant was flowing from the top of the vane downwards, passing first over the thermocouples at the upper span-wise location before passing over the thermocouples at the lower span-wise location, this would be consistent with the intuitive understanding of heat transfer since the coolant would be warming up along the direction of the flow.

The effect of varying the coolant flow rate on the internal coolant temperatures is seen in Figure 3.5, which presents the temperature of gas at the impinging jet orifice and at the center of the film cooling hole inlet for both span-wise locations as a function of $I_{SS3,eq}$, as well as the normalized temperature at the coolant inlet at the base of the vane model. Two important trends may be noticed here. With regard to the span-wise temperature gradient just discussed, the gradient persisted for all coolant flow rates tested at this density ratio; the gas at each of the upper thermocouple locations was consistently colder than the gas at the lower thermocouple locations over the entire range of $I_{SS3,eq}$. While Figure 3.5 only shows the impinging jet and hole inlet temperatures, this trend holds true for the other positions as well.

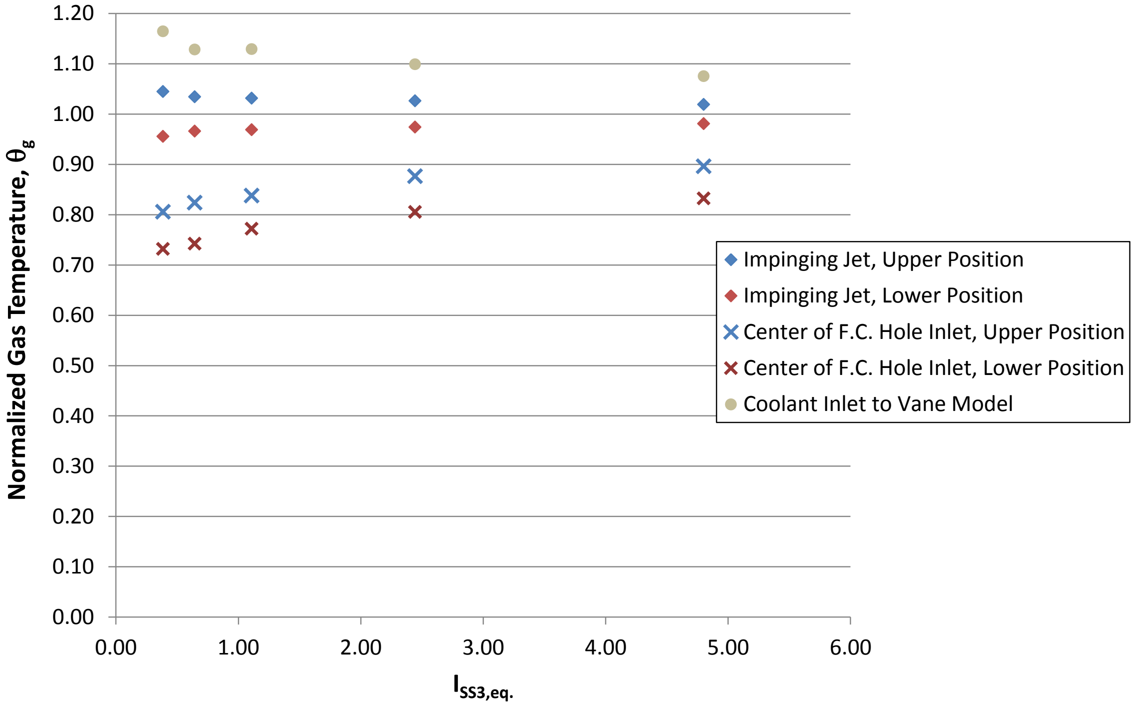

Figure 3.5: Variation of span-wise coolant temperatures with coolant flow rate, nominal $DR_{SS3} = 1.14$, simulated “internal cooling only”

As $I_{SS3,eq}$ was increased, θ_g at the center of the film cooling hole inlets increased as well, while θ_g for the coolant inlet at the base of the model continually decreased. Because θ_g is normalized relative to the average temperature of both measured impinging jet locations as shown in Equation 2.5, this signifies that the temperature rise of the coolant from the vane inlet to the impinging jets is decreasing as the flow rate is increased, as does the measured temperature rise from the impinging jets to the film cooling holes. From a heat transfer perspective, this is unsurprising: as the coolant flow rate was increased, the capacity of the coolant to store thermal energy also increased. If the specific heat of the fluid is taken as constant, the amount of heat transferred to the coolant can be easily related to the temperature change of the fluid from the inlet to the outlet by $q'' = \dot{m}C_p\left(T_{inlet} - T_{outlet}\right)$ (Incropera and DeWitt, 2002). The product $\dot{m}C_p$ is sometimes referred to as the “heat capacity rate” and is the proportionality factor between the amount of heat transferred to a fluid and the temperature rise experienced by the fluid. It’s easily seen that increasing the capacity flow rate will decrease the amount of temperature rise from the impingement hole to the coolant hole inlet experienced by the fluid for a given heat transfer rate, which is consistent with the results presented in Figure 3.5.

3.1.3 Internal Surface Temperatures with Simulated Internal Impingement Cooling Only

While gas turbine engine designers are ultimately concerned with reducing the external surface temperature of an actively cooled gas turbine engine component, examining the internal component surface temperatures can be useful to help draw conclusions regarding the behavior of the cooling system. As discussed in Chapter 2 Section 2.2.2.3, our vane model was instrumented with five ribbon type thermocouples on the inner wall surface of the hatch containing the film cooling holes for this purpose.

With the middle two film cooling holes taped over to simulate the case of internal cooling only, the rate of convection heat transfer on the inner wall surface resulting from the impinging jets is of great importance since convection on the inner wall was the only mechanism that kept the wall temperature below that of the hot mainstream gas. As the coolant flow rate was increased during the experiment, the strength of the impinging jets increased which in turn increased the internal heat transfer coefficient, h_i. This change in h_i had a direct impact on the inner wall surface temperature measured by the five ribbon thermocouples. Like θ_g, the internal wall surface temperatures have been normalized between T_∞ and $T_{imp.jet}$ according to Equation 2.5, and the effect of varying the coolant flow rate and therefore the jet strength on $\theta_{w,i}$ is shown in Figure 3.6.

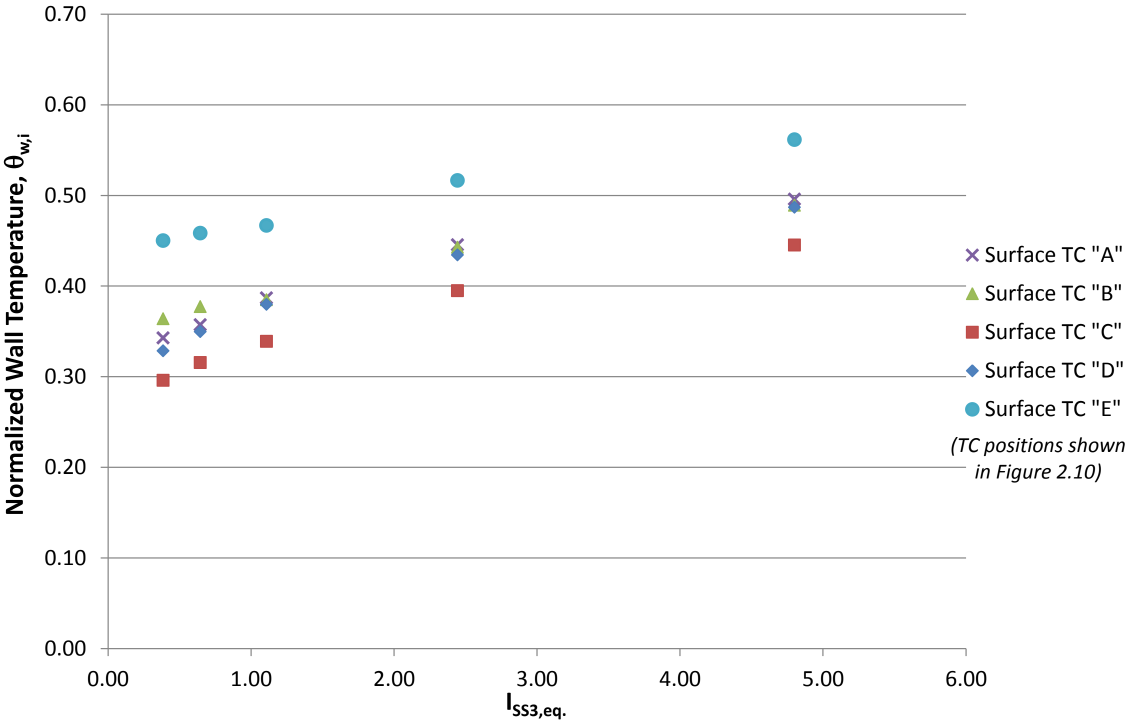

Figure 3.6: Variation of internal wall surface temperatures with coolant flow rate, nominal $DR_{SS3} = 1.14$, simulated "internal cooling only"

For each particular value of $I_{SS3,eq}$, there was an amount of variation between the five different thermocouples - this can be primarily attributed to the differences in position of the thermocouples. Thermocouples "A" and "E" were located very close to the film cooling holes which had been taped over as part of the "internal cooling only" simulation, although “A” was slightly closer to one of the untaped holes as seen in Figure 2.10. The warmest thermocouple at all values of $I_{SS3,eq}$ tested was thermocouple “C”, which was also the farthest downstream from the film cooling holes. Without film coolant, there is no reason to expect a large stream-wise temperature gradient over this relatively flat section of the airfoil, so the difference between thermocouple “C” and the others could be attributed to the exact position of the thermocouple relative to the location of the impinging jet striking the inner wall surface of the airfoil. Even though thermocouple “C” was positioned on the inner wall surface directly across the impingement cavity from an impinging jet hole as shown in Figure 2.10, the impinging jets were not expected to travel straight from the hole to the inner wall surface at this location (because of cross-flow through the impingement cavity since all of the coolant had to be exhausted through the unblocked film coolant holes). Thermocouples “A”, “B”, and “D” all measured very similar temperatures across the range of $I_{SS3,eq}$ tested, particularly at the highest three flow rates measured.

A 1-D series resistance model of the heat transfer through the vane wall can be used to verify that the behaviour of $\theta_{w,i}$ with $I_{SS3,eq}$ is physically reasonable. As $I_{SS3,eq}$ is increased, the impinging jets strengthen, which increases the internal heat transfer coefficient h_i. This will decrease the overall heat transfer resistance through the wall (since h_0 stays the same). The associated increase in q'' along with the decreased heat transfer resistance associated with the internal convection should result in the inner wall surface becoming much colder, or increasing $\theta_{w,i}$, and is consistent with the measurements shown in Figure 3.6. Estimation of the change in h_i with $I_{SS3,eq.}$ is discussed in the next section.

3.1.4 External Surface Temperatures with Simulated Internal Impingement Cooling Only

Because the hottest part of an actively cooled gas turbine vane is the external surface, overall effectiveness is one of the most useful figures of merit for evaluating cooling performance. Examining the overall effectiveness with the film cooling holes blocked to isolate the effect of internal impingement cooling is important in evaluating the contributions to overall effectiveness of each active cooling scheme individually; without knowing the contribution to overall effectiveness made by the impingement cooling alone, it would not be possible to determine how much the film cooling contributes to thermal performance for the scenario where film cooling and internal cooling are both active.

Laterally averaged overall effectiveness values are shown in Figure 3.7, which were calculated from the surface temperature according to Equation 1.8 and were laterally averaged over the middle pitch from centerline to centerline of the two holes which had been blocked. A knee is seen in each of the curves at a distance downstream of the hole of about $x/d = 11$ at which point $\overline{\phi_0}$ begins to drop off. This is because the coolant was fed through the vane in two different passages which are divided by a wall at this location as described in Chapter 2, and different internal cooling boundary conditions existed on either side of the dividing wall. Upstream of the dividing wall was the front coolant passage, which fed the film cooling holes and had impingement cooling as the internal surface boundary condition. Downstream of the dividing wall was the rear coolant passage, which had basic duct flow providing a nearly constant convective heat transfer coefficient on the inner wall surface. The bend in the overall effectiveness curves is much less noticeable for lower values of $I_{SS3,eq}$, which implies that the internal cooling conditions were closely matched, and the internal cooling in the front passage became much stronger than that in the rear passage as $I_{SS3,eq}$ was increased.

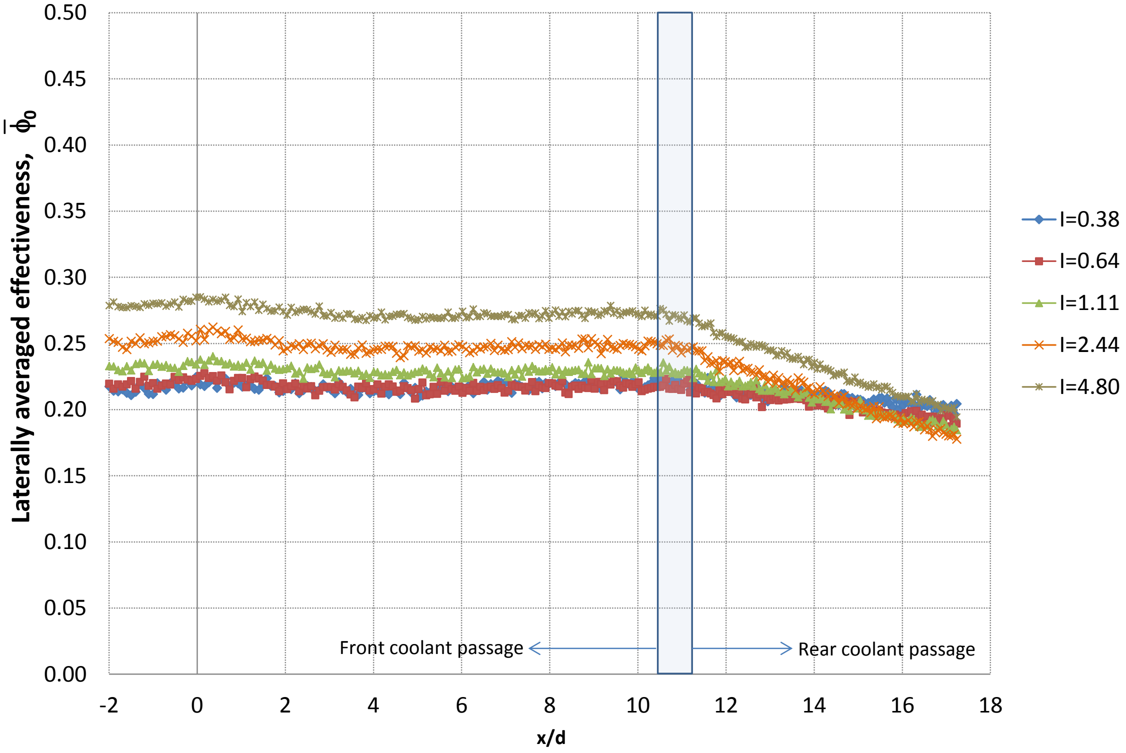

Figure 3.7: Laterally averaged overall effectiveness without film cooling, nominal $DR = 1.14$

An important trend is evident from Figure 3.7: with internal impingement cooling only, overall effectiveness is a monotonically increasing function of coolant flow rate. Over the range of conditions tested, there was no "optimal" value of $I_{SS3,eq}$ which resulted in a peak overall effectiveness, but rather $\overline{\phi_0}$ simply increased with $I_{SS3,eq}$. This highlights a distinction between impingement cooling and film cooling, since the latter is generally characterized by a peak effectiveness at a momentum flux ratio less than 1, above which performance decreases due to the tendency of the film cooling jets to detach from the surface and lose most of their cooling ability (Bogard and Thole, 2006).

It is seen here that values of $\overline{\phi_0}$ ranged from about 0.21 to 0.28 over the range of $I_{SS3} = 0.38$ to 4.80. During subsequent testing in the same test facility but with the vane model modified with 12 additional rows of film cooling holes in a "full coverage" configuration, Dyson et al. (2013) measured values ranging from about $\overline{\phi_0} = 0.40$ to 0.49 at significantly lower momentum flux ratios of $I_{SS3} = 0.40$ to 0.75. The reason that $\overline{\phi_0}$ was higher for the full coverage case at even lower I_{SS3} values was due to the greater mass flow rate of coolant passing through the impingement plate, which was more realistic and presumably more evenly distributed among the impinging jet array for the full coverage configuration. It should also be noted that for the fully cooled vane configuration, momentum flux ratios approximately above $I_{SS3} = 0.75$ were deemed unrealistic due to the total amount of coolant flow required through the model.

Once again, a 1-D heat transfer analysis is useful in determining whether the observed trend is reasonable. As $I_{SS3,eq}$ is increased and the impinging jets strengthen, q'' increases for the reasons previously discussed. In the absence of film cooling, h_0 and T_∞ remain the same, and so the temperature of the external surface should drop in accordance with the series resistance heat transfer model (as well as Newton's Law of Cooling, upon which the convection resistance is based). This causes an increase in overall effectiveness with coolant flow rate, which matches the experimentally observed trend for all of the values of $I_{SS3,eq}$ tested except for the lowest two, which did not show a noticeable change in overall effectiveness with flow rate.

One possibility for the lack of improvement in $\overline{\phi_0}$ at the lowest flow rates is that the coolant distribution amongst the different rows of impinging jets did not increase uniformly as the flow rate was increased from $I_{SS3,eq} = 0.38$ to $I_{SS3,eq} = 0.64$, owing to the complex 3-dimensional nature of the internal velocity field. If at $I_{SS3,eq} = 0.38$ increasing the coolant flow rate had the effect of strengthening rows of impinging jets that were farther away from the surface being imaged by the IR camera while the impinging jets in the region near the row of film cooling holes remained unaffected, then $\overline{\phi_0}$ would show little or no increase in the region being studied. If the strengthening of the impingement jets with increasing $I_{SS3,eq}$ in this region is non-linear, the resulting change at low values of $I_{SS3,eq}$ may be very small. Even if the imping jets indeed get stronger with the small change in $I_{SS3,eq}$, the resulting change in $\overline{\phi_0}$ may have been smaller than the uncertainty in the surface temperature measurement.

The 1-D resistance model was also employed to calculate the area-averaged heat transfer coefficient, $\overline{\overline{h_i}}$, as a function of $I_{SS3,eq.}$, by using $\overline{\phi}_0$ along with with h_0 data measured previously by Dees et al. (2009) on a vane model of the same external geometry and flow conditions. Values were averaged over an area downstream of the film cooling holes from $x/d = 6$ to $x/d = 10$ where $\overline{h_i}$ appears relatively flat. It was seen that as the coolant flow was increased from $I_{SS3,eq.} = 0.38$ to 4.80, the calculated value of h_i increased by around 50%. It was not possible to find an impingement heat transfer correlation for comparison that was valid for the exact combination of the geometry and Reynolds number used during this study. However, two of the most closely applicable correlations found from the open literature show that the relative increase in h_i with $I_{SS3,eq.}$ should have been closer to 100% (de la Calzada and Alvarez, 2010) or 140% (Chupp et al., 1969) based on h_i scaling with Re_{jet} to a power of 0.45 or 0.7, respectively. The reason for the lower measured increase in h_i may be for the same reason just given for the small increases in $\overline{\phi}_0$ at low flow rates: as $I_{SS3,eq.}$ was increased, the impinging jets away from the row of film cooling holes may have experienced greater increases in coolant flow rate, and with less of an increase through impinging jets near the measurement region.

3.2 Internal Cooling and Film Cooling

This section will present results for test conditions which had one row of film cooling holes active on the suction side of the vane, in addition to the internal impingement cooling for which results have already been presented. First, the adiabatic effectiveness will be presented in order to highlight the physical behavior of the film cooling alone. Next, internal coolant temperatures will be presented and discussed, to be followed by measurements of temperature on the inner wall surface and external surface temperature measurements in terms of overall effectiveness. Finally, the effect of an increase in density ratio on the system will be presented.

3.2.1 Adiabatic Effectiveness Results

While this thesis primarily focuses on overall effectiveness data and other temperatures collected using a matched-Bi technique, behavior of film cooling alone is typically quantified using the adiabatic, or film, effectiveness first discussed in 1.2.2. Understanding how the film effectiveness varied with position and coolant flow rate is important for the appreciation of the overall effectiveness results where both film cooling and internal cooling were present. For the vane model discussed here, a separate experiment was run by fellow lab-mate Tom Dyson to measure the film effectiveness, η, by using a geometrically identical model but constructed from a polyurethane foam with a low thermal conductivity of $k = 0.048$ W/m-K. The surface temperature of this model was measured using the same infra-red thermography technique used for the matched-Bi model in the current study, and a "conduction correction" was applied to account for the fact that while the thermal conductivity of the foam was very low, it was not perfectly adiabatic as required by the definition of adiabatic effectiveness (Williams et al., 2012). While the open literature is full of η results for various film cooling geometries and flow conditions, direct measurements taken on the exact geometry tested here are important as a reference reference for comparing ϕ results against, and for capturing any effects of the of project-specific internal cooling geometry on the external flow field. Laterally averaged adiabatic effectiveness measurements from this experiment are shown in Figure 3.8, with the downstream edge of the film cooling hole represented by $x/d = 0$ the abscissa.

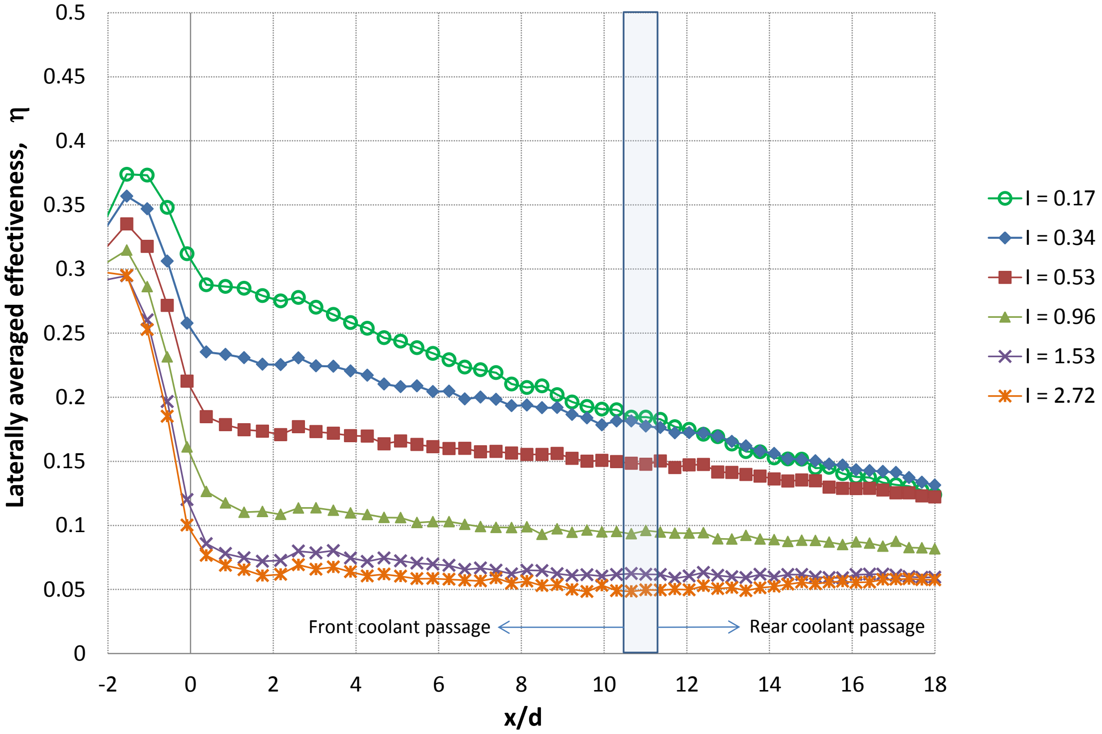

Figure 3.8: Laterally averaged adiabatic effectiveness, nominal $DR = 1.2$

The relatively flat curvature on the surface of the vane model measured here made comparisons to flat-plate data in the open literature possible. Figure 3.9 shows the measurements performed as part of this study along with with those published by Baldauf et al. (2002) and Waye and Bogard (2006), which have been adjusted to account for the difference in hole pitch. The measurements were in agreement (within the measurement uncertainty) and both show the same trend with increasing I.

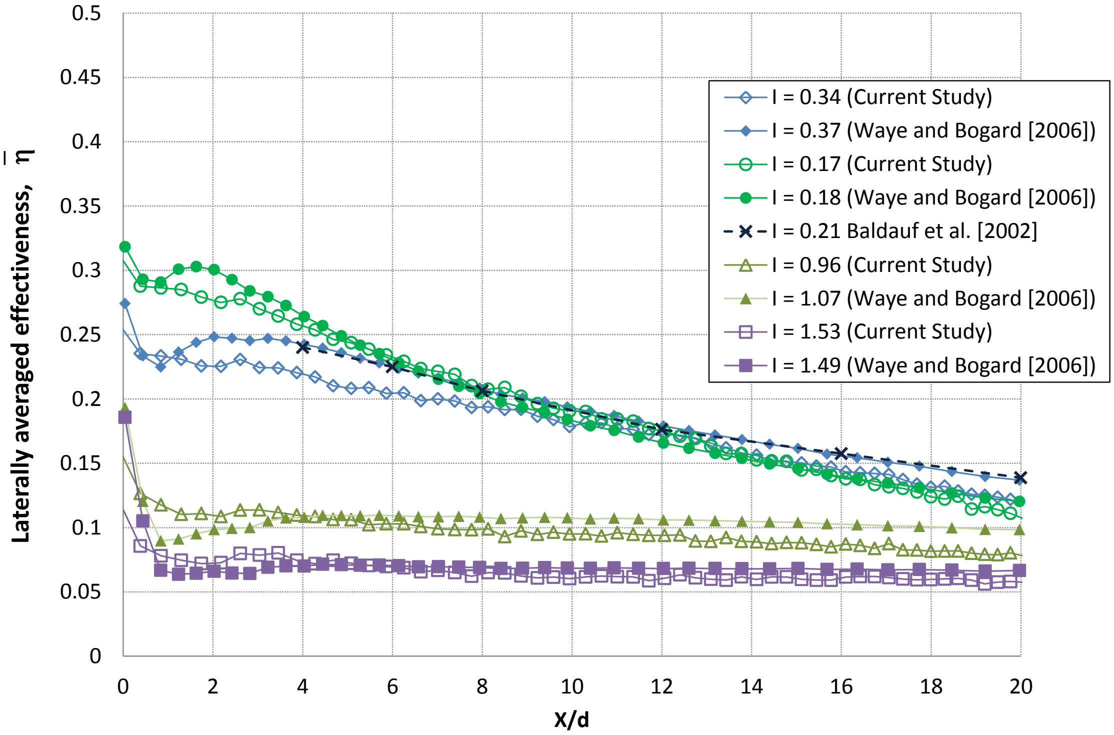

Figure 3.9: Comparison of $\overline{\eta}$ to published literature, nominal $DR = 1.2$

The single most important observation to be drawn from the $\overline{\eta}$ results shown here is that the maximum value of $\overline{\eta}$ was achieved at the lowest momentum flux ratio tested of $I_{SS3} = 0.17$, and as the coolant flow rate was increased $\overline{\eta}$ continually dropped. The cause of this drop in film effectiveness has been widely reported on in the open literature (Bogard and Thole, 2006), and is simply explained in terms of jet dynamics. At very low momentum flux ratios, film coolant is ejected from the film cooling holes and is almost immediately pushed against the external surface of the part wall by the mainstream flow and it continues travelling downstream along the external surface of the part wall, performing its function as coolant. However, as the jet momentum flux ratio is increased, the phenomenon of jet separation begins to occur as the momentum of the fluid ejected from the jet hole causes it to be projected farther into the mainstream flow and away from the surface which it is intended to protect. At sufficiently high flow rates, the jet projects far enough into the mainstream flow that it provides essentially no benefit and is said to be fully detached from the surface.

3.2.2 Internal Gas Temperatures with Internal Impingement and External Film Cooling

Before proceeding to discuss internal surface temperatures and overall effectiveness results for the matched-Bi model with film cooling, a comparison of internal gas temperatures between the film-cooled cases and the simulated "no film cooling" case where the middle two holes were taped over is helpful. In the same manner as presented in Section 3.1.2, Figure 3.10 displays the normalized internal gas temperatures which were measured at the lower of the two span-wise coolant instrumentation locations, for a film coolant momentum flux ratio of $I_{SS3} = 0.38$ and density ratio of $DR = 1.12$ (where DR is defined using the temperature of the gas at the exit of the film cooling holes, as shown in Equation 1.4). The normalized coolant temperatures are within a few percent of those shown in Figure 3.2, with the largest difference being an increase in θ_g at the coolant inlet for the case with film cooling active. Because the temperatures are all normalized between the mainstream temperature and the average of the two impinging jet temperature thermocouples, this indicates that as the coolant flowed from the inlet to the plenum and then impinging jet holes, it warmed up a few percent more for the test case where the film cooling holes were active than it did for the case where the middle two holes were taped. These small differences in temperatures from Figure 3.2, are not statistically significant when compared with the estimated uncertainty of $\delta\theta_g = \pm 0.022$, meaning the internal coolant temperatures in the vane model with all of the film cooling holes active are essentially the same as those measured when the middle two holes were taped over. This is an important conclusion, since the method of taping over the middle two holes to evaluate the overall effectiveness in the absence of film cooling relied on the assumption that taping over the holes had a negligible effect on the internal coolant flowing through the model.

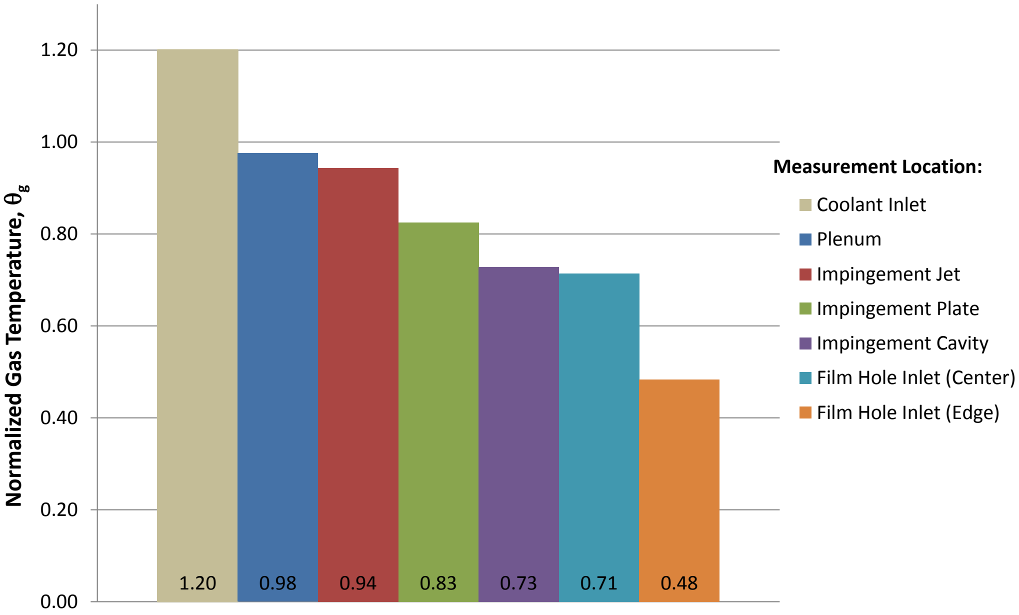

Figure 3.10: Internal coolant temperatures at various positions along the gas flow path with film cooling, lower span-wise location, $DR = 1.12$, $I_{SS3} = 0.38$

A comparison between gas temperatures at the two different span-wise measurements can be seen in Figure 3.11. The same span-wise temperature difference that was seen for the case with "internal impingement cooling only" persisted when all of the film cooling holes were active, and the differences in θ_g from the simulated "internal cooling only" results previously shown in Figure 3.3 were within the estimated measurement uncertainty of $\delta\theta_g = \pm 0.022$. The fact that the coolant temperatures were very similar at each span-wise locations for both the cases with and without film cooling suggests that whatever change in the internal coolant velocity field as a result of taping over the middle two film cooling holes was minor, lending some more validity to the method of taping over the holes.

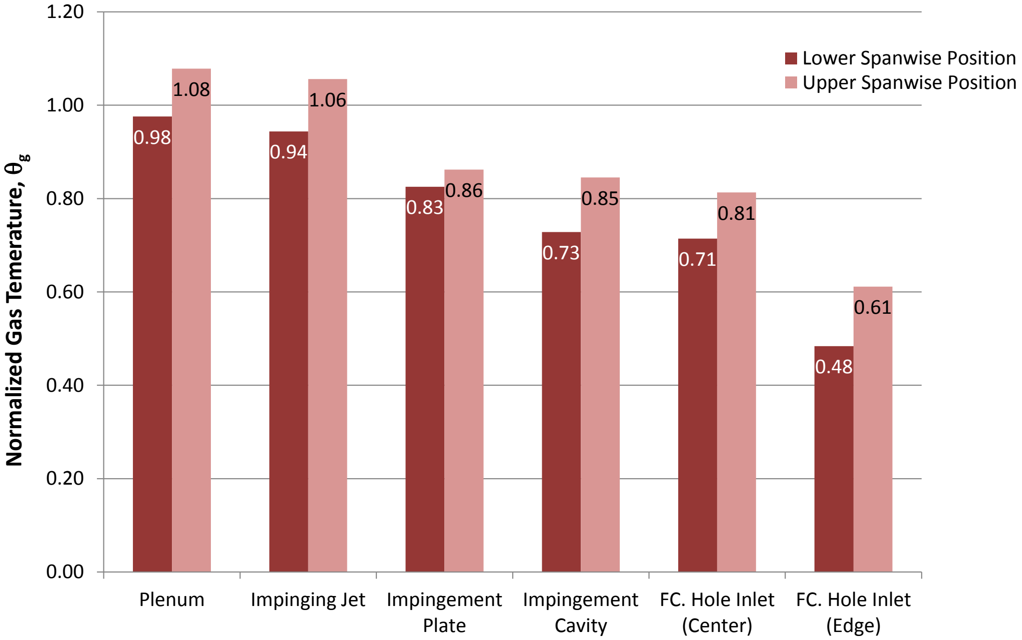

Figure 3.11: Comparison of internal coolant temperatures at two span-wise locations with film cooling active, $DR = 1.12$, $I_{SS3} = 0.38$

Also seen again in Figure 3.11 is that the impingement plate temperature at the upper span-wise instrumentation location was nearly the same as the temperature in the impingement cavity, which may be explained by the high levels of turbulent mixing that were present in the impingement cavity, leading to a very high convection heat transfer coefficient on the downstream side of the impingement plate. That this only happened at the upper span-wise instrumentation location suggests that the impinging jets could have been stronger near the top of the vane than they were at the lower part of the vane. This would be the case if, as mentioned in Section 3.1.2, the coolant was jetting upwards from the inlet at the front of the model, striking the inside of the top mounting plate, as this would increase the pressure at the top of the model and would tend to drive more flow through the impingement plate near the top.

The effect of increasing the coolant flow rate on internal coolant temperatures for the film-cooled case may be seen in Figure 3.12. Normalized temperatures are shown for two different span-wise locations, for both an impinging jet and the center of a film cooling hole. Also shown is θ_g measured at the inlet of the coolant to the base of the vane model. The overall trends were nearly the same as for the non-film-cooled case. At the lowest value of I_{SS3} there existed the greatest spread between the coolant temperature measurements at different positions, while the difference generally decreased as the momentum flux ratio was increased.

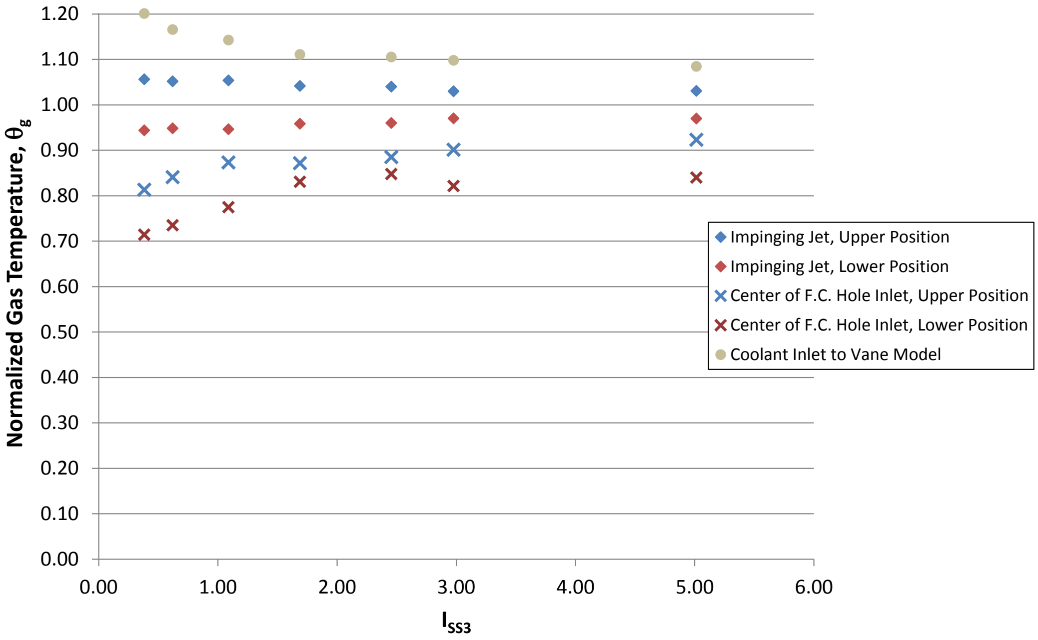

Figure 3.12: Variation of span-wise coolant temperatures with coolant flow rate, film cooling active, nominal $DR_{SS3} = 1.14$

3.2.3 Internal surface temperatures with internal impingement and external film cooling

Contrary to the internal gas temperatures which experienced very little change when all of the film cooling holes were active relative to the simulated “internal cooling only” case, the inner wall surface temperatures were very different with all of the film cooling holes active. Figure 3.13 shows the normalized inner wall surface temperatures, $\theta_{w,i}$, with the film cooling active as a function of the momentum flux ratio, I_{SS3}.

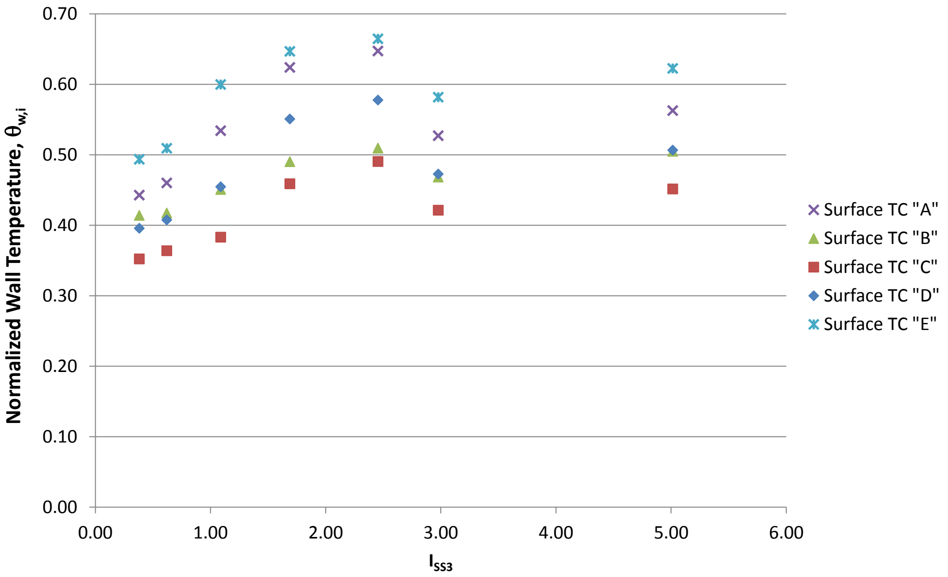

Figure 3.13: Variation of internal wall surface temperatures with coolant flow rate, film cooling active, nominal $DR_{SS3} = 1.14$

The spread amongst the five thermocouples can be attributed to the differences in thermocouple location, both span-wise and stream-wise. In contrast with the non-film cooled case shown previously in Figure 3.6 where the inner surface became progressively colder as the coolant flow rate was increased, values of $\theta_{w,i}$ increased with momentum flux ratio up to a peak at $I_{SS3} = 2.46$ before dropping of as the momentum flux ratio was increased further to $I_{SS3} = 2.98$. It was previously shown in Figure 3.7 that the overall effectiveness resulting from internal cooling alone increased continually with I_{SS3} while film (adiabatic) effectiveness decreased as I_{SS3} was increased as shown in Figure 3.8, so it was reasoned that a peak in overall effectiveness and $\theta_{w,i}$ with both internal and film cooling would be expected at some optimal value. However, the peak in $\theta_{w,i}$ happened at a much higher I_{SS3} than expected based solely on film effectiveness.

The existence of the peak value for $\theta_{w,i}$ seen in Figure 3.13 was seen in two different experiments, adding credibility to the data. After the existence of a peak in performance was seen in the first experiment, a second experiment was performed, in part to expand upon the range of conditions tested, as well as to verify that the results were repeatable after setting up and performing the experiment on a different day (nearly one month later in this case.) A comparison of $\theta_{w,i}$ values measured on the two different test days were previously shown in Figures 2.20 and 2.21, for internal surface thermocouples "A" and "B", respectively. Good agreement was seen between the two different experiments, verifying the presence of the peak in effectiveness; the small differences seen between the two experiments is likely due to uncertainty in the measured coolant flow rate.

A more direct view of the effect of film cooling on $\theta_{w,i}$ is given in Figure 3.14, where measurements from two surface thermocouples are compared between the case with simulated "internal cooling only" and the case with all of the film cooling holes active. The measured data points are represented with symbols and smoothed lines have been fit through the data points for the ease of visualizing the differences in trends with I_{SS3} between the different cases.

From a 1-D heat transfer perspective, the addition of film cooling reduces the driving potential for heat transfer through the component wall as the film coolant

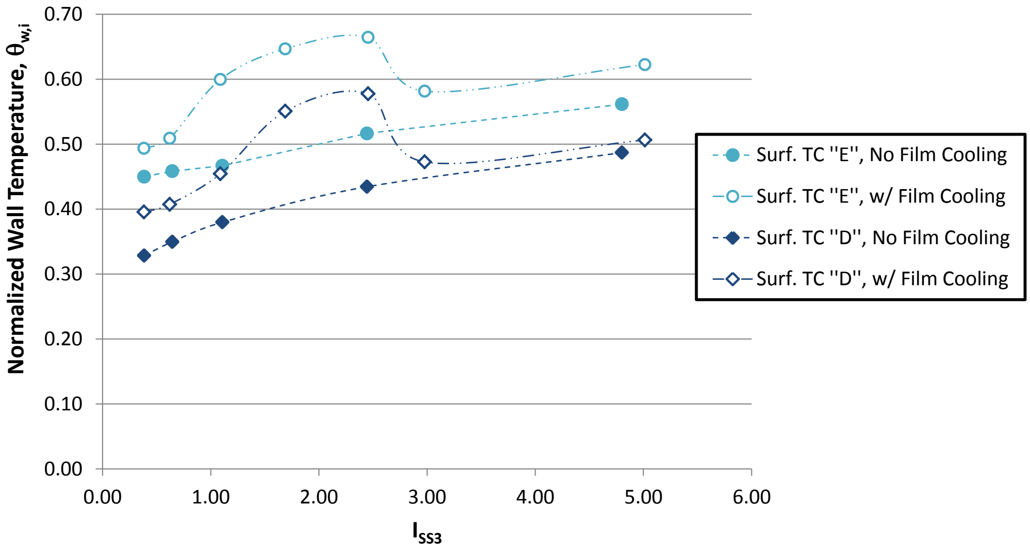

Figure 3.14: Effect of film cooling on internal wall surface temperatures, nominal $DR_{SS3} = 1.14$

flows over the external surface of the part. Using the simple resistance model shown in Figure 1.7, this should result in both lower q" and reduced temperature (greater θ) of the inner wall. It is easily seen that at the lowest I_{SS3} values, film cooling provided a modest increase in $\theta_{w,i}$ of 20% and 10% for surface thermocouples "D" and "E", respectively. This increase with film cooling became greater as the coolant flow rate increased up until the peak at $I_{SS3} = 2.46$, resulting in an improvement in $\theta_{w,i}$ of about 29% to 30% for the two thermocouple locations. As the momentum flux ratio was further increased to $I_{SS3} = 2.98$, the film cooled cases showed a sharp drop in $\theta_{w,i}$ and the addition of film cooling contributed very little at and above this momentum flux ratio. The drop in normalized temperature did not only occur on the inner wall surface - the results to be presented in the following section will show that $\overline{\phi}$ also experienced a drop at $I_{SS3} = 2.98$ as well. These relatively small increases in $\theta_{w,i}$ due to film cooling highlight the dominance of the internal impingement cooling as the primary mechanism for cooling the inner wall surface, with film cooling being of secondary importance.

While the momentum flux ratios of $I_{SS3} = 1.09$ through 2.46 showed the most pronounced increase in $\theta_{w,i}$ with film cooling, the film effectiveness at these momentum flux ratios was very low, around $\overline{\eta} = 0.05$, as presented in Figure 3.8, presumably due to jet detachment. With such low values of film effectiveness and the dominance of internal impingement cooling, the larger contributions with film cooling at these intermediate flow rates may be attributed to a "reconfiguring" of the internal impinging jets when the middle two film cooling holes were un-taped which increased the internal cooling in the measurement region. Although this cannot be confirmed without knowing more details about the internal flow field, the scope of which is beyond this thesis, this explanation is the best which can be made from the data collected. It makes sense that because all of the coolant flowing through the impinging jets was exhausted through the film cooling holes, taping over the two film cooling holes nearest to the internal surface thermocouples would cause some decrease in strength of the closest impinging jets and possibly alter the location at which they contacted the inner wall surface.

The addition of film cooling also helped to cool the part by convection in the film cooling holes, providing extra cooling in regions near the row of film cooling holes. Surface thermocouple "E" was less than a hole diameter downstream of the film cooling hole breakout and "D" was a few hole diameters downstream as shown in Figure 2.10. This additional convective cooling was only present when the film cooling holes are active and as such would not be included in the film effectiveness results even though the cooling mechanism was not truly "film cooling". The amount of in-hole convective cooling would be expected to increase along with I_{SS3}, partially offsetting the drop in $\overline{\eta}$ especially near the holes, with the net result that activating the film cooling and increasing the flow rate provided more cooling than the adiabatic effectiveness alone would indicate.

Additionally, adiabatic effectiveness by definition assumes an adiabatic part wall, and doesn't include the effect of coolant pre-heating that was present in the thermal conducting model. This pre-heating reduces the cooling potential of the film coolant as discussed in Section 1.3 which is represented by a decrease in χ in Equation 1.15. At the lowest value of $I_{SS3} = 0.38$, the amount of coolant warming seen was $\chi = 0.70$, indicating that the coolant had already lost 30% of its film cooling potential by the time it was ejected from the holes, reducing the true amount of film cooling. As the mass flow rate of coolant increased, χ increased by 11% to $\chi = 0.78$. Since it was shown that $\overline{\eta}$ dropped by more than 70% across the range of jet momentum flux ratios tested, this increase in χ was not enough to make up for the loss of film effectiveness at higher momentum flux ratios, supporting the idea of a "reconfiguring" of the impingement jets and in-hole convection as causes for the boost in $\theta_{w,i}$ for the "with film cooling" cases.

The sharp drop in $\theta_{w,i}$ above $I_{SS3} = 2.98$ is not easily explained from the current data, but could be caused by multiple phenomenon. First, a "reconfiguring" of the internal impinging jets at and above this momentum flux ratio could have caused a drop in internal cooling. This is supported by a smaller drop in $\overline{\phi}$ values which will be further discussed in Section 3.2.4. A second contributing effect could be an increase in the external heat transfer coefficient downstream of the film cooling holes when the jet momentum flux ratio is pushed above some threshold. The external surface heat transfer coefficient is frequently augmented by the addition of film cooling jets, which can increase turbulence levels near the surface of the part and can also disturb the external boundary layer. It is possible that as the mainstream air flowed over the vane surface and interacted with the film cooling jets, vortical flow structures were formed which greatly increased the thermal transport from the surface. This would result in a decrease in ϕ for the external surface, accompanied by a drop in $\theta_{w,i}$.

3.2.4 External Surface Temperatures with Internal Impingement and External Film Cooling

Overall effectiveness may be considered the most important figure of merit for actively cooled gas turbine engine components since the whole purpose of using an active cooling strategy is to keep the metal surface temperatures within allowable limits, and the overall effectiveness is by definition a representation of the external metal surface temperature. Laterally averaged values of overall effectiveness are shown in Figure 3.15 for the range of momentum flux ratios tested. For the condition of $I_{SS3} = 0.38$, both the initial measurement and the mid-test repeat are shown, which together give an indication of the amount of uncertainty in the dataset. A "knee" in each of the curves occurs at a downstream distance of about $x/d = 11$, where an internal wall divides the front and rear internal coolant passages. This "knee" occurs because the front and rear coolant passages each had different internal cooling conditions as previously discussed. At the lower values of momentum flux ratio between $I_{SS3} = 0.38$ and $I_{SS3} = 1.09$, the changes in $\overline{\phi}$ with momentum flux ratio are negligible, compared to the uncertainty and in-test repeatability of the measurement. Further increasing the coolant flow rate caused the overall effectiveness to increase to a maximum value at $I_{SS3} = 1.69$, beyond which overall effectiveness downstream of the holes decreased. It should be noted that very close to the film cooling hole (the downstream edge of which is at $x/d = 0$), overall effectiveness remained high because of the cooling which occurred due to convection inside of the

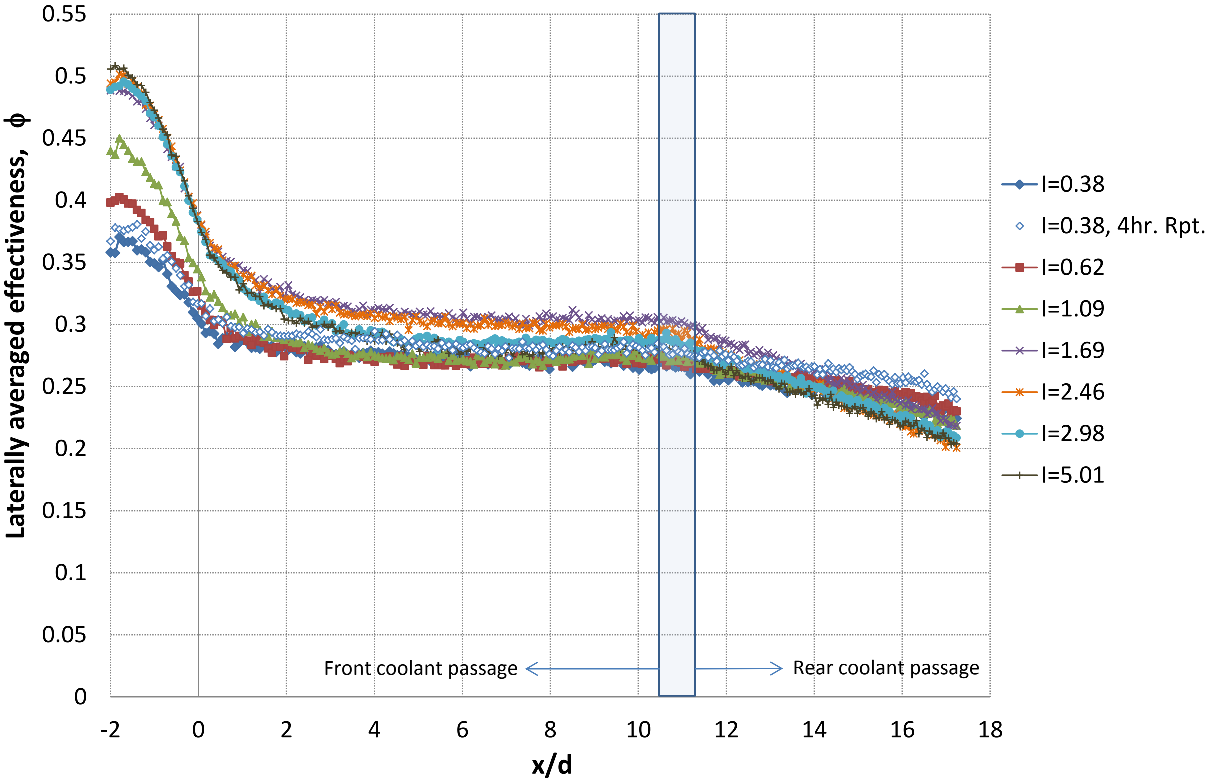

Figure 3.15: Laterally averaged overall effectiveness, film cooling active, nominal $DR_{SS3} = 1.14$

film cooling hole and undoubtedly strengthened as the flow rate though the jets was increased. At the highest momentum flux ratio, overall effectiveness downstream of the holes had decreased to approximately the value measured without film cooling at the same flow rate, presumably because at such a high momentum flux ratio the film cooling jets were completely detached from the vane surface, preventing the coolant from functioning as a protective film and leaving internal impingement as the primary cooling mechanism. While the values at the highest and lowest momentum flux ratios are essentially the same, this is most likely a coincidence since two different cooling mechanisms are primarily responsible for keeping the part cool at these two very different flow rates.

It is important to note here that the trend seen in the $\overline{\phi}$ values with increasing I_{SS3} stand in contrast to those measured by Dees et al. (2011b), who were responsible for the only other experimental study of overall effectiveness measured downstream of a single row of film cooling holes on the suction side of a matched-Bi vane. Dees et al. employed an internal cooling scheme which essentially held h_i (and therefore $\overline{\phi_0}$) constant while I was increased, and as a result their data showed that $\overline{\phi}$ dropped due to decreasing $\overline{\eta}$ as the jets began to detach from the vane surface with increasing I values.

To highlight the similarities and differences in behavior of the internal and external surface temperatures with and without film cooling, Figure 3.16 presents a direct comparison between $\overline{\overline{\phi}}$, which was averaged over downstream distance from $x/d = 4$ to $x/d = 10$ where $\overline{\phi}$ was relatively flat, and the previously shown $\theta_{w,i}$ data. It is seen that at the lowest momentum flux ratios, $\overline{\overline{\phi}}$ and $\theta_{w,i}$ experience a similar increase when the film cooling was added. However, in the intermediate ranges of I_{SS3} where $\theta_{w,i}$ experienced a large increase with the addition of film cooling, $\overline{\overline{\phi}}$ showed a much smaller increase and subsequently a much smaller drop than $\theta_{w,i}$ at $I_{SS3} = 2.98$. The fact that the external surface temperature change was smaller than the internal change reinforces the idea that a "reconfiguring" of the internal impinging jets when the middle two film cooling holes were unblocked was primarily responsible for the large increase and subsequent decrease in $\theta_{w,i}$.

When overall effectiveness values are laterally averaged, spatial detail is lost which may reveal certain nuances of the data. For this reason, it was useful to examine 2-dimensional contour plots of the regions which were laterally averaged. These 2-D contour plots are shown below in Figures 3.17 - 3.25 for the film cooled cases, which includes the first in-test repeat of $I_{SS3} = 0.38$ to give a visible indicator of the

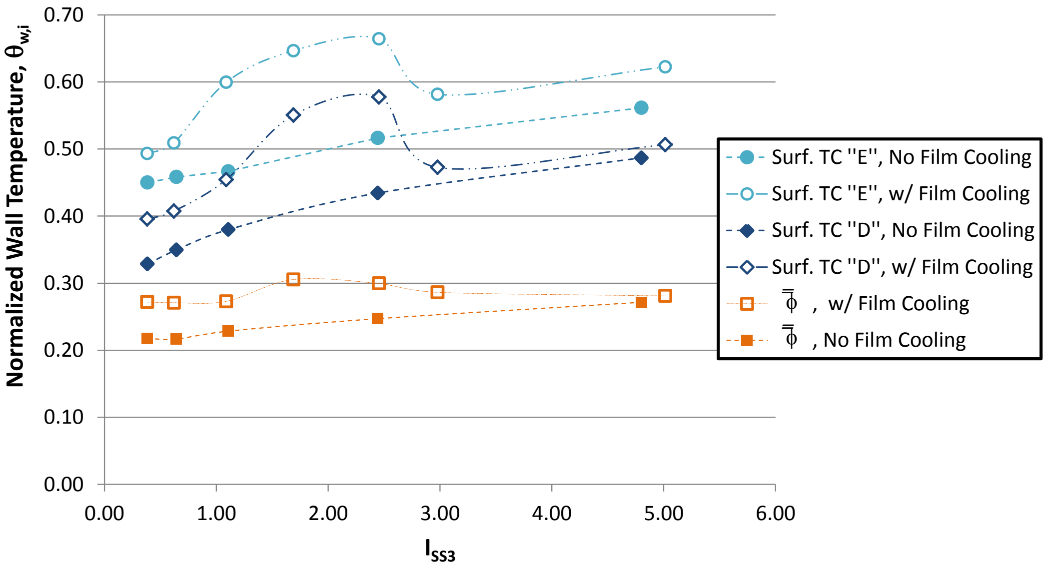

Figure 3.16: Comparison of $\bar{\bar{\phi}}$ and $\theta_{w,i}$ vs. I_{SS3}, with and without film cooling

level of uncertainty which was present in the measurements. The areas shown cover two entire cooling jet pitches, from mid-pitch to mid pitch, with the film cooling hole center-lines located at span-wise positions of z/d=2 and z/d=6 on the vertical axis. It is important to note that in the region inside the cooling hole (upstream of $s/d = 0$), the exact value of the contours are not valid since the IR calibration curve used to process the images does not reach such a low temperature as existed in the hole. The contour levels in the hole are valid, however, for drawing qualitative comparisons.

These 2-D ϕ distributions generally show the same trends that were seen in the laterally averaged values. As was seen in the laterally averaged values, the 2-D contour plots clearly show the drop in ϕ downstream of the holes as the momentum flux ratio was increased from $I_{SS3} = 2.46$ to $I_{SS3} = 2.98$. However, one significant detail is seen in the 2-D ϕ distributions which is not apparent from the $\bar{\phi}$ values. When looking at the laterally averaged values shown in Figure 3.15, there appeared to be little difference between $\bar{\phi}$ for the highest and lowest I_{SS3} values tested, over

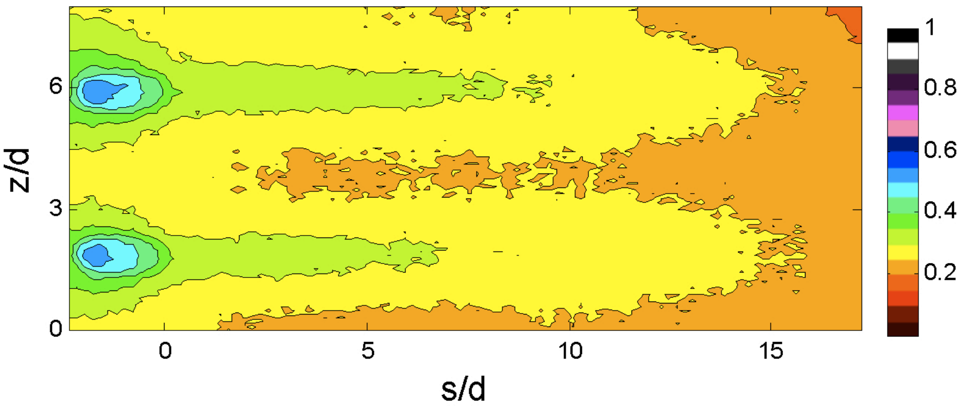

Figure 3.17: Overall effectiveness with film cooling active, $I_{SS3} = 0.38$, $DR_{SS3} = 1.12$

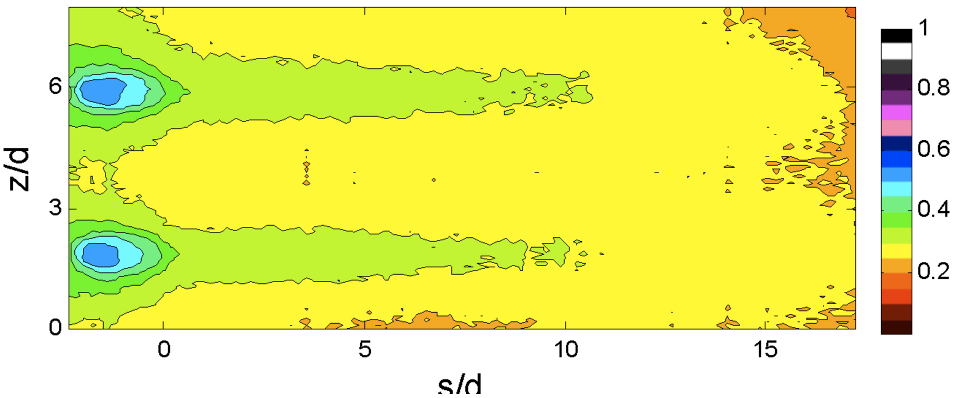

Figure 3.18: Overall effectiveness with film cooling active, first repeat of $I_{SS3} = 0.38$, $DR_{SS3} = 1.12$

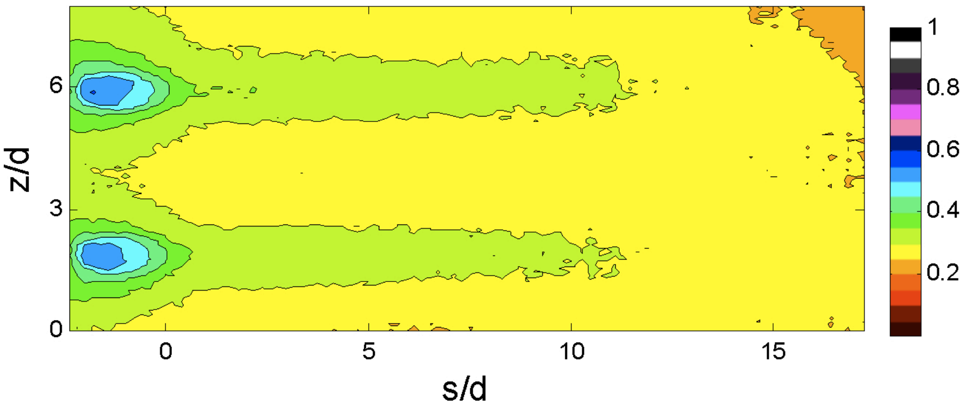

Figure 3.19: Overall effectiveness with film cooling active, second repeat of $I_{SS3} = 0.38$, $DR_{SS3} = 1.12$

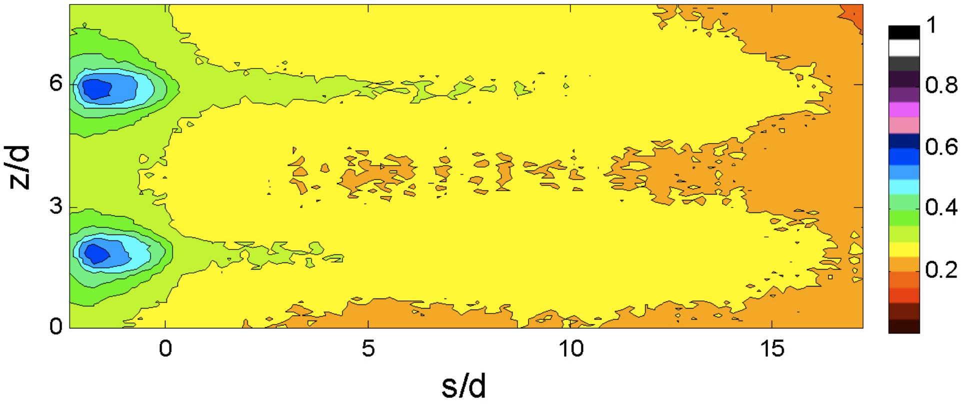

Figure 3.20: Overall effectiveness with film cooling active, $I_{SS3} = 0.62$, $DR_{SS3} = 1.13$

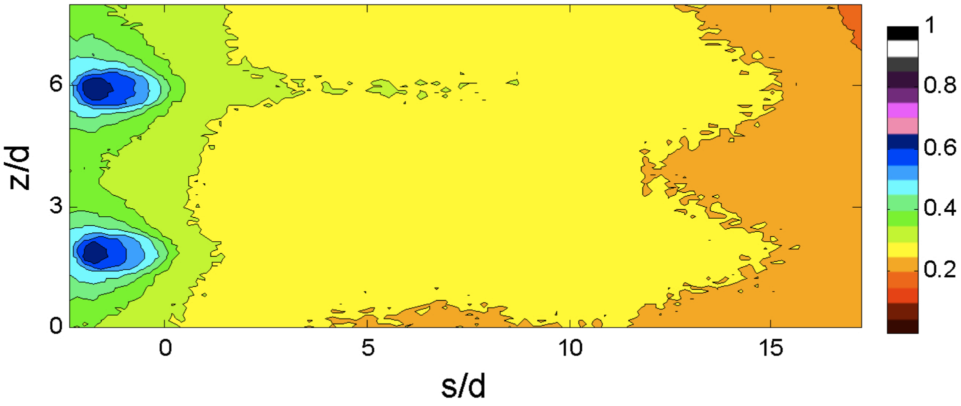

Figure 3.21: Overall effectiveness with film cooling active, $I_{SS3} = 1.09$, $DR_{SS3} = 1.14$

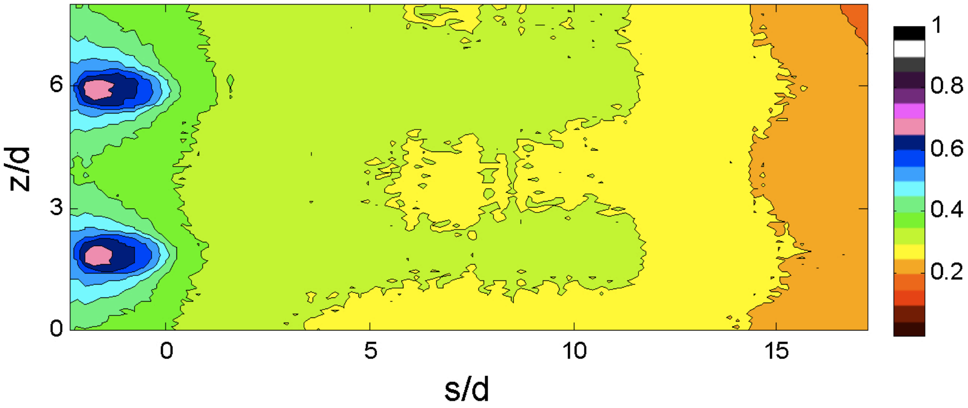

Figure 3.22: Overall effectiveness with film cooling active, $I_{SS3} = 1.69$, $DR_{SS3} = 1.15$

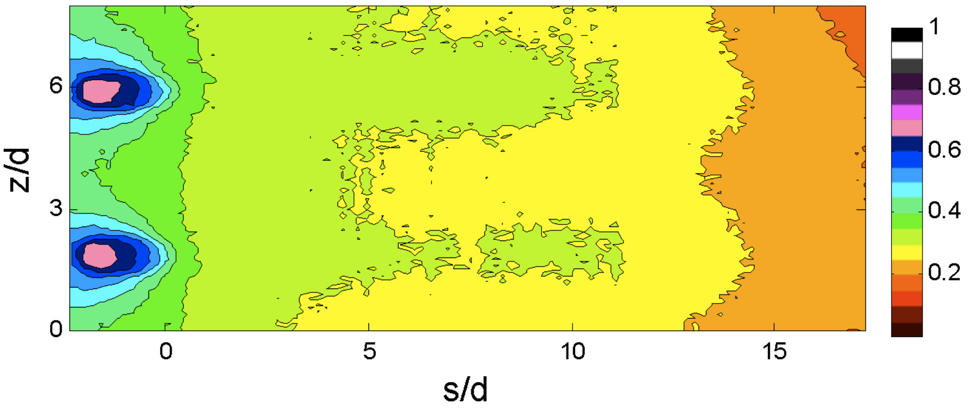

Figure 3.23: Overall effectiveness with film cooling active, $I_{SS3} = 2.46$, $DR_{SS3} = 1.16$

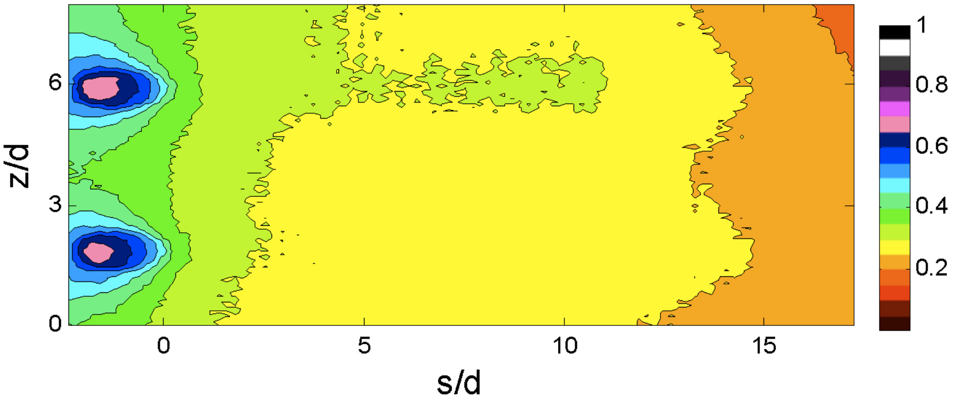

Figure 3.24: Overall effectiveness with film cooling active, $I_{SS3} = 2.98$, $DR_{SS3} = 1.16$

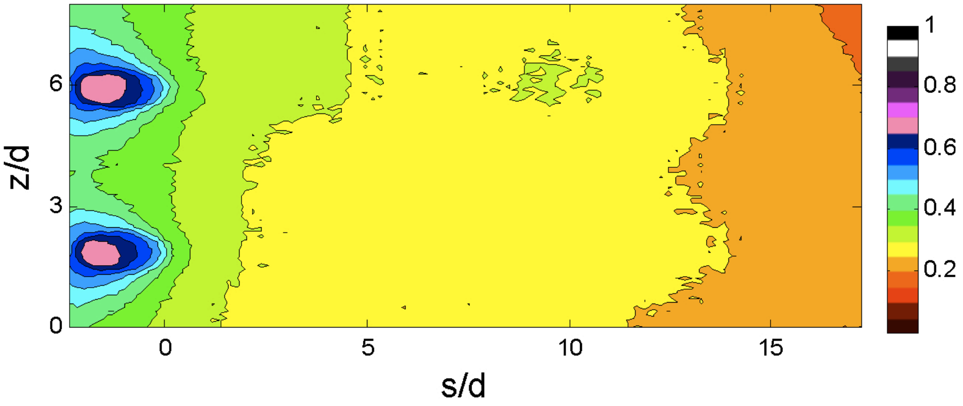

Figure 3.25: Overall effectiveness with film cooling active, $I_{SS3} = 5.01$, $DR_{SS3} = 1.17$

a downstream distance of about $x/d = 4$ to $x/d = 14$. When looking at the 2-D contours, it is evident that significant lateral gradients existed at the lower flow rates, with higher contour levels directly downstream of the jet holes and relatively warm regions existing mid-pitch between the pair of jets. At the higher momentum flux ratios of $I_{SS3} = 2.98$ and $I_{SS3} = 5.01$, contours just downstream of the jet holes were much less distinct and showed less span-wise variation. The physical reason for this is that at lower momentum flux ratios the film cooling jets remained attached to the surface and made a more significant contribution to overall effectiveness directly downstream of the holes than they did between the holes. At the higher momentum flux ratios where η would be much lower, overall effectiveness was dominated by the internal impinging jets, which were more evenly distributed over the internal surface in both the lateral and stream wise directions. Although conduction within the part has the effect of smoothing out thermal gradients, the lateral gradients are still clearly visible with the film cooling active. This is important since from a durability perspective, the regions of highest component temperature are what matters most, and in this case the lower momentum flux ratios actually resulted in higher component temperatures mid-pitch despite having similar $\overline{\phi}$ values to the highest momentum flux ratios.

While the film cooling jets detach from the surface at high momentum flux ratios and become ineffective, the effect of convective cooling inside the film cooling holes only gets stronger as the flow rate is increased, and this is clearly seen in the contour plots. Starting at the lowest momentum flux ratio of I_{SS3} in Figure 3.17 and examining ϕ inside and in the near vicinity of the film cooling holes as the momentum flux ratio was increased up to $I_{SS3} = 1.69$ in Figure 3.22, it was seen that the region around and between the film cooling holes continually became colder as the flow rate increased. Proceeding to the highest flow rates of $I_{SS3} = 2.46, 2.98$, and 5.01, shown in Figures 3.23, 3.24, and 3.25, respectively, there was little noticeable change in the contour levels in and around the hole with increasing flow rate, even when the overall effectiveness downstream of $x/d = 2$ dropped. One explanation may be that the increase in convection within the holes was a non-linear function of coolant flow rate, such that at high flow rates much larger increases in momentum flux ratio would be needed to provide the the same increase in convective cooling. Another possibility is that because of heat conduction through the part in the stream-wise direction and the fact that the overall effectiveness downstream of the holes decreased at the highest momentum flux ratios, convective heat transfer inside the film holes may indeed have increased along with coolant flow rate, but the surface temperatures near the hole didn't change enough to cause a noticeable difference in contour level as more heat was conducted downstream.

Several of the contour plots of $\overline{\phi}$ show higher values of overall effectiveness downstream of the upper-most jet at $z/d = 6$ than for the lower jet at $z/d = 2$. Although a difference in mass flow through each of the jets could cause this sort of non-uniformity, it is important to keep in mind that because the vane model was matched-Bi and conducting in nature, the overall effectiveness was also sensitive to internal cooling. Therefore, the differences seen between the jets may be caused by the span-wise temperature gradient which was observed in the coolant temperatures discussed in Section 3.2.2. If the coolant inside the vane was colder near the top of the vane, it would be natural for the internal and external surfaces of the vane wall to be colder near the top as well, which would have increased the size of the overall effectiveness contour for the upper jet as observed. Also, the pitch of the internal impinging jets was not the same as the pitch of the film cooling holes, so that the internal and external jets were not consistently aligned in the span-wise direction which may contribute to the observed gradient.

While the existence of an optimal momentum flux ratio resulting in peak cooling performance was not surprising, the fact that this peak in $\overline{\phi}$ occurred at $I_{SS3} = 1.69$ was unexpected. The results shown for the non-film-cooled case revealed that, based on internal cooling alone, the overall effectiveness increased monotonically due to the increase in impinging jet strength. It was also shown that the film effectiveness, η, peaked at the lowest momentum flux ratio tested of $I_{SS3} = 0.17$, which is much lower than the value of $I_{SS3} = 1.69$ at which $\overline{\phi}$ peaked.

One reason that the overall effectiveness did not drop off at lower values of I_{SS3} with both impingement and film cooling present, as would have been expected for the film alone, is that the drop in film effectiveness with increasing momentum flux ratio was offset by the increase in impingement cooling which was shown in Figure 3.7, along with the decreased coolant pre-heating at higher mass flow rates. As I_{SS3} was increased beyond 1.69, however, the increase in h_i and χ was presumably not enough to offset the effects of jet detachment, resulting in a drop in $\overline{\phi}$.

One important consideration when interpreting experimental results is how repeatable the results are. The most astonishing results in the world are meaningless if they cannot be duplicated. As unexpectedly high as the I_{SS3} value was where performance started to decrease, it was observed in two different experiments, performed one month apart from each other, during which time the wind tunnel facility had a new mainstream flow heat exchanger installed. Good agreement was seen between the two tests, as already mentioned in the discussion of experimental uncertainty in Section 2.5, lending credibility to the results.

To get a better understanding of the contribution of film cooling to overall effectiveness, comparisons can be directly made between the measured overall effectiveness with and without film cooling. Figure 3.26 shows the values of $\overline{\phi}$ which were measured at the lowest three I_{SS3} values for cases in which film cooling was present, as well as $\overline{\phi_0}$ for the simulated non-film-cooled configuration.

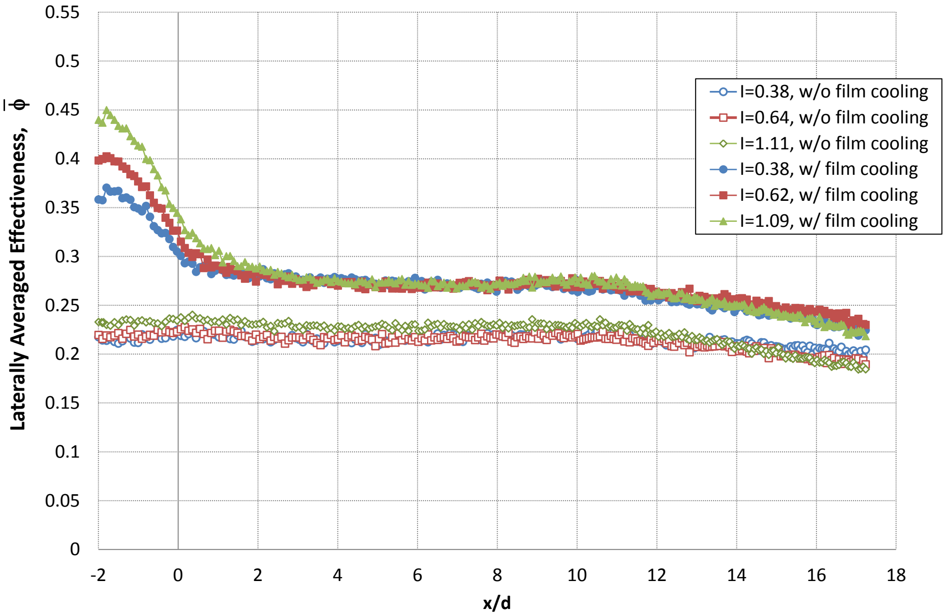

Figure 3.26: Effect of film cooling on $\overline{\phi}$, nominal $DR_{SS3} = 1.14$

Comparing the two different cooling configurations, a significant improvement was seen with the addition of film cooling at all three momentum flux ratios. However, the fact that all three showed similar improvements with film cooling downstream of the holes was surprising, since the film effectiveness was the highest at $I_{SS3} = 0.38$ and had decreased by nearly a factor of two as the momentum flux ratio was increased $I_{SS3} = 1.09$, as seen in Figure 3.8. Since $\overline{\phi_0}$ remained constant while film effectiveness decreased with increasing I_{SS3}, it was expected that $\overline{\phi}$ would decrease as well. Because these overall effectiveness measurements were measured using the matched-Bi approach, it is possible that conjugate heat transfer effects were responsible for the deviation between the measurements and what was expected based on the film behavior alone. Although it remains beyond the scope of this thesis, CFD models which incorporate conjugate heat transfer effects may shed light into the physical behavior of the system and could be used to further investigate why overall effectiveness didn't drop along with film effectiveness for these three cases.

As the momentum flux ratio was increased to $I_{SS3} = 2.3$, the addition of film cooling continued to provide an improvement in $\overline{\phi}$ of 20%, as seen in Figure 3.27. At this high of a momentum flux ratio, the coolant jets should have been detached from the vane surface, dramatically decreasing the film effectiveness due to entrainment of hot mainstream gas beneath the separated jet (Baldauf et al., 2002). With the jet nearly completely detached from the vane surface, the improvement in $\overline{\phi}$ was expected to be smaller than the 20% improvement observed.

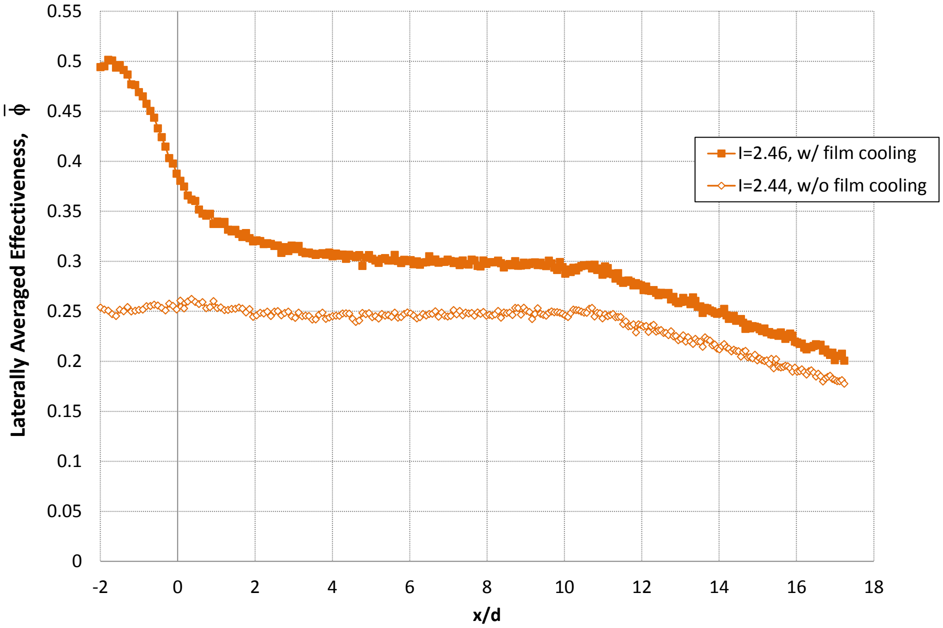

Figure 3.27: Effect of film cooling on $\overline{\phi}$, $DR_{SS3} = 1.14$

The effect of the addition of film cooling on $\overline{\phi}$ for the maximum momentum flux ratio tested of $I_{SS3} = 5.01$ can be seen in Figure 3.28. Just downstream of the film cooling holes at $x/d = 0$, there was a significant improvement in overall effectiveness due to strong convective heat transfer which occurred inside the film cooling holes. However, there was almost no contribution to overall effectiveness due to the presence of film cooling farther downstream of this region. This is consistent with the understanding that at very high momentum flux ratios, the detachment of the film cooling jet and decrease in η associated with it leave internal impingement alone to keep the vane cool.

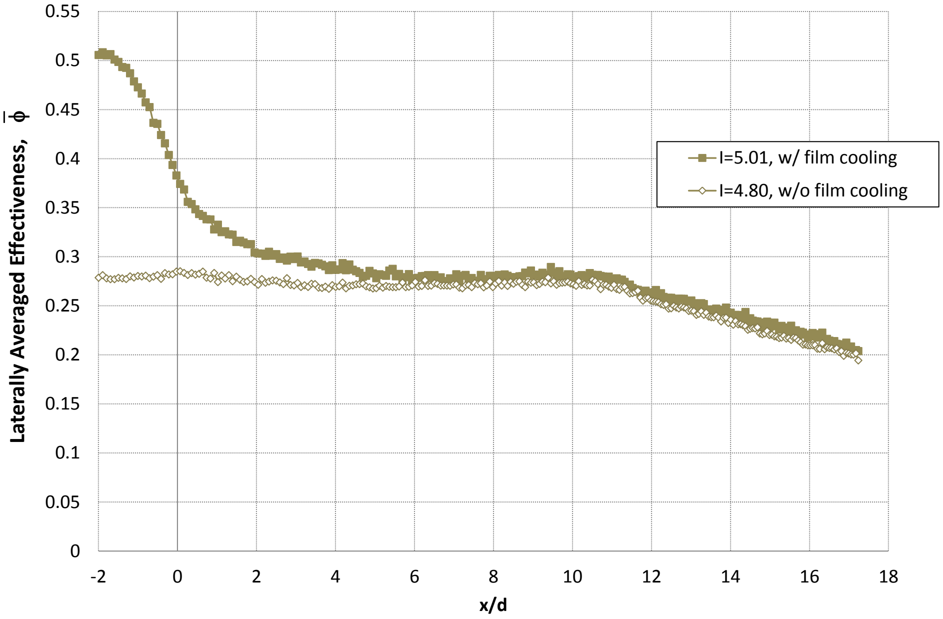

Figure 3.28: Effect of film cooling on $\overline{\phi}$, $DR_{SS3} = 1.17$

3.2.5 Overall effectiveness prediction through 1-D analysis

It was shown in Section 1.3 that a simple 1-dimensional analysis of heat transfer through a plane wall could be used to relate ϕ to ϕ_0 and η for a idealized part geometry with external film and internal cooling through Equation 1.15. One motivation for applying this simplified analysis is that measurements of ϕ_0 and η may be easier to acquire than measurements of ϕ. The dataset collected as part of this thesis provided a good opportunity to apply this simplified analysis, and measurements of $\overline{\phi}_0$ and χ were used along with $\overline{\eta}$ measurements collected by lab mate Tom Dyson to predict

$\overline{\phi}$, which was then compared with the $\overline{\phi}$ values measured during the current study. Predicted values for laterally averaged overall effectiveness, $\overline{\phi}_p$, are compared directly with the measured $\overline{\phi}$ along with $\overline{\phi}_0$ for reference in Figures 3.29a through 3.29d. It

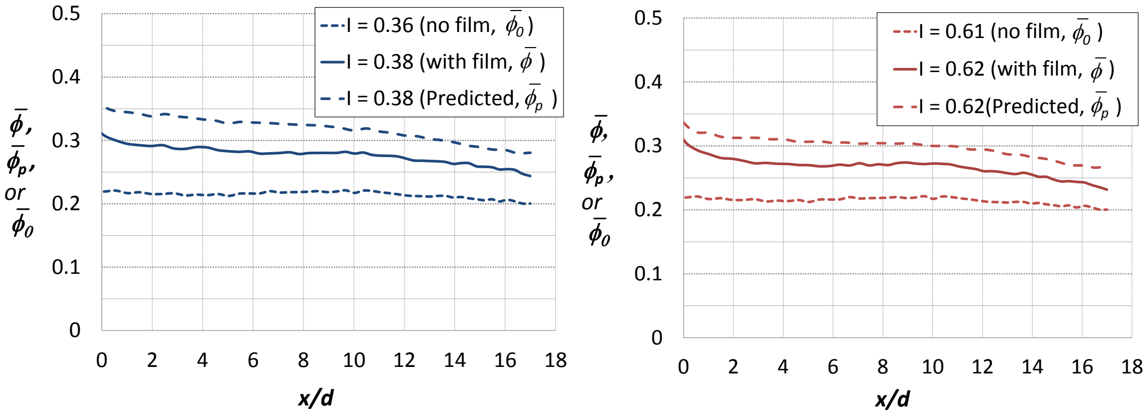

(a) $I_{SS3} = 0.38$

(b) $I_{SS3} = 0.62$

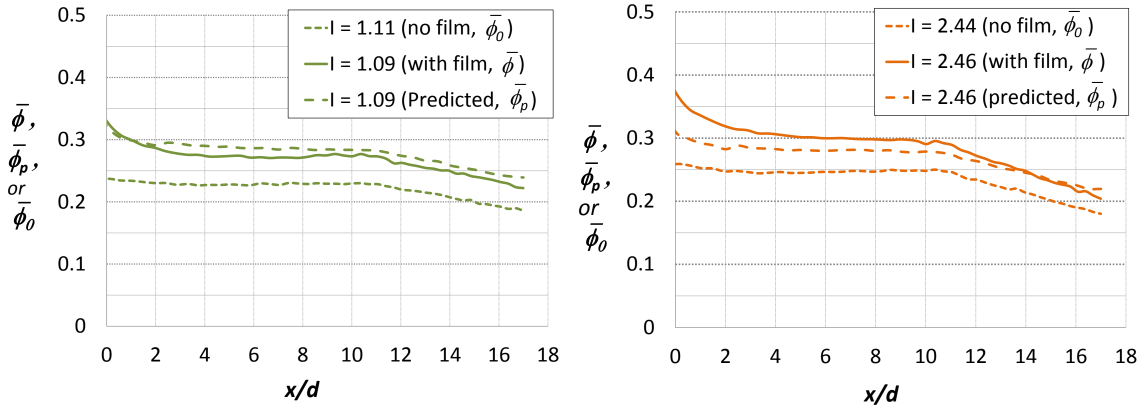

(c) $I_{SS3} = 1.09$

(d) $I_{SS3} = 2.46$

Figure 3.29: Comparison of $\overline{\phi}$ with 1-D prediction from $\overline{\phi_0}$ and $\overline{\eta}$

was seen that for the lower two momentum flux ratios of $I_{SS3} = 0.38$ and 0.62, the 1-D analysis significantly over-predicted overall effectiveness. At the intermediate value of $I_{SS3} = 1.09$ the simplified analysis fared better and $\overline{\phi}_p$ was in good agreement with $\overline{\phi}$, as shown in Figure 3.29c. However at the highest momentum flux ratio of $I_{SS3} = 2.46$ the 1-D analysis again failed to match the experimental results, this time under-predicting the overall effectiveness as seen in Figure 3.29d.

The lack of agreement between predicted and measured $\overline{\phi}$ values is very likely due to a breakdown of some of the assumptions used in the derivation of Equation 1.15. The first of these assumptions which is suspect is that the heat transfer through the wall was 1-dimensional. While there may be certain regions in the airfoil where this assumption may be sufficiently accurate, strong temperature gradients in both the lateral and stream-wise directions existed in the vicinity of the film cooling holes, violating this assumption. Also, the impinging jets were distributed in a 2-dimensional array over the inner surface of the vane, and the resulting 2-D internal cooling distribution along with the internal dividing wall at $x/d = 11$ could have lessened the accuracy of the 1-D assumption.

A second assumption used in the derivation of Equation 1.15 is that T_{aw} accurately represents the driving potential for convective heat transfer at the outer surface of the airfoil. This assumption is not always valid, however, as mentioned in Section 1.3.3. Using CFD analysis performed as part of the larger project from which this thesis draws, Dyson et al. (2012) investigated the applicability of T_{aw} to represent the driving potential for heat transfer at the external surface for the same matched-Bi vane geometry experimentally studied for this thesis. CFD simulations were not only run for the conducting configuration, but also for a configuration with an adiabatic wall in order to compare gas temperatures immediately above the wall for both cases. They found that for the lowest flow rates where the jets were attached to the surface, T_{aw} was actually colder than the gas temperature immediately above the surface of a conducting wall, while T_{aw} was warmer than the gas temperature over the surface of the conducting wall at higher momentum flux ratios where the jets were detached. This should result in over-predicted ϕ_p values at lower momentum flux ratios, and under-predicted ϕ_p values at high momentum flux ratios, which was seen in Figures 3.29a through 3.29d.

3.3 Effect of Density Ratio

As discussed in Chapter 1, experimentally matching the jet-to-mainstream density ratio of an operating engine can be difficult, and many experimental studies including this one have used a lower density ratio while matching other parameters such as momentum flux ratio to those representative of an operating engine. For this reason, it is useful to know what effect increasing the density ratio would have had on the system, and for this reason a single data point was taken at a density ratio of 1.25 for comparison with the data measured at DR=1.12. It was intended to increase the density ratio to 1.4 for this portion of the experiment, but due to the way the DR was erroneously monitored during the experiment (using the coolant inlet temperature as the reference to calculate DR, instead of the cooling hole exit, which would have been more correct), it was lower than intended. Nevertheless, the increase of 12% in DR was enough to effect noticeable changes in the system behavior.

It is important to note that while the density ratio was increased, the target momentum flux ratio was maintained at the same nominal value as for the lower DR case so that the dynamic behavior of the film cooling jet penetrating into the mainstream would be preserved. Because it is not possible to independently vary the density ratio, momentum flux ratio, and blowing ratio all at the same time, the implication of matching the momentum flux ratio when increasing the density ratio is that the blowing ratio (and coolant mass flow rate) increased by about 7% from the low DR case to the high DR case.

While at the lower density ratio of $DR = 1.12$ the internal coolant thermocouples measured a strong span-wise temperature gradient as previously shown in Figures 3.11 and 3.12, this temperature gradient practically vanished when the density ratio was increased to $DR = 1.25$. This is shown in Figure 3.30 which compares the two span-wise instrumentation locations measuring internal gas temperatures for the high DR case at a momentum flux ratio of $I_{SS3} = 0.40$.

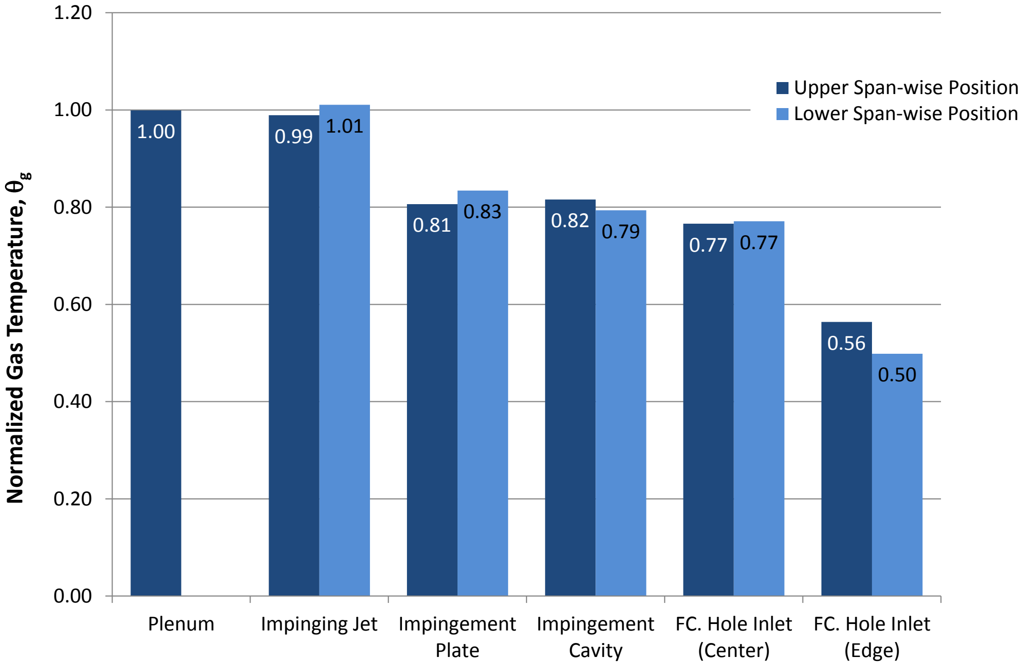

Figure 3.30: Comparison of internal coolant temperatures at two span-wise locations, film cooling active, $DR_{SS3} = 1.25$, $I_{SS3} = 0.40$

While Figure 3.30 shows that the temperatures at the upper and lower measurement locations for the $DR = 1.25$ case were nearly the same, they were also both close to the average of the "upper" and "lower" instrumentation locations previously shown in Figure 3.11 for the $DR = 1.12$ case. The disappearance of the span-wise temperature gradient which occurred when increasing DR suggests a major change in the internal coolant velocity field, although the increase in coolant density and mass flow rate only increased the internal flow Reynolds number by about 7%. During low

DR testing, however, the internal Reynolds number varied by over 200% across the range of momentum flux ratios tested, but the span-wise temperature gradient persisted as evidenced in Figure 3.12. This leaves the disappearance of the temperature gradient between the two span-wise locations to be attributed to complexities in the internal flow field which are not fully understood and are beyond the scope of this thesis.

Just as the increase in DR from 1.12 to 1.25 brought about an unexpectedly dramatic change in the internal coolant temperatures, it also had an impact on the inner wall surface temperatures measured by the five ribbon-type thermocouples. This was unexpected based on the change in DR alone, but follows naturally from the observation that the internal coolant temperatures changed as just discussed. The five ribbon type thermocouples are compared for both density ratios in Figure 3.31. The impact of the density ratio increase on the inner wall temperature was pronounced,

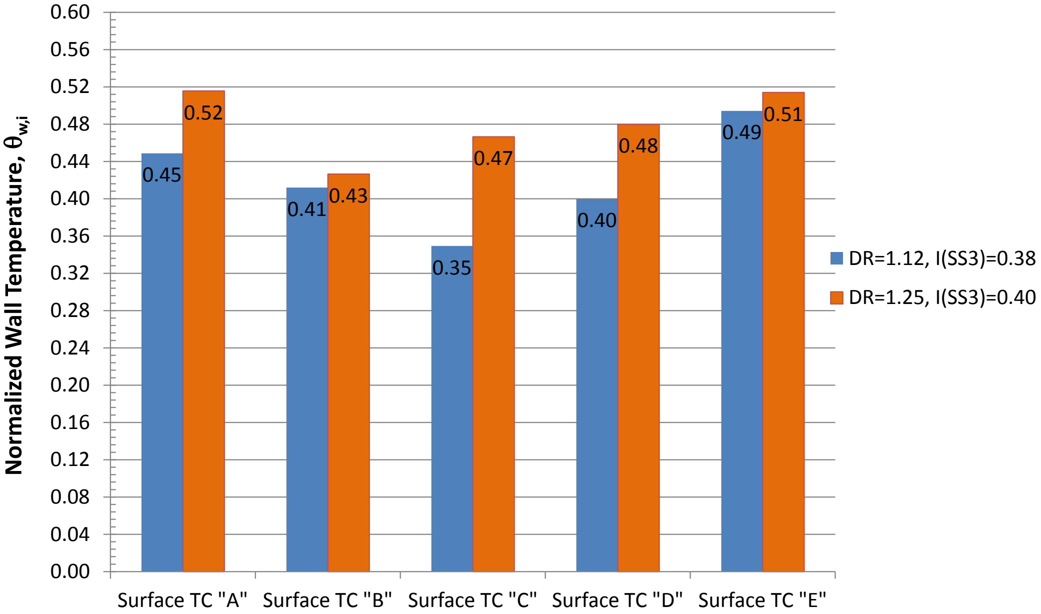

Figure 3.31: Effect of density ratio increase on internal wall surface temperatures, film cooling active, $I_{SS3} = 0.40$

increasing $\theta_{w,i}$ by 0.02 for thermocouples "B" and "E", and up to 0.12 in the case of thermocouple "C". A small increase in cooling performance on the inner surface was expected: the 7% increase in coolant mass flow rate since I_{SS3} was the parameter matched between the two density ratios should increase the strength of the impinging jets a small amount (raising h_i) while also reducing the amount of coolant pre-heat (due to the increased heat capacity rate associated with the increase in mass flow rate). The fact that the change in inner wall surface temperature was as much as 33 % may be viewed as an impact of the change in internal coolant velocity field and internal coolant temperatures of Figure 3.30. The fact that different thermocouples experienced very different changes in $\theta_{w,i}$ would back up this hypothesis, as thermocouples "E" and "B" experienced little improvement, even though "E" was positioned on the wall directly across from an impinging jet hole, while "B" was positioned on the wall mid-pitch between impinging jet holes. Thermocouples "C" and "D" both experienced larger increases in $\theta_{w,i}$, although "D" was at the same stream-wise location as "B" but positioned directly across from an impinging jet, and "C" was at the same span-wise location as "B" but positioned one-half of an impinging jet pitch farther downstream.

The improvement in overall effectiveness at $DR = 1.25$ agreed much more closely with expectations than did the internal temperatures. A comparison of the two different density ratios appears in Figure 3.32. It should be noted that the second repeat of the low-density $I_{SS3} = 0.38$ test condition is shown in this figure, for the simple fact that the second repeat point was measured immediately before cooling the system down to the higher density ratio. From the viewpoint of minimizing the effect of experimental uncertainty, if there was to have been any unknown bias error which crept into the measurements during the test, the second low-DR repeat point would have been more consistent with the high-DR test condition in terms of this unknown error. At the higher density ratio of 1.25, $\overline{\phi}$ improved by about 0.02 from that measured at the lower density ratio. This improvement is much closer to that experienced by inner surface thermocouples "B" and "E" than it is to the other three surface thermocouples, which may suggest that the temperatures measured at these two inner wall surface locations gave a more accurate representation of the relationship between internal cooling performance and overall effectiveness than that that given at thermocouple locations "A", "C" and "D", although why this would be the case is unclear.

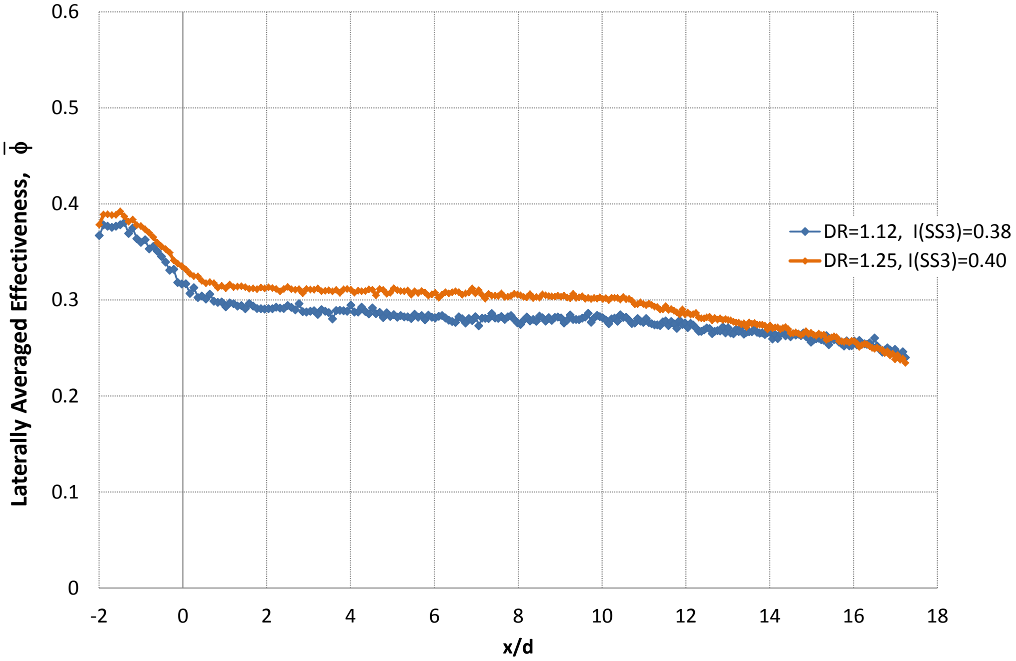

Figure 3.32: Effect of density ratio increase on overall effectiveness, film cooling active

Finally, a 2-D contour of ϕ for the high-DR test condition appears in Figure 3.33, which may be compared with Figure 3.19 to asses the impact of increasing the density ratio over the surface. It can be seen that the contours of overall effectiveness downstream of the cooling holes are higher in value for the high-DR case, as was seen with the lateral averages.

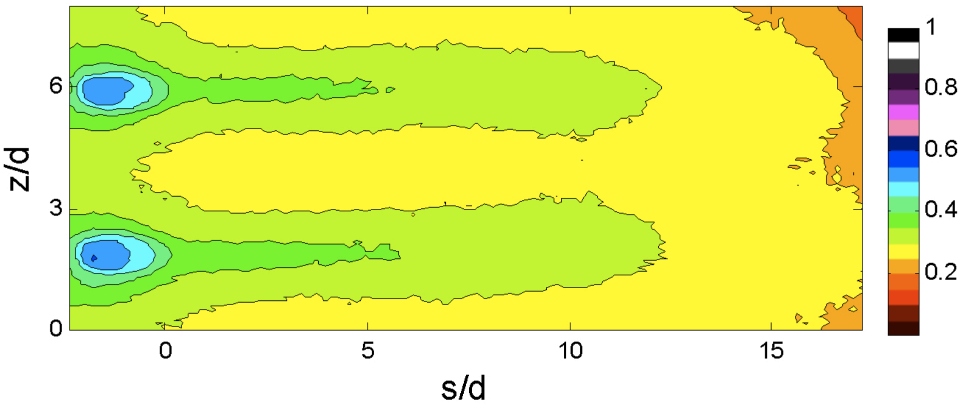

Figure 3.33: Overall effectiveness with film cooling active, $I_{SS3} = 0.40$, $DR_{SS3} = 1.25$

Chapter 4

Conclusions

A scaled-up gas turbine vane model was constructed in accordance with the matched-Bi technique and was used to collect internal gas and surface temperature data including the conjugate effects of both internal and external heat transfer. The vane model included an internal impingement cooling scheme, and a single row of film cooling holes located on the suction side. This study represents the first time in the open literature that a matched-Bi airfoil with internal impingement and external film cooling has been used to measure internal surface temperatures and gas temperatures along the coolant flow path as a function of coolant flow rate, and is also only the second study to quantify overall effectiveness downstream of a single row of holes on the suction side of a matched-Bi airfoil. This makes the present dataset extremely valuable for use in the validation of advanced computational models used in the thermal design of gas turbine engines. Although Dees et al. (2011b) measured overall effectiveness downstream of a single row of film cooling holes on the suction side of a matched-Bi airfoil with the same external geometry, the internal cooling in that study was provided by a much different internal U-bend channel and was located on a higher-curvature surface of the vane, resulting in very different trends from the current study.

A typical gas turbine vane with film cooling may have many rows of film cooling holes distributed over its surface. In order to provide a simple geometry and cooling configuration for the purposes of initial CFD predictions, a single row of film cooling holes was used, with the goal of eventually adding many more rows of holes as part of a subsequent study. This simplification made the internal impingement cooling somewhat unrealistic, however, as all of the coolant flowing through the impingement plate was ultimately ejected as film coolant and the impingement plate was designed for the scenario of a fully-cooled (multi-row) vane, so only having one row of film cooling holes reduced the amount of coolant flowing through the model and also resulted in a different distribution of coolant among the impingement holes than would exist with a fully-cooled vane. Nevertheless, the uniqueness of the present study still gives importance to the data collected.

A simple 1-D heat transfer analysis was performed (resulting in the identification of a new film-cooling parameter , χ) which was used to aid in the interpretation of the test results and to relate overall effectiveness to adiabatic film effectiveness. The effect of density ratio on system temperatures was also investigated.

This chapter is broken into two sections: first, a summary of the test results is presented along with significant conclusions drawn, followed by a section discussing recommendations of future work to be done.

4.1 Summary of Results

In order to measure gas temperature along the internal coolant flow path, the vane model was instrumented with an arrangement of internal thermocouples. These thermocouples were monitored as the coolant flow rate was varied at a nominal density ratio of $DR = 1.14$. The extent that the coolant warmed up as it flowed through the model from the inlet, through impingement holes and cavity, proceeding to the film cooling holes was quantified. At the middle of the inlet to the film cooling holes the normalized temperature (relative to the average impinging jet temperature and mainstream temperature) for $I_{SS3} = 0.38$ were about $\theta_g = 0.81$ for the top hole and $\theta_g = 0.71$ for the lower hole, indicating that the coolant had lost between 19% and 29% of its cooling potential before even entering the film cooling holes. As the coolant flow rate was increased to $I_{SS3} = 4.80$ the coolant warmed up less with about $\theta_g = 0.92$ and $\theta_g = 0.84$ for the top and bottom holes, respectively, due to the higher capacity flow rate ($\dot{m}C_p$). An increase in temperature was expected, since heat is continually transferred to the coolant as it flows through the model. However, because the vane model only had one row of holes and a lower coolant mass flow rate than it would for a multi-row, fully-cooled configuration, the amount of warming seen here is most likely unrealistically high.

As noted above, each of the temperatures measured along the flow path at the upper span-wise instrumentation location were colder than the same temperatures at the lower span-wise instrumentation location. This disagreed with expectation because the coolant inlet to the model was nearer to the lower location, and it was expected that the coolant would flow from the base upward, warming in temperature along the way. However, these measurements revealed that the internal coolant velocity field was more complex than initially assumed, potentially due to the geometry of the inlet to the coolant plenum, where the coolant may have been jetting upwards through the front of the model and then turning and flowing downwards before passing through the impingement plate and eventually the film cooling holes.

It was desired to independently examine the the effects of internal impingement and external film cooling on system temperatures and overall effectiveness. In order to do this, temperature measurements were made under two different cooling conditions at the same coolant flow rates: first, measurements were made with two of the film cooling holes taped over, so that temperatures measured in the region between these holes may be viewed as a case of simulated “internal cooling only”. Then, the holes were unblocked for measurements with the full effect of film cooling. It was seen that the internal gas temperatures remained essentially the same for the cases, although the measured internal and externals surface temperatures were markedly different. Because all of the coolant flowing through the impingement plate eventually had to leave through the film cooling holes, it was reasoned that taping over the two middle film cooling holes would have impacted the flow path and thereby could have had an effect on the coolant temperatures, although this would not be ideal for comparing the with- and without-film-cooling cases. The fact that the surface temperatures experienced a noticeable change while the internal gas temperatures did not was reasonable, since the strength of the impinging jets near the blocked holes could have been affected while the gas temperature measurements remained unaffected, since these gas temperatures were measured at span-wise locations nearer to holes which remained un-blocked.

For test conditions where the middle two film cooling holes were blocked, internal and external surface temperatures both dropped monotonically as the film coolant mass flow rate was increased. This was unsurprising, since in the absence of film cooling, the impinging jets over the internal surface were the dominant cooling mechanism and the velocity of these impinging jets should only increase with coolant flow rate. Values of $\theta_{w,i}$ at different internal positions ranged from 0.30 to 0.45 for $I_{SS3,eq.} = 0.38$ and increased to between $\theta_{w,i} = 0.45$ and 0.56 for $I_{SS3,eq.} = 4.80$. Measured values of overall effectiveness for this simulated “internal cooling only” condition ranged from about $\overline{\phi}_0 = 0.21$ for $I_{SS3,eq.} = 0.38$ to $\overline{\phi}_0 = 0.28$ for $I_{SS3,eq.} = 4.80$.

The relative increase in both measured $\overline{\phi}_0$ and $\theta_{w,i}$ with increased coolant flow rate was smaller at the lower flow rates than the higher ones, and values of h_i calculated from the 1-D resistance analogy using $\overline{\phi}_0$ and h_0 disagreed with published correlations for impingement jet heat transfer. One possibility for this is that 3-D heat transfer effects may have more importance at higher values of $I_{SS3,eq}$, which would reduce the validity of the 1-D analysis. Also, it is likely that the impingement jet velocity in the measurement region did not increase proportionally to the total coolant flow rate because the impinging jets were spaced evenly over the entire inner wall surface, but all of the coolant had to leave from one row of holes of film cooling jet holes on the suction side of the vane. This could result in more film coolant being concentrated through impinging jets near the row of film cooling holes at lower I_{SS3} values, and a more uniform coolant distribution over all of the film cooling jets when I_{SS3} and the coolant plenum pressure are increased.

Subsequent testing was performed by lab-mate Tom Dyson using the same physical vane model modified with additional film cooling holes to give a "full coverage" film cooling configuration. Overall effectiveness values with some holes blocked to provide a case of simulated "internal cooling only" were much higher than those of the current study, ranging from $\overline{\phi_0} = 0.40$ to 0.49 at significantly lower momentum flux ratios of $I_{SS3} = 0.40$ to 0.75 (Dyson et al., 2013). This increase is due to the greater internal coolant flow rate for the full coverage case, which resulted in stronger and presumably a more uniform distribution of coolant among the rows of impinging jets.

With both internal impingement cooling and external film cooling present on the matched-Bi vane model, a peak in normalized internal wall surface temperature, $\theta_{w,i}$, occurred at a coolant jet momentum flux ratio of $I_{SS3} = 2.46$, and dropped as the coolant flow rate was increased to $I_{SS3} = 2.98$. Comparing the values with all of the film cooling holes active to the test cases of simulated “internal cooling only”, it was seen that the internal impingement was the dominant mechanism responsible for cooling the inner wall surface as the addition of film cooling only increased $\theta_{w,i}$ by between 10% and 20% at the lowest flow rates, around 30% at $I_{SS3} = 2.46$, and provided almost no benefit at higher flow rates. The increase in $\theta_{w,i}$ with the addition of film cooling at momentum flux ratios from $I_{SS3} = 1.09$ to 2.46 may be primarily attributed to additional convective cooling inside the film cooling holes and a re-configuring of the internal coolant velocity field when all of the film cooling holes were activated, since it was shown that the adiabatic film effectiveness had diminished at these coolant momentum flux ratios. It was also speculated that a contributing factor to the subsequent drop in $\theta_{w,i}$ above these flow rates may be an increase in the external heat transfer coefficient above $I_{SS3} = 2.46$, which would have the effect of increasing the external wall temperature (decreasing $\theta_{w,i}$ and ϕ), although a re-configuration of the impinging jets was a more likely cause since the drop in ϕ was greater than that seen in $\theta_{w,i}$.

Overall effectiveness, ϕ, may be viewed as the most relevant measure of film cooling performance since it represents the outer wall surface temperature of a real engine component. Laterally averaged values of ϕ downstream of the film cooling holes were shown to increase with coolant momentum flux ratio of up to $I_{SS3} = 1.59$ and 2.46 before experiencing a slight drop at $I_{SS3} = 2.98$. This value of I is dependent on several factors. First, the film effectiveness, η, was shown in a separate experiment to peak at the lowest momentum flux ratio of $I_{SS3} = 0.17$ and decreased rapidly afterwards. At the same time, h_i increases with I_{SS3} as likely does the external heat transfer coefficient with film cooling, h_f. While these three concurrent effects impact ϕ, ultimately there was no single good explanation for the drop in ϕ at $I_{SS3} = 2.98$. This unexpected result was repeatable in two separate experiments, however, and the fact that $\theta_{w,i}$ experienced a greater drop than ϕ suggests that a drop in internal cooling was primarily responsible. The trend in ϕ with I_{SS3} seen here stood in contrast to that seen by Dees et al. (2011b), who held the internal cooling condition essentially constant and saw a decrease in ϕ as η dropped with increasing I. This stands to emphasize the internal cooling configuration as one of the major difference between the present study and that of Dees et al..

Because component reliability depends on the highest temperature present in the metal component, the presence of hot spots between film cooling holes is important and is masked in the laterally averaged values. Consequently, it is important to review the spatial distributions of ϕ. Examination of the 2-D contour plots of ϕ showed that while laterally averaged values, $\overline{\phi}$ had very similar values at both highest and lowest flow rates tested, stronger lateral temperature gradients across the surface existed for the lowest coolant flow rates tested, resulting in warmer surface temperatures mid-pitch. At the higher flow rates where the jets were presumed to be fully detached from the surface, the surface temperature was much more uniform, owing to internal impingement cooling as the dominant cooling mechanism.

Based on a simplified 1-dimensional heat transfer analysis through a plane wall and the assumption that the adiabatic wall temperature, T_{aw}, is the appropriate potential for heat transfer at the external surface, measurements of $\overline{\eta}$ and $\overline{\phi}_0$ were used to predict $\overline{\phi}$ with film cooling. This approach over-predicted $\overline{\phi}$ at the lowest momentum flux ratios, while under-predicting it at the highest momentum flux ratios. The most likely cause for the disagreement between predicted and measured $\overline{\phi}$ values is that the simplifying assumption of 1-dimensional heat transfer was not valid. Furthermore, it is questionable whether T_{aw} accurately represents the driving temperature for heat transfer to the external vane surface (as recently shown by Dyson et al. (2012) during CFD analysis of the same matched-Bi vane geometry studied here).

Finally, the effect of the coolant density ratio, DR, on coolant and internal surface temperatures as well as overall effectiveness was investigated. As the coolant density ratio was increased while keeping I_{SS3} near the target of 0.38, several changes were noticed. First, the span-wise temperature gradient seen in the internal gas measurements represented by θ_g at $DR = 1.12$ nearly vanished at $DR = 1.25$, suggesting a major change in the internal coolant flow field that is not currently understood. Also, the normalized inner wall temperature $\theta_{w,i}$ increased significantly, which would follow from the change in the internal coolant flow field. Measured values of $\overline{\phi}$ at $DR = 1.25$ were much more in line with expectations, showing only a moderate increase from the values at the lower $DR = 1.12$.

4.2 Recommendations for Future Work

There are several aspects of the current study which may easily expanded upon. First and foremost, the large amount of temperature data collected here provide ample opportunities for comparisons to CFD predictions of overall effectiveness and internal temperatures. This was actually one of the primary goals of this project, as much work remains to be done in validating different CFD codes and turbulence modelling schemes which may be used in the design of gas turbine cooling schemes. Along these lines, Dyson et al. (2012) performed CFD simulations of the geometry and test conditions used for the current study, employing the $k - \omega SST$ model and a steady $RANS$ approach. They compared ϕ and η distributions and saw that while ϕ values remained close between the CFD and experiments, the $k - \omega SST$ under-predicted jet diffusions. Other opportunities to use the dataset presented here include examination of other modelling approaches and comparison of internal gas and inner wall surface temperatures to predictions.

During the data reduction and analysis, a few unexpected results were seen. The first of these is that the vane model was colder at the top than at the bottom, even though the coolant inlet was at the bottom of the model and the coolant was experted to warm as it flowed upwards. It was speculated that a complex internal flow field could be responsible for this; additional CFD simulations may shed light into the nature of the internal coolant flow field, although this could also be investigated experimentally by using a larger number of internal thermocouples to gather a more detailed map of the internal temperatures. Additionally, the internal cooling geometry could be modified to help re-distribute the flow inside the plenum by installing screens or baffles, or by changing the shape of the coolant inlet at the base of the vane model.

One significant weakness of the dataset is that because the vane model only had one row of film cooling holes on the suction side being fed from the front plenum, the total amount of coolant flowing through the model and its distribution over the array of internal impinging jets does not accurately represent a realistic internal cooling configuration for actual gas turbine vanes, which typically have many rows of film cooling holes distributed over the airfoil surface. With a single row of holes, more coolant was expected to flow through the impinging jets closest to the row of film cooling holes than through the impinging jet holes farther away. Separate experiments or CFD analysis could be performed to further examine the coolant distribution through the internal impingement plate in order to better understand these results. However, the cooling configuration with the single row of holes tested for this thesis was actually a stepping stone on the path to performing experiments with a much more complex “fully cooled” vane model containing 13 rows of holes, in which case only 15% of the coolant would be flowing through the suction side row tested here, resulting in a more even distribution of coolant through the impinging jet holes.

Finally, there was a significant drop in both $\theta_{w,i}$ and $\overline{\phi}$ when film cooling was present as the jet momentum flux ratio was increased to $I_{SS3} = 2.98$. It was speculated that this may be due to a “reconfiguration” of the impinging jets cooling the inner wall surface, and/or an increase in external heat transfer coefficient. Again, this provides another opportunity to further investigate augmentation of the external heat transfer coefficient in the presence of very strong jets, which could be done using a CFD analysis or experimentation.

Bibliography

Jason E Albert. Adiabatic and overall effectiveness measurements of a forward-diffused film cooling configuration for a turbine blade leading edge. Master's thesis, The University of Texas, 2003.

Jason E Albert. *Experimental Simulation and Mitigation of Contaminant Deposition on Film Cooled Gas Turbine Airfoils*. PhD thesis, The University of Texas, 2011.

Jason E. Albert, David G. Bogard, and Frank Cunha. Adiabatic and overall effectiveness for a film cooled blade. *ASME Conference Proceedings*, 2004(53998):251–259, 2004.

S. Baldauf, M. Scheurlen, A. Schulz, and S. Wittig. Correlation of film-cooling effectiveness from thermographic measurements at enginelike conditions. *Journal of Turbomachinery*, 124:686–698, 2002.

David G. Bogard and Karen A. Thole. Gas turbine film cooling. *Journal of Propulsion and Power*, 22(2):249–270, 2006.

M.P. Boyce. *Gas turbine engineering handbook*. Referex Engineering. Gulf Professional Pub., 2002.

Y.A. Çengel and M.A. Boles. *Thermodynamics: an engineering approach*. McGraw-Hill series in mechanical engineering. McGraw-Hill Higher Education, 2006.

R. E. Chupp, H. E. Helms, and P. W. McFadden. Evaluation of internal heat-transfer coefficients for impingement-cooled turbine airfoils. *Journal of Aircraft*, 6(3):203–208, 1969.

Pedro de la Calzada and Jose Javier Alvarez. Experimental investigation on the heat transfer of a leading edge impingement cooling system for low pressure turbine vanes. *Journal of Heat Transfer*, 132(12):122202, 2010.

Jason E. Dees, David G. Bogard, Gustavo A. Ledezma, Gregory M. Laskowski, and Anil K. Tolpadi. Experimental measurements and computational predictions for an internally cooled simulated turbine vane. *ASME Conference Proceedings*, 2009 (43826):2135–2144, 2009.

Jason E. Dees, David G. Bogard, Gustavo A. Ledezma, Gregory M. Laskowski, and Anil K. Tolpadi. Momentum and thermal boundary layer development on an internally cooled turbine vane. *ASME Conference Proceedings*, 2010(43994):457–469, 2010.

Jason E. Dees, David G. Bogard, Gustavo A. Ledezma, and Gregory M. Laskowski. The effects of conjugate heat transfer on the thermal field above a film cooled wall. *Proceedings of the ASME Turbo Expo 2011*, (46617), 2011a.

Jason E. Dees, David G. Bogard, Gustavo A. Ledezma, and Gregory M. Laskowski. Overall and adiabatic effectiveness values on a scaled up, simulated gas turbine vane: Part i - experimental measurements. *Proceedings of the ASME Turbo Expo 2011*, (46612), 2011b.

Thomas E. Dyson, David G. Bogard, and Sean D. Bradshaw. Evaluation of CFD simulations of film cooling performance on a turbine vane including conjugate heat transfer effects. *Proceedings of the ASME Turbo Expo 2012*, (69107), 2012.

Thomas E. Dyson, J. W. McClintic, David G. Bogard, and Sean D. Bradshaw. Adiabatic and overall effectiveness for a fully cooled turbine vane. *Proceedings of the ASME Turbo Expo 2013*, (94928), 2013.

Marcia I. Ethridge, J. Michael Cutbirth, and David G. Bogard. Effects of showerhead cooling on turbine vane suction side film cooling effectiveness. In *Proceedings of ASME International Mechanical Engineering Congress and Exposition*, 2000.

Richard J. Goldstein. Film cooling. volume 7 of *Advances in Heat Transfer*, pages 321 – 379. Elsevier, 1971.

Richard J. Goldstein. *Fluid mechanics measurements.* Taylor & Francis, 1996.

J.C. Han, S. Dutta, and S. Ekkad. *Gas turbine heat transfer and cooling technology.* Taylor & Francis, 2000.

Katiherine L. Harrison and David G. Bogard. Use of the adiabatic wall temperature in film cooling to predict wall heat flux and temperature. In *Proceedings of ASME Turbo Expo 2008: Power for Land, Sea and Air*, 2008.

L. D. Hylton, M. S. Mihelc, E. R. Turner, D. A. Nealy, and R. E. York. Analytical and experimental evaluation of the heat transfer distribution over the surfaces of turbine vanes. Technical report, May 1983.

L. D. Hylton, V. Nirmalan, B. K. Sultanian, and R. M. Kaufman. The effects of leading edge and downstream film cooling on turbine vane heat transfer. Technical report, November 1988.

F.P. Incropera and D.P. DeWitt. *Fundamentals of heat and mass transfer.* J. Wiley, 2002.

Ross G. Johnson. Experimental study of the effect of oscillating stagnation line on overall cooling performance on a leading edge with one row of cooling holes. Master's thesis, The University of Texas, 2008.

Robert J. Moffat. Describing the uncertainties in experimental results. *Experimental Thermal and Fluid Science*, 1(1):3 – 17, 1988.

Neil Petchers. *Combined Heating, Cooling and Power Handbook : Technologies and Applications*. Marcel Dekker, Inc., 2002.

Yoran Pinchon. Turbulence field measurements for the large wind tunnel. The University of Texas at Austin TTCRL Internal Report, 2009.

P. C. Sweeney and J. F. Rhodes. An infrared technique for evaluating turbine airfoil cooling designs. *Journal of Turbomachinery*, 122(1):170–177, 2000.

Elon J. Terrell, Brian D. Mouzon, and David G. Bogard. Convective heat transfer through film cooling holes of a gas turbine blade leading edge. *ASME Conference Proceedings*, 2005(47268):833–844, 2005.

Scot K. Waye and David G. Bogard. High resolution film cooling effectiveness comparison of axial and compound angle holes on the suction side of a turbine vane. *ASME Conference Proceedings*, 2006(4238X):195–203, 2006.

Randall P. Williams, Thomas E. Dyson, David G. Bogard, and Sean D. Bradshaw. Sensitivity of the overall effectiveness to film cooling and internal cooling on a turbine vane suction side. *Proceedings of the ASME Turbo Expo 2012*, (69110), 2012.

Vita

Randall Paul Williams was born in Beeville, Texas in 1984. The oldest of two siblings, he expressed an interest in engineering at an early age, and almost caught the living room carpet on fire after connecting a vacuum cleaner motor to a car battery using speaker wire (receiving his first lesson in Joule heating in the process). He attended Texas A&M University in College Station and studied Mechanical Engineering, receiving his B.S. in 2006. His engineering interests include design of thermal/fluid systems and active cooling of electronics and gas turbine engine components, the development and optimization of synthetic jet actuators, and moving coil actuator design. Randy has too many hobbies, and in his free time he loves playing guitar, cooking, travelling, live music, hunting hogs and deer in South Texas, and the beach. His favorite movie is Idiocracy, and he prefers beers that are dark, yet hoppy.

Permanent address: 5186 Star Trek Dr.
Beeville, TX 78102

This thesis was typeset with LaTeX[†] by the author.

[†] LaTeX is a document preparation system developed by Leslie Lamport as a special version of Donald Knuth's TeX Program.